LYMAN-α SPECTROSCOPY OF MAGNETICALLY TRAPPED ATOMIC HYDROGEN

ACADEMISCH PROEFSCHRIFT

ter verkrijging van de graad van doctor
aan de Universiteit van Amsterdam,
op gezag van de Rector Magnificus
prof. dr. P. W. M. de Meijer
in het openbaar te verdedigen in de Aula der Universiteit
(Oude Lutherse Kerk, ingang Singel 411, hoek Spui),
op vrijdag 12 november 1993 te 10.00 uur

door

Otger Jan Luiten

geboren te Eindhoven

Druk: Boek- en Offsetdrukkerij Letru, Helmond, 04920-37797

Promotor:	prof. dr. J. T. M. Walraven
Co-promotor:	dr. T. W. Hijmans

Faculteit der Natuur- en Sterrenkunde

The work described in this thesis was carried out at the

Van der Waals - Zeeman Laboratorium
Universiteit van Amsterdam
Valckenierstraat 65-67
1018 XE Amsterdam

and was financially supported by the
"Stichting voor Fundamenteel Onderzoek der Materie (FOM)",
and the
"Nederlandse Organisatie voor Wetenschappelijk Onderzoek (NWO-PIONIER)".

Contents

Chapter 1

Introduction

1.1 Cold trapped atoms

Through the interaction with electromagnetic fields atoms can be localized and levitated in space, free from confining material surfaces. In vacuo the atoms are thus ideally isolated from their environment, only influenced by the confining electromagnetic field. The realization of such conditions offers opportunities in many areas of physics. Obviously, the combination of the confinement of a particle, allowing for long observation times, and the elimination of external influences is ideal for high-precision studies of fundamental single particle properties, which may have important consequences, for example, for the development of more accurate frequency standards [1]. Making use of the potentially very low kinetic energies of the trapped particles, collisional phenomena can be studied in a new regime of ultra-low collisional energies, both between atoms [2] and between atoms and surfaces [3]. Traps may also be put to use as sources of very slowly moving atoms for matter-wave experiments, such as atomic interferometry [4].

Maybe the most intriguing, however, is the possibility to prepare collections of many weakly interacting particles under such conditions that the quantum mechanical uncertainty in position, expressed by the thermal wavelength $\lambda_{th} = h/\sqrt{2\pi m k_B T}$, becomes comparable to the interparticle spacing, $\lambda_{th} \sim n^{-1/3}$. Here T is the temperature of the trapped gas, n the gas density, and m the particle mass. For these conditions of quantum degeneracy new, exotic states of matter have been predicted. For instance, in the weakly interacting bosonic system of atomic hydrogen for $T\,n^{-2/3} = 1.6 \times 10^{-14}\,\mathrm{K\,cm^2}$ a phase transition to a gaseous state displaying macroscopic quantum behavior is expected to occur, the so-called Bose-Einstein condensation (BEC). Quantum degeneracy in a system of weakly interacting particles would provide a model system for macroscopic quantum behavior, with possibly important consequences for the understanding of superconductivity and superfluidity.

Trapping of charged particles is possible since the invention of the Paul trap in 1958 [5]. Trapping of neutral particles is much harder because the trapping forces must rely on interactions with higher order moments, such as, for instance, static magnetic dipole moments, which are much weaker than electrostatic interactions. The resulting trapping potentials are therefore relatively shallow and the particles must be "pre-cooled" to very small kinetic energies before they can be trapped. For example, the magnetic moment of atoms is typically $\sim \mu_B$, the Bohr magneton. Since the maximum achievable well depths of static magnetic traps are of the order $\Delta B \approx 1\,\mathrm{T}$, the kinetic energy of the atoms has to be reduced to less than $\mu_B \Delta B / k_B \sim 1\,\mathrm{K}$, in temperature units. In 1977 Kügler *et al.* succeeded in trapping very slow neutrons ($v < 20\,\mathrm{m/s}$) in a magnetic storage ring [6].

In the last decade enormous progress has been made in the field of trapping and cooling, which is for a large part due to the development of laser cooling techniques. In 1985 the first neutral atoms were trapped by decelerating a beam of sodium atoms using near-resonant laser light and subsequently switching on a magnetostatic trap [7]. Since then the field of trapped neutral atoms has grown at a very rapid pace and many trapping schemes have been developed (mainly for the alkalis Na, Rb, and Cs) employing optical fields, static magnetic fields, microwave fields, and combinations of these [8, 9]. These schemes have in common that a continuous wave (cw) laser is required. As this was (and still is) not available at the Lyman-α wavelength ($\lambda_\alpha = 121.6\,\mathrm{nm}$) of the $1S \rightarrow 2P$ transition in atomic hydrogen, the simplest atom was initially excluded from this line of research. However, in 1987 Hess *et al.* [10] and shortly thereafter Van Roijen *et al.* [11] succeeded in magnetically trapping hydrogen atoms, using cryogenic instead of optical techniques.

1.2 Spin-polarized atomic hydrogen

Atomic hydrogen is the only gaseous atomic system in which quantum degeneracy was already pursued before the advent of electromagnetic trapping techniques. This was made possible by the fact that H gas can be stabilized at sub-Kelvin temperatures by applying a strong magnetic field and covering the walls of the containing vessel with a layer of liquid helium, as was first demonstrated by Silvera and Walraven [12]. The strong B-field aligns the electron spins, thus suppressing recombination to the molecular state in the gas, while the extremely low energy of physisorption of H on a liquid-helium surface ($\sim 1\,\mathrm{K}$) prevents massive surface adsorption and thus minimizes surface-catalyzed recombination. Owing to the weakness of the triplet interatomic potential and the small atomic mass, spin-polarized

H is expected to remain gaseous down to $T = 0$, which makes it the ideal candidate for the observation of quantum degeneracy in a weakly interacting system.

Initially, experiments were aimed at increasing the density of a gas of "high-field seeking" spin-down polarized H (H↓) in thermal equilibrium with the cell walls [13]. It turned out that in this approach serious limitations arise on both the attainable density and the temperature of the gas due to three-body recombination on the surface, which make reaching BEC very hard, if not impossible. For this reason the attention turned to wall-free confinement of "low-field seeking" spin-up polarized hydrogen atoms (H↑) in a static B-field minimum [14]. Since a B-field maximum in free space is not allowed by Maxwell's equations, it is not possible to trap H↓ magnetostatically. In switching from H↓ to H↑, however, orders of magnitude in stability are sacrificed because an extra two-body decay channel is introduced in the form of electron spin relaxation to the non-trapped H↓ state, which is energetically favorable [15].

Among the trapable atomic species atomic hydrogen is unique in the sense that no optical techniques are required to load atoms into a magnetostatic trap. Instead H↑ gas can be pre-cooled to sub-Kelvin temperatures and manipulated by liquid-helium covered surfaces. In this way gas densities can be built up around the trapping region which are sufficiently high to scatter atoms into trapped states through elastic interatomic collisions. In fact, this filling mechanism is so efficient that the achievable gas densities ($\leq 3 \times 10^{14}\,\mathrm{cm}^{-3}$) are higher than in any other trapped system and are only limited by two-body collisional relaxation to non-trapped H↓ [11]. As a result the trapped gas quickly reaches a state of internal equilibrium through elastic interatomic collisions. This is not only important for a proper description of the statistical properties of the gas, but it also enables a cooling method that does not require optical techniques: evaporative cooling [10]. As the trapped atoms are continually redistributing their energies through elastic collisions, sometimes H↑ atoms are produced with kinetic energies larger than the well depth which subsequently escape (evaporate) from the trap. After thermalization this results in a lower temperature of the remaining gas. By slowly reducing the well depth the temperature can be reduced even further. Using this technique, temperatures as low as $\sim 100\,\mu\mathrm{K}$ at densities $\sim 8 \times 10^{13}\,\mathrm{cm}^{-3}$ have been attained with trapped H, which is within an order of magnitude of the above-mentioned BEC criterion [3].

Although laser cooling techniques have been very successful in reducing the kinetic energy of trapped atoms - average energies $\sim 1\,\mu\mathrm{K}$ are achieved more or less routinely in trapped Cs - it is now generally being recognized that evaporative cooling techniques are the most promising for reaching the quantum degenerate regime, also for other atoms than H [16]. This may be illustrated with the following simple argument. The lowest temperature that can be reached with current laser cooling techniques is the so-called single photon recoil limit $T_R = \hbar^2 k^2/2mk_B$, where k is the wavenumber of the photon. For atomic hydrogen $T_R \approx 650\,\mu$K and for cesium $T_R \approx 0.13\,\mu$K. This corresponds to the situation in which the average atomic momentum is $\sim \hbar k$, the recoil due to the spontaneous emission of a photon. In other words, at the recoil limit the thermal wavelength λ_{th} of the atoms is approximately equal to the wavelength λ of the light. Therefore, in order to reach the quantum degenerate regime using laser cooling, the density should be so high that the average interatomic distance $n^{-1/3} < \lambda$. It is clear that under these conditions the usual optical cooling principles, which are based on single particle excitation, are no longer applicable.

1.3 This thesis

Until recently all information on the samples of trapped H$\uparrow$ was obtained indirectly by monitoring the flux of atoms escaping from the trap [3, 11]. To this purpose the traditional bolometric technique was employed to detect the heat released in the recombination to the molecular state. In Amsterdam Van Roijen *et al.* [11, 17] studied the magnetic relaxation of trapped H$\uparrow$ in thermal equilibrium with the surrounding walls in this way. However, as the quantum degeneracy regime comes within reach, the traditional detection techniques start lacking sensitivity and the need arises for a non-destructive, *in situ* detection technique, capable of independently determining the temperature and the density of the trapped gas. Resonant optical techniques seem the obvious answer. These techniques have not been applied before mainly because of a hesitancy to combine the cryogenic environment (dilution refrigerator) necessary for spin-polarized H research with the requirements for the generation and detection of narrowband Lyman-α radiation (harmonic generation and vacuum optics).

In this thesis the implementation of resonant optical techniques at the Lyman-α wavelength to the system of trapped H$\uparrow$ is described. The results of the first optical experiments with trapped H$\uparrow$ are presented, showing the value and the reliability of this new diagnostic method, and a detailed description is given of the theoretical and the experimental aspects of Lyman-α spectroscopy. As a first application the dynamics are studied of a sample which is thermally isolated from the surrounding walls by means of evaporative cooling. The important evaporative cooling process is investigated both theoretically and experimentally.

First and foremost, an accurate description of the magnetic field $\vec{B}(\vec{r})$ in our trap is required, both for the spectroscopy of the gas and for the description of its dynamical properties. In Chapter 2 an approximate method for calculating the field in our magnetic trap is developed, based on an expansion method, which yields accurate analytical expressions.

In Chapter 3 the properties of samples of trapped H$\uparrow$ are reviewed. The loading of the trap, the thermalization process, and several particle loss and heating mechanisms are discussed. An approximate description of the field in our so-called Ioffe trap is introduced, which allows us to obtain convenient analytical expressions for the density of trapped states, which in turn enables straightforward calculation of important quantities like the effective volume, the specific heat, and the average interatomic collision rates.

Chapters 4 and 5 deal with the experimental techniques. Chapter 4 describes the cryogenic part of the setup, in particular the construction details of the experimental cell at the heart of the dilution refrigerator. New features are the optical access from room temperature and the installation of cryogenic Lyman-α detectors inside the cell, which enable measurement of both the transmission of the sample and the resonant fluorescence. Chapter 5 describes the optical part of the setup. Narrowband Lyman-α radiation (121.6 nm, bandwidth $\sim 100\,\mathrm{MHz}$) is generated in krypton gas as the third harmonic of pulsed UV light at 364.8 nm. The efficiency of our Lyman-α generation scheme is investigated and various special techniques are discussed concerning frequency tuning and stability and the use of vacuum optics. Furthermore, the design and the detection sensitivity of our home-made cryogenic Lyman-α detectors are discussed.

Chapter 6 is devoted to Lyman-α spectroscopy of samples of trapped H$\uparrow$. The first half of this chapter gives a detailed theoretical treatment of the extinction of a Lyman-α beam passing through an H$\uparrow$ sample. A proper description, necessary for the understanding of the experimental spectra and reliable diagnostics of the gas, turns out to be quite involved. It entails including effects due to Zeeman shifts, Doppler shifts, optical thickness, the polarization of the light, and optical activity of the sample. In the second half of this chapter several examples of experimental spectra are presented. The general features of the spectra are qualitatively explained and it is shown how the temperature and the density of the gas can be determined through careful fitting with approximately 25% accuracy. The accuracy is mainly limited by imprecise knowledge of the beam shape. Some spectra display unexpected features, which are explained in terms of subtle polarization and dispersion effects. The emphasis in this work is on transmission spectroscopy, but some fluorescence spectra are analyzed as well. Furthermore, optical evidence is shown of the fact that cold deuterium gas can be produced and subsequently transported to the trapping region. However, we were not able to trap D$\uparrow$.

In Chapter 7 the dynamics of the evaporative cooling process is investigated. A convenient model is presented, free of adjustable parameters, which allowed us to derive analytical expressions for the particle and energy loss rate during evaporative cooling in our Ioffe trap. It is shown that under conditions favorable for obtaining reasonable cooling rates, the energy distribution of the trapped atoms deviates essentially from the Boltzmann form. Using Lyman-α transmission spectroscopy the evolution of the temperature and the density have been measured during the onset of the evaporation process. The experimental results are confronted with the theoretical description.

1.4 Future prospects

Aside from considerations of detection sensitivity, the application of Lyman-α resonant optical techniques to H$\uparrow$ was also strongly motivated by the possibility of optical cooling. Recently Setija *et al.* demonstrated optical cooling of trapped H$\uparrow$, using the apparatus described in this thesis [18]. Two methods were used: Doppler cooling, for which a minimum temperature of 8 mK was reported, and light-induced evaporation (LIE), a new cooling method by which 3 mK was reached. The latter is the optical analog of ordinary forced evaporative cooling [3] and is particularly promising. It has the advantage over the usual forced evaporation method that it is no longer necessary to ramp down the confining magnetic field, so one can work with a well-defined, static trapping potential. LIE requires high density samples (optically thick) and fast collisional thermalization. Therefore it is very well suited for trapped H$\uparrow$.

The LIE results obtained thus far are very encouraging. In order to reach lower temperatures higher cooling powers are required, which can be accomplished by simply increasing the Lyman-α intensity. Furthermore, once the sub-mK regime is entered, it will become necessary to upgrade the detection sensitivity as well, as the samples become very small. At present both the beam intensity and the detection sensitivity are mainly limited by the available control over the shape and the size of the beam at the site of the sample. The beam intensity may be further increased by improving the efficiency of the third harmonic generation of Lyman-α. With these improvements the μK regime should be within reach.

References

[1] D. J. Wineland, W. M. Itano, J. C. Bergquist, and R. G. Hulet, Phys. Rev. A **36**, 2220 (1987).

[2] J. Weiner, J. Opt. Soc. Am. B **6**, 2270 (1989).

[3] J. M. Doyle, J. C. Sandberg, I. A. Yu, C. L. Cesar, D. Kleppner, and T. J. Greytak, Phys. Rev. Lett. **67**, 603 (1991).

[4] D. E. Pritchard, in *Proceedings of the 13th International Conference on Atomic Physics*, H. Walther, T. W. Hänsch, and B. Neizert, eds. (American Institute of Physics, New York, 1993), p. 185.

[5] W. Paul, O. Osberghaus, and E. Fischer, Forschungsber. des Wirtsch. Verkehrsminist. Nordrhein-Westfalen **415** (1958).

[6] K.-J. Kügler, W. Paul, and U. Trinks, Phys. Lett. **72**B, 422 (1978).

[7] A. L. Migdall, J. V. Prodan, W. D. Phillips, T. H. Bergeman, and H. J. Metcalf, Phys. Rev. Lett. **54**, 2596 (1985).

[8] For an overview up to 1989 see the special issue on laser cooling and trapping of atoms, edited by S. Chu and C. Wieman, J. Opt. Soc. Am. B **6**, No. 11 (1989).

[9] C. C. Agosta, I. F. Silvera, H. T. C. Stoof, and B. J. Verhaar, Phys. Rev. Lett. **62**, 2361 (1989).

[10] H. F. Hess, G. P. Kochanski, J. M. Doyle, N. Masuhara, D. Kleppner, and T. J. Greytak, Phys. Rev. Lett. **59**, 672 (1987).

[11] R. van Roijen, J. J. Berkhout, S. Jaakkola, and J. T. M. Walraven, Phys. Rev. Lett. **61**, 931 (1988).

[12] I. F. Silvera and J. T. M. Walraven, Phys. Rev. Lett. **44**, 164 (1980).

[13] For an overview of the early H↓ experiments see I. F. Silvera and J. T. M. Walraven, in *Progress in Low Temperature Physics*, D. F. Brewer, ed. (North Holland, Amsterdam, 1986), Vol. 10, p. 139; for a more recent but less extensive overview see I. F. Silvera and M. W. Reynolds, J. Low Temp. Phys. **87**, Nos. 3/4, 343 (1992).

[14] H. F. Hess, Phys. Rev. B **34**, 3476 (1986).

[15] A. Lagendijk, I. F. Silvera, and B. J. Verhaar, Phys. Rev. B **33**, 626 (1986); H. T. C. Stoof, J. M. V. A. Koelman, and B. J. Verhaar, Phys. Rev. B **38**, 4688 (1988).

[16] C. R. Monroe, E. A. Cornell, C. A. Sackett, C. J. Myatt, and C. E. Wieman, Phys. Rev. Lett. **70**, 414 (1993).

[17] R. van Roijen, Ph. D. thesis, University of Amsterdam (1989).

[18] I. D. Setija, H. G. C. Werij, O. J. Luiten, M. W. Reynolds, T. W. Hijmans, and J. T. M. Walraven, Phys. Rev. Lett. **70**, 2257 (1993).

Chapter 2

Magnetic Trap

2.1 Introduction

For the present experiments we use the magnetostatic trap built by van Roijen *et al.* [1, 2]. We modified the trap to enable trapping of larger H↑ samples and to increase the flexibility of the trapping parameters. The magnetic field configuration is a so-called Ioffe trap [3] (see Fig. 2.1), originally developed in the 1960's for trapping plasmas and first proposed for neutral atom trapping by Pritchard [4].

The Ioffe trap configuration consists of two circular coaxial coils with parallel currents, and four linear conductors (Ioffe bars), arranged symmetrically around the symmetry axis of the circular coils at equal radial distances with equal currents in alternating directions. In the central region the circular coils produce a $\vec{B}$ field nearly parallel to the axis, which has a minimum in $|\vec{B}|$ in the axial direction, but which is not confining in the radial direction. The four Ioffe bars generate a $\vec{B}$ field perpendicular to the axis. This field is zero on the axis and its magnitude $|\vec{B}|$ increases linearly with the radial distance from the axis. If the current through the four linear conductors is large enough the two $\vec{B}$ fields add up to a minimum in $|\vec{B}|$ in the center.

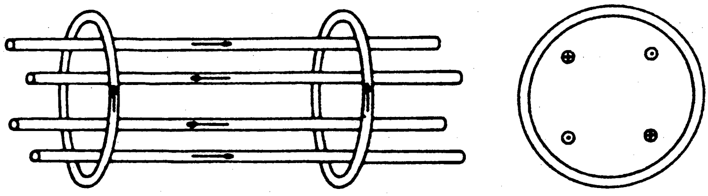

Figure 2.1: Side and end view of a Ioffe trap [5].

Although several other minimum-B-field configurations are conceivable [5], the Ioffe trap combines a number of properties which suit our purposes: 1) To trap a substantial amount of H$\uparrow$ atoms a potential well depth comparable to the adsorption energy of H atoms on the surrounding surface ($\epsilon_a/k_B = 1\,\mathrm{K}$ for H on liquid ^{4}He) is required. In our Ioffe trap a maximum magnetic well depth of 1.5 T can be achieved, which is equivalent to 1 K trapping energy for H$\uparrow$ atoms. 2) The trap should preferably have a single central minimum in $|\vec{B}|$ to obtain maximum localization of the atoms. This rules out ring configurations commonly used in neutron and plasma trapping. 3) The field in the minimum $|\vec{B}|_{min}$ should be non-zero for several reasons, which exclude the much simpler two-coil quadrupole trap: First, a non-zero minimum prevents particle loss due to nonadiabatic spin-flips (Majorana transitions) [6], which can become a significant loss mechanism at very low temperatures. Second, for the spectroscopic diagnostics (Chapter 6) and optical manipulation of the trapped gas [7] it is important that the different Zeeman components of the absorption lines are spectrally separated. Third, a non-zero minimum ensures that the bottom of the potential well is "flat" in all directions, so that at very low temperatures it is still possible to trap a sizeable amount of atoms. In our Ioffe trap an extra trimming coil is included halfway between the two axially confining coils, enabling adjustment of $|\vec{B}|_{min}$ independent of the currents through the confining coils, thus providing control over the Zeeman splitting of the absorption lines. Furthermore, tunability of $|\vec{B}|_{min}$ makes it possible to investigate the B-field dependence of the various collisional decay proceses. 4) The combination of axial confinement using dipole coils and quadrupolar radial confinement results in a trapping field that depends in a well-behaved manner on position, allowing analytical calculation of the particle energy distribution function in the trap and related quantities. This will be discussed in Chapter 3. Near the minimum the trap potential is harmonic which makes the description of particle motion simple, in particular at very low temperatures. In fact it is possible in our trap to construct a potential well that is harmonic *and* isotropic near the minimum, as will be discussed in Sect. 2.3.3. It can be shown [5] that this is only possible in magnetostatic traps with $|\vec{B}|_{min} \neq 0$, of which the Ioffe trap is probably the simplest realization.

In this chapter we will describe the main features of the actual trapping magnet and a method to calculate the generated $\vec{B}$ field. In this method the finite dimensions of the wire bundles and end effects of the Ioffe bars are taken into account explicitly without resorting to brute force numerical integration. We will also investigate the shape of the potential well near the minimum and discuss several examples of trapping geometries.

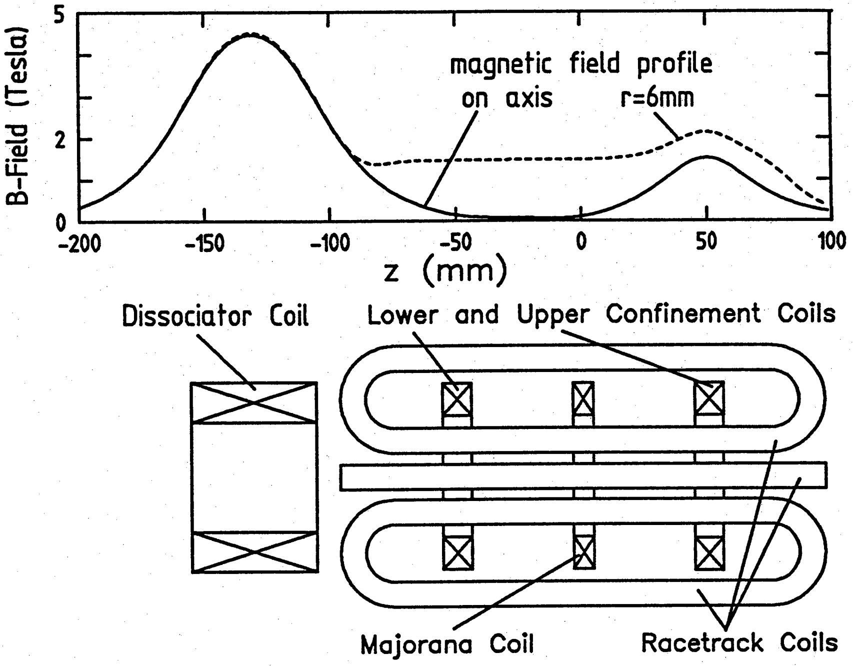

Figure 2.2: Lower part: Cross section view ($y = 0$) of the trapping magnet coils. The z-axis (from left to right) is pointing vertically upwards in reality. Upper part: Magnetic field along the z-axis if only the dissociator coil, the upper confinement coil, and the racetracks are energized with the maximum allowable currents. Solid line: field on axis. Dashed line: field 6 mm off axis.

2.2 The trapping magnet assembly

Our trapping magnet consists of four circular coils with a common symmetry axis, the z-axis, and four racetrack-shaped coils, orientated as shown in Fig. 2.2. All coils are wound with superconducting wire and have rectangular wire bundle cross sections. The entire trapping magnet assembly fits into a stainless steel tank which is filled with liquid ^{4}He at 4.2 K during operation. The magnet tank has a free accessible bore with a diameter of 40 mm for $z < -103$ mm and of 16 mm for $z > -103$ mm, inside which the experimental cell at $T \lesssim 0.2$ K is mounted (Chapter 4). A detailed description of the construction of the trapping magnet assembly, the winding of the coils, and the materials used is given in Ref. [2]. Here the discussion is restricted to the information that is necessary for the calculation of the magnetic field.

The four identical racetrack coils are electrically connected in series in such a way that a 90° rotation around the z-axis is equivalent to a reversal of the currents. Consequently, the racetracks generate a quadrupolar radially confining field. Each coil has 1680 windings (42 layers of 40), packed in a wire bundle of $10 \times 10\,\mathrm{mm}^2$. The straight parts of the coils extend from $z = -75\,\mathrm{mm}$ to $z = 75\,\mathrm{mm}$ and the centers of the inner bars and of the outer bars are at a radial distance of, respectively, 14 mm and 49 mm from the z-axis. Each inner bar is connected to the corresponding outer bar through semi-circular arcs. When the maximum current of 36 A is used, a radial $|\vec{B}|$ field gradient of 2.2 T/cm can be achieved inside the bore.

From left to right (in reality from bottom to top, see Fig. 4.1) we have four dipole coils (see Fig. 2.2), designated dissociator coil, lower confinement coil, Majorana coil, and upper confinement coil. The center of the Majorana coil defines $z = 0$. In the first trapping experiment [1] the upper and the lower confinement coils were electrically connected in series with equal current orientation. When combined with the racetracks this pair of, nearly identical, dipole coils generates a minimum in $|\vec{B}|$ on the axis near $z = 0$. The smaller Majorana coil at $z = 0$ can be used to adjust the value of $|\vec{B}|_{min}$ without altering the current through the confining coils. When the maximum current is sent through the confining coils and the racetracks, while simultaneously pulling the field minimum down to $|\vec{B}|_{min} = 0$ by means of the Majorana coil, a maximum well depth of 1.5 T can be achieved. Below the lower confinement coil a high field region ($\sim 4.5\,\mathrm{T}$) can be created by a large solenoid, the dissociator coil. In this high field region H atoms are produced in both electron-spin states and its purpose is to keep the high-field seeking $\mathrm{H}\!\downarrow$ atoms well separated from the $\mathrm{H}\!\uparrow$ atoms that get trapped in the field minimum.

If only the dissociator coil and the upper confinement coil are energized (see Fig. 2.2), the result is a much longer trapping region. In fact, the combination of the racetracks with any pair of the four dipole coils can be used to generate a B-field minimum on the axis. For this reason we decided to decouple the upper and the lower confinement coils. In the present setup all four dipole coils can be energized separately.

In Table 2.1 all information needed to calculate the exact field generated by the four dipole coils is summarized. Each coil can be characterized by the position z_c of the center, the length L over which it extends in the z direction, the inner radius a, the thickness t (the difference between inner and outer radius), the total number of windings N_w, the number of winding layers N_ℓ, and the maximum current I_{max}.

Table 2.1: Dipole coil parameters (see text) [8].

dipole coil	z_c (mm)	a (mm)	L (mm)	t (mm)	N_w	N_ℓ	I_{max} (A)
upper conf.	50	24	12	11.8	1813	45	40
lower conf.	-50	24	12	12.5	1726	45	40
Majorana	0	24	8	9.3	4335	78	5
dissociator	-131	22	50	16	7893	54	40

2.3 Calculation of the magnetic field

The eight trapping coils produce a complicated, highly inhomogeneous $\vec{B}$ field. For reliable spectroscopy of the trapped gas detailed knowledge of $\vec{B}(\vec{r})$ is required, not only because of the Zeeman shifts of the absorption lines, but also because the local absorption of the light depends strongly on the angle between the light polarization and $\vec{B}$. Furthermore, precise knowledge of $|\vec{B}(\vec{r})|$ is essential for the averaging of, for instance, the rates of collisional processes over the thermal density distribution of the trapped gas [1] and for the calculation of particle trajectories. Exact numerical calculation of the field using the law of Biot and Savart is time-consuming and does not yield much insight. Instead we use an approximation method in which the field is expanded in powers of the radial distance from the z-axis while taking full advantage of the symmetries of the trap configuration, a method also employed by the authors of Ref. [5]. For trap configurations with a single central minimum this expansion is a very natural method, as it yields the highest accuracy in the region with the largest particle concentration. Taking into account only the leading terms of the expansion we obtain closed expressions for $\vec{B}(\vec{r})$ which describe the field accurately in the entire trapping region.

2.3.1 Dipolar field

We will first calculate the field due to a single circular dipole coil with a wire bundle of rectangular cross section. The z-axis is the symmetry axis, the center is situated at $z = z_c$, and its dimensions are characterized by the inner radius a, the length L, and the thickness t. In the calculation we will assume a homogeneous current density $j = N_w I/(L\,t)$, where N_w is the number of windings and I is the current through a single wire. The field will be described in the cylindrical coordinates (ρ, ϕ, z).

In free space the magnetic field $\vec{B}$ can be derived from a scalar potential V:

$$\vec{B} = -\vec{\nabla} V = -\frac{\partial V}{\partial \rho}\vec{e}_\rho - \frac{1}{\rho}\frac{\partial V}{\partial \phi}\vec{e}_\phi - \frac{\partial V}{\partial z}\vec{e}_z. \tag{2.1}$$

Since $\vec{\nabla} \cdot \vec{B} = 0$, the potential V obeys Laplace's equation:

$$\Delta V = \frac{\partial^2 V}{\partial \rho^2} + \frac{1}{\rho}\frac{\partial V}{\partial \rho} + \frac{1}{\rho^2}\frac{\partial^2 V}{\partial \phi^2} + \frac{\partial^2 V}{\partial z^2} = 0. \tag{2.2}$$

Because the potential V is independent of ϕ (since $B_\phi = 0$) and because V is an even function of ρ, we may write the following expansion in powers of ρ:

$$V(\rho, \phi, z) = \sum_{n=0}^{\infty} a_{2n}(z)\, \rho^{2n}. \tag{2.3}$$

Substituting Eq. (2.3) into the Laplace equation (2.2), we find a recursion relation between the z-dependent coefficients $a_n(z)$:

$$4n^2 a_{2n}(z) = -a''_{2n-2}(z), \tag{2.4}$$

where the prime denotes differentiation with respect to z. Using Eqs. (2.4) and (2.1) the field $\vec{B}$ in an arbitrary point (ρ, ϕ, z) can now be written in terms of $a'_0(z) = -B_z(0,0,z)$:

$$\begin{aligned} B_\rho(\rho, \phi, z) &= -\tfrac{1}{2}B'_z(0,0,z)\rho + \tfrac{1}{16}B'''_z(0,0,z)\rho^3 + \cdots \\ B_z(\rho, \phi, z) &= B_z(0,0,z) - \tfrac{1}{4}B''_z(0,0,z)\rho^2 + \cdots \end{aligned} \tag{2.5}$$

Thus, in any axially symmetric configuration the entire magnetic field (in free space) is completely determined by the field on the axis, which can be obtained either by measurement or by calculation. The field on the z-axis of a single current loop of radius R, centered at $z = A$, with a current I, is given by the well-known law of Ampère

$$B_z(0,0,z) = \frac{\mu_0 I}{2R}\left(1 + \left(\frac{z-A}{R}\right)^2\right)^{-3/2}. \tag{2.6}$$

By integrating Eq. (2.6) over A from $A = z_c - L/2$ to $A = z_c + L/2$ and over R from $R = a$ to $R = a + t$, and assuming a homogeneous current density $j = N_w I/Lt$, we obtain an expression for the field on the axis due to a circular dipole coil with a rectangular wire bundle cross section:

$$\begin{aligned} B_z(0,0,z) &= \frac{\mu_0 N_w I a}{2Lt}\left\{x_2 \ln\left[\frac{x_2}{x_1}\frac{1+\sqrt{1+x_1^2}}{1+\sqrt{1+x_2^2}}\right]\right. \\ &- \left. x_4 \ln\left[\frac{x_4}{x_3}\frac{1+\sqrt{1+x_3^2}}{1+\sqrt{1+x_4^2}}\right]\right\}, \end{aligned} \tag{2.7}$$

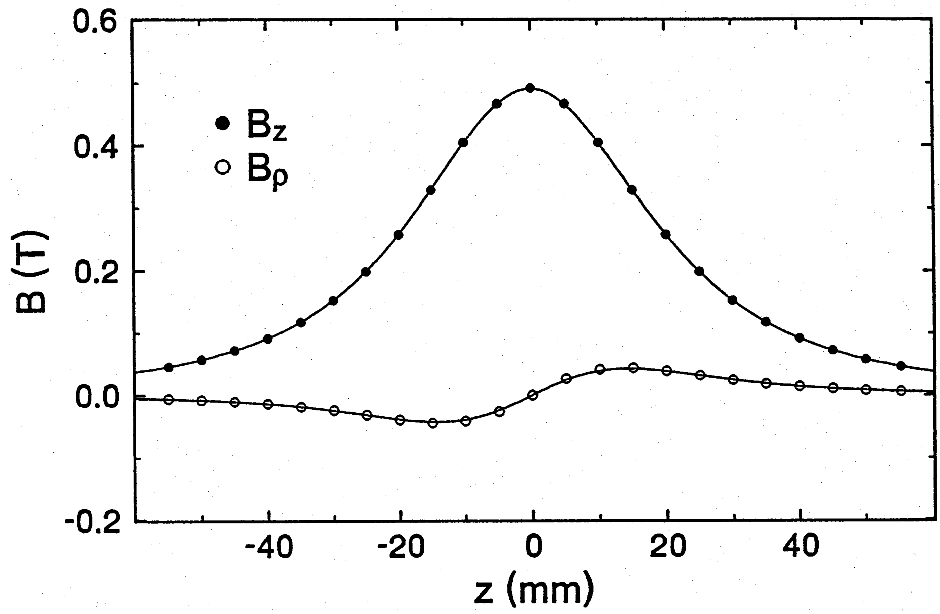

Figure 2.3: Calculated field components B_z and B_ρ versus z at $\rho = 6\,\mathrm{mm}$, generated by the Majorana coil operating at the maximum current $I_{max} = 5\,\mathrm{A}$. Solid line: analytical expression using the first two terms in the B_z expansion and the first term in the B_ρ expansion. Circles: exact numerical calculation.

where $x_1 = (z-z_c+L/2)/(a+t)$, $x_2 = (z-z_c+L/2)/a$, $x_3 = (z-z_c-L/2)/(a+t)$, and $x_4 = (z-z_c-L/2)/a$. Using expression (2.7) and its derivatives with respect to z, the expansion (2.5), and the information contained in Table 2.1, the magnetic field due to the four dipoles in the trap can be calculated to any degree of precision. It turns out that for our purposes it is sufficient to retain the first two terms in the B_z expansion and only the first term in the B_ρ expansion, requiring the first and the second z-derivative of expression (2.7). As an illustration of the accuracy of the method we compare in Fig. 2.3 the field of the Majorana coil at $\rho = 6\,\mathrm{mm}$ (the inner radius of the present experimental cell) calculated using the truncated expansion with the result of an exact numerical calculation, as a function of z. Clearly, the analytical expressions for B_z and B_ρ describe the dipolar field inside the trapping region very well: For $\rho < 6\,\mathrm{mm}$ the deviations in B_z and $|\vec{B}|$ are $< 1\%$, the deviations in B_ρ are $< 10\%$.

2.3.2 Quadrupolar field

For the calculation of the field of the racetrack coils we will use the scalar potential method again and we will start with some very general symmetry considerations: 1) Twofold symmetry implies $V(\rho,\phi,z)=V(\rho,\phi+\pi,z)$. 2) V is an even function of ρ. 3) Since $|\vec{B}|=0$ for $\rho=0$ we are free to choose $V(0,0,z)=0$ and 4) we are also free to choose the reference direction for the azimuthal angle in such a way that $B_\rho=-\partial V/\partial\rho=0$ for $\phi=0$, consistent with the orientation of the racetracks (see Fig. 2.2). Under these conditions V can be expanded in the following way:

$$V=\sum_{m=1}^{\infty}\sum_{n=1}^{\infty}\rho^{2m}b_{2m,2n}(z)\sin 2n\phi. \tag{2.8}$$

By substituting the expansion (2.8) in the Laplace equation (2.2), the following relations between the $b_{2m,2n}$-coefficients are obtained:

$$\begin{aligned} b_{2m,2n}(z) &= -\tfrac{1}{4(m^2-n^2)}b''_{2(m-1),2n}(z),\ m>n,\\ b_{2m,2n}(z) &= 0,\ m<n. \end{aligned} \tag{2.9}$$

These relations hold for any field with twofold symmetry. To calculate the field using the expansion (2.8), knowledge of the functions

$$b_{2m,2m}(z)=-(1/(2m)!)(\partial^{2m-1}B_\phi/\partial\rho^{2m-1})_{\rho=0,\phi=0}+\sum_{n=1}^{m-1}(2n/2m)b_{2m,2n}, \tag{2.10}$$

$m=1,2,\ldots$, is required. In lowest order, i.e., in the quadrupolar approximation, we find (using Eq. (2.1)):

$$\begin{aligned} B_\rho(\rho,\phi,z) &= 2b(z)\rho\sin 2\phi\\ B_\phi(\rho,\phi,z) &= 2b(z)\rho\cos 2\phi\\ B_z(\rho,\phi,z) &= b'(z)\rho^2\sin 2\phi, \end{aligned} \tag{2.11}$$

where $b(z)\equiv -b_{2,2}(z)$. If b does not depend too strongly on z, it follows from Eqs. (2.11) that $|\vec{B}|$ is in lowest order proportional to ρ, a well-known property of quadrupolar fields.

In our case we have the extra symmetry that a rotation over 90° around the z-axis corresponds to a reversal of the currents: $V(\rho,\phi+\pi/2,z)=-V(\rho,\phi,z)$. Consequently, only terms with odd n contribute in the expansion (2.8), i.e., terms with $\sin 2\phi$, $\sin 6\phi$, $\sin 10\phi$, etc. This means that the first corrections to the expressions (2.11) that cannot be calculated using the derivatives of $b(z)$ are of the order $\sim\rho^5$ and therefore negligible for small ρ. Hence it is reasonable to assume that Eqs. (2.11) suffice to describe the field of the racetracks and that only $b(z)=(1/2)(\partial B_\phi/\partial\rho)_{\rho=0,\phi=0}$ needs to be calculated for the experimental parameters.

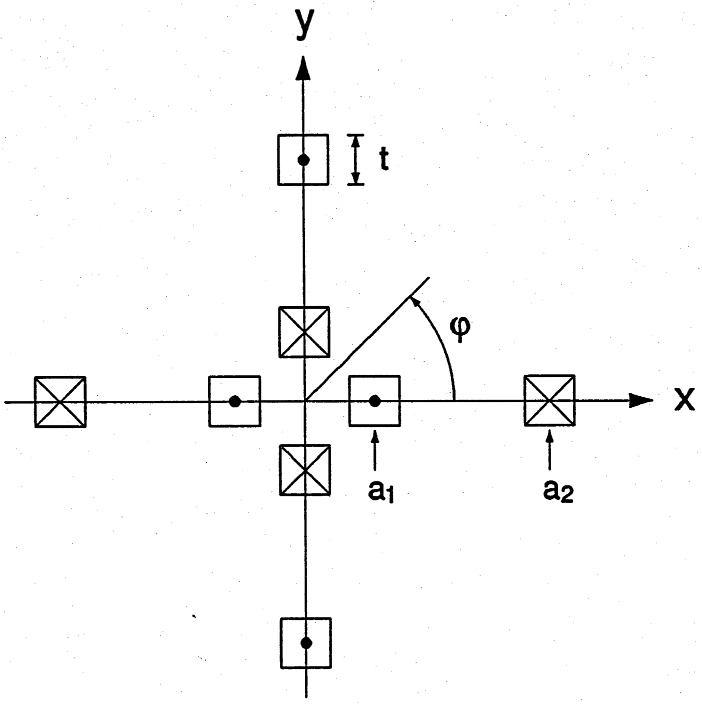

Figure 2.4: Cross section view of the racetracks at $z = 0$. The centers of the four inner bars are at $\rho = a_1 = 14\,\mathrm{mm}$, the centers of the four outer bars at $\rho = a_2 = 49\,\mathrm{mm}$, the square wire bundles have a thickness $t = 10\,\mathrm{mm}$. The directions of the currents are also indicated.

To investigate the influence of higher order terms in ρ in more detail, we first calculate the field for the (2-dimensional) case when the straight sections of the racetracks extend from $z = -\infty$ to $z = \infty$ (see Fig. 2.4). The field due to four infinitely long wires coinciding with the centers of the inner bars of the racetracks ($\rho = a_1 = 14\,\mathrm{mm}$) can be calculated quite straightforwardly in cartesian coordinates. Subsequently, the scalar potential is also easily derived,

$$V_{4w}(x,y) = -\mathrm{Im}\frac{\mu_0 I}{2\pi}\ln(\frac{a_1^2 + (x+iy)^2}{a_1^2 - (x+iy)^2}), \tag{2.12}$$

and can be expanded either in cartesian or in cylindrical coordinates:

$$V_{4w} \;=\; -\mathrm{Im}\frac{2\mu_0 I}{\pi}\sum_{n=0}^{\infty}\frac{(x/a_1 + iy/a_1)^{4n+2}}{4n+2}$$

$$= -\frac{2\mu_0 I}{\pi}\sum_{n=0}^{\infty}\frac{(\rho/a_1)^{4n+2}\sin[(4n+2)\phi]}{4n+2}. \qquad (2.13)$$

The expansion in cylindrical coordinates is precisely of the form we expected on grounds of symmetry considerations. Cartesian coordinates, however, are more convenient for calculating the scalar potential due to the rectangular shape of the four Ioffe bars: We assume a homogeneous current density $j = N_w I/t^2$, with I the current through a single wire, and integrate Eq. (2.13) over the square wire bundle cross sections. After rewriting the result in cylindrical coordinates and regrouping the series in terms of $(\rho/a_1)^n \sin n\phi$, we arrive at the following expression for the scalar potential due to four square, infinitely long Ioffe bars:

$$\begin{aligned} V_{4b} &= -\frac{\mu_0 N_w I}{\pi}\{[1-\frac{1}{12}(\frac{t}{a_1})^4](\frac{\rho}{a_1})^2\sin 2\phi \\ &+ [\frac{1}{3}-\frac{7}{10}(\frac{t}{a_1})^4](\frac{\rho}{a_1})^6\sin 6\phi + O[(\frac{\rho}{a_1})^{10}]\}. \qquad (2.14)\end{aligned}$$

Using Eq. (2.1), the corresponding magnetic field components become:

$$\begin{aligned} B_\rho(\rho,\phi) &= \frac{2\mu_0 N_w I}{\pi a_1}\{[1-\frac{1}{12}(\frac{t}{a_1})^4]\frac{\rho}{a_1}\sin 2\phi \\ &+ [1-\frac{21}{10}(\frac{t}{a_1})^4](\frac{\rho}{a_1})^5\sin 6\phi + O[(\frac{\rho}{a_1})^9]\} \\ & \qquad\qquad\qquad\qquad\qquad\qquad\qquad\qquad (2.15) \\ B_\phi(\rho,\phi) &= \frac{2\mu_0 N_w I}{\pi a_1}\{[1-\frac{1}{12}(\frac{t}{a_1})^4]\frac{\rho}{a_1}\cos 2\phi \\ &+ [1-\frac{21}{10}(\frac{t}{a_1})^4](\frac{\rho}{a_1})^5\cos 6\phi + O[(\frac{\rho}{a_1})^9]\}.\end{aligned}$$

From Eqs. (2.15) it follows that the relative contribution to $|\vec{B}|$ of the nonlinear terms in ρ is of the order $[1-(131/60)(t/a_1)^4](\rho/a_1)^4$, which is $< 1\%$ for $\rho < 5\,\mathrm{mm}$ and clearly negligible in most cases.

The expressions (2.15) should describe the quadrupolar field in the $z = 0$ plane of the actual trap fairly well, as end effects due to the finite length of the racetracks are presumably small at $z = 0$ (see Fig. 2.2). The field of the outer bars can be obtained trivially by changing the sign of expressions (2.15) and replacing a_1 by a_2. We calculated the quadrupolar field of the real racetracks at $z = 0$ as a function of ρ for $\phi = 0°$ and $\phi = 45°$ by exact numerical integration and compared this to the field obtained using the analytical expressions for infinitely long Ioffe bars (see Fig. 2.5). As expected, the magnitude of the field increases linearly (within $\sim 1\%$) up to $\rho = 5\,\mathrm{mm}$, beyond this distance non-linearities become significant. The field gradient is $\alpha = 2.2\,\mathrm{T/cm}$ if the racetracks are operated at the maximum current

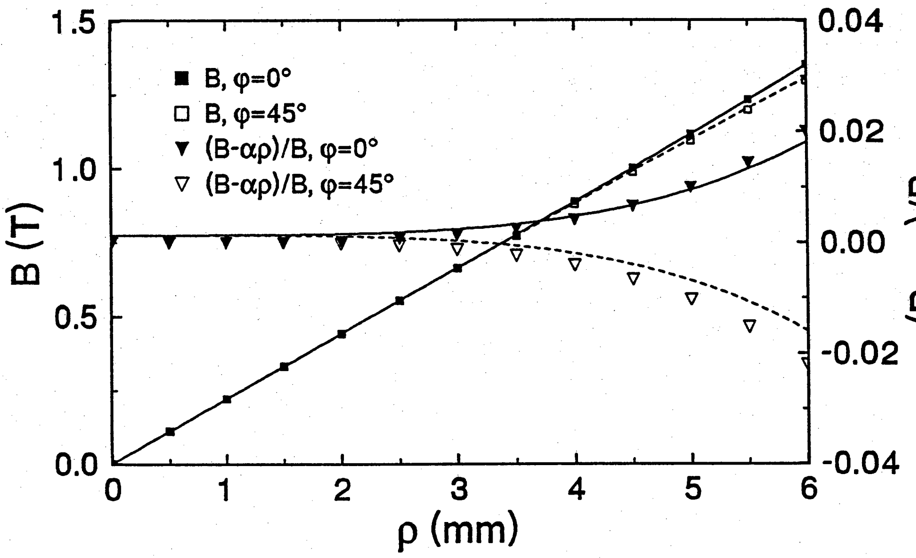

Figure 2.5: Calculated field magnitude B of the racetracks operating at $I_{max} = 36\,\mathrm{A}$ as a function of ρ at $z = 0$ for $\phi = 0°$ and $\phi = 45°$ (squares). Also shown is the relative deviation $(B - \alpha\rho)/B$, $\alpha = 2.21\,\mathrm{T/cm}$, from a purely quadrupolar field (triangles). Solid line: analytical expression for $\phi = 0°$. Dashed line: analytical expression for $\phi = 45°$.

$I_{max} = 36\,\mathrm{A}$. The analytical expressions describe the quadrupolar field very well at $z = 0$, including the non-linearities. The largest deviations, $< 1\%$, occur at $\rho = 6\,\mathrm{mm}$ for $\phi = 45°$ and are probably due to finite length effects of the racetracks.

The non-linearities in the quadrupolar field, associated with the "higher harmonics" ($\sin 6\phi$, $\sin 10\phi$, etc.), only play a role in parts of the trapping region where the hydrogen atom density is so strongly suppressed that they can be completely neglected in the description of many properties. The effects on the quadrupolar field connected with the finite length of the racetracks, however, can only be neglected if the trapping region falls well within the z-range of the straight sections of the racetracks, as is the case, for instance, for the trapping geometry used by van Roijen *et al.* [1, 2]. In the longer trapping geometries used in the present experiments (see, for instance, Fig. 2.2) part of the trapping field is determined by the semi-circular arcs at the end of the Ioffe bars. These end effects are taken into account properly if we describe the field with Eqs. (2.11), so the function $b(z) = (1/2)(\partial B_\phi/\partial\rho)_{\rho=0,\phi=0}$ is required. This function has been calculated numerically and is accurately described

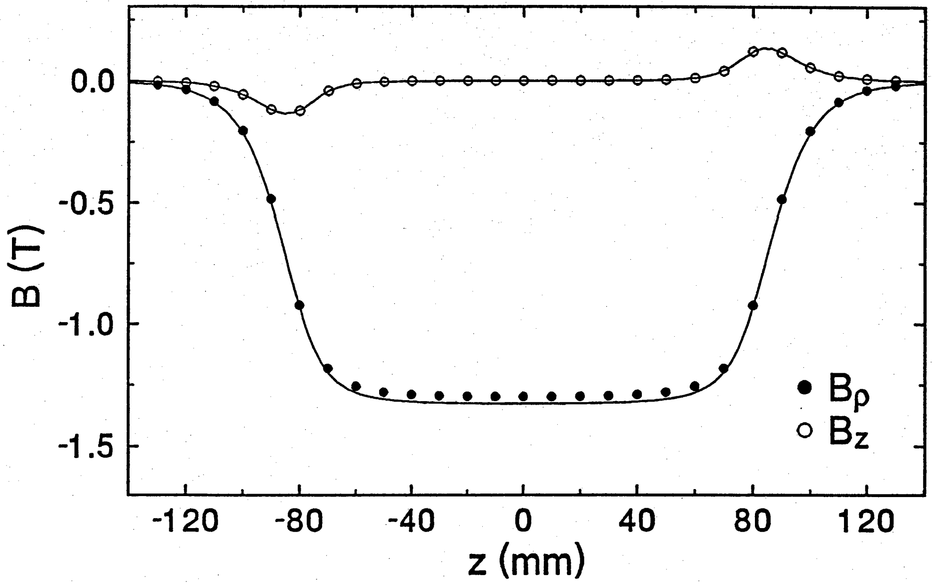

Figure 2.6: Calculated magnetic field components versus z of the racetracks ($I = I_{max} = 36\,\mathrm{A}$) for $\rho = 6\,\mathrm{mm}$ and $\phi = 45°$. Circles: exact numerical calculation. Solid lines: closed expressions.

by the following form:

$$b(z) = b_0(I/I_{max})[\tanh(\frac{z_0 - z}{z_1}) + \tanh(\frac{z_0 + z}{z_1})], \tag{2.16}$$

where $b_0 = 1.104\,\mathrm{T/cm}$, $z_0 = 86.6\,\mathrm{mm}$, and $z_1 = 15.5\,\mathrm{mm}$ have been obtained by fitting Eq. (2.16) to the numerically calculated values. As a check we calculated the field of the racetracks as a function of z for $\rho = 6\,\mathrm{mm}$, $\phi = 45°$, using Eqs. (2.11) and (2.16), and compared this to an exact numerical calculation, as shown in Fig. 2.6. The expressions (2.11) and (2.16) clearly describe the behavior of both field components very well. The small systematic deviation in B_ρ is due to the ρ^5 field contributions (see Fig. 2.5), which have not been taken into account. Apparently, finite length effects become significant for $|z| > 40\,\mathrm{mm}$, manifesting themselves in a decrease of the radial field gradient, but also in the appearance of a B_z field component.

2.3.3 Field near the minimum

Most of the complexities and details of the trapping field which have been discussed in the previous sections are only relevant for trapped gas samples at relatively high temperatures. At low temperatures most hydrogen atoms reside near the minimum where the description of the field is much simpler. If we approximate the dipolar field on the z-axis by $B_z = B_0 + \beta(z - z_0)^2$, where $\beta = (1/2)(\partial^2 B_z(0,0,z)/\partial z^2)_{z=z_0}$, with $z = z_0$ the position of the minimum, and the quadrupolar field by using a constant radial field gradient α, then, adding Eqs. (2.5) and (2.11), the field components are [5]:

$$\begin{aligned} B_\rho &= -\alpha\rho\sin 2\phi - \beta\rho(z - z_0) \\ B_\phi &= -\alpha\rho\cos 2\phi \\ B_z &= B_0 + \beta(z - z_0)^2 - \tfrac{1}{2}\beta\rho^2, \end{aligned} \tag{2.17}$$

and therefore

$$B = \sqrt{[B_0 + \beta(z - z_0)^2]^2 + [\alpha^2 - \beta B_0 + 2\alpha\beta(z - z_0)\sin 2\phi]\rho^2 + (1/4)\beta^2\rho^4}. \tag{2.18}$$

A direct consequence of Eq. (2.18) is that a finite radial field gradient is needed for trapping: The field will only be confining if $\alpha^2 > \beta B_0$. Typical values for the present experiments are $B_0 = 0.1\,\mathrm{T}$, $\alpha = 2.2\,\mathrm{T/cm}$, and $\beta = 0.022\,\mathrm{T/cm}^2$, in which case Eq. (2.18) may be approximated by

$$B = \sqrt{[B_0 + \beta(z - z_0)^2]^2 + [\alpha^2 + 2\alpha\beta(z - z_0)\sin 2\phi]\rho^2}. \tag{2.19}$$

For many applications, the $\sin 2\phi$ term in Eq. (2.19) can also be neglected, yielding an expression that allows the analytical calculation of some important properties of the trapped gas (Chapter 3).

Very close to the minimum, i.e., for $(B - B_0)/B_0 \ll 1$, Eq. (2.18) may be expanded, yielding to lowest order in z and ρ:

$$B = B_0 + \beta(z - z_0)^2 + \frac{1}{2}(\frac{\alpha^2}{B_0} - \beta)\rho^2. \tag{2.20}$$

The harmonic approximation (2.20) of the field is only valid if the temperature T of the trapped gas is much smaller than $\mu_B B_0/k_B$, for instance for $B_0 = 0.1\,\mathrm{T}$ if $T \ll 0.067\,\mathrm{K}$. One of the nice features of the Ioffe trap is that the radial field gradient α can be adjusted independently of β and B_0, allowing the construction of an *isotropic* harmonic $|\vec{B}|$ field by setting

$$\alpha = \sqrt{3\beta B_0}. \tag{2.21}$$

For instance, for the typical values $B_0 = 0.1\,\mathrm{T}$ and $\beta = 0.022\,\mathrm{T/cm}^2$ this means lowering the radial field gradient to $\alpha = 0.08\,\mathrm{T/cm}$ ($I = 1.3\,\mathrm{A}$).

Table 2.2: Currents through the trapping coils, defining different trapping geometries.

geometry	racetracks	dissociator	lower conf.	Majorana	upper conf.
Short	36 A	35 A	40 A	-4.5 A	40 A
Long	36 A	35 A	0	-1 A	27 A
Isotrop. harm.	1.3 A	35 A	0	-1 A	27 A

2.4 Examples of trapping geometries

We will now discuss two trapping geometries, calculated using Table 2.1 and the closed expressions (2.5), (2.7), (2.11), and (2.16). The currents which are sent through the trapping coils and which define the different trapping geometries, are tabulated in Table 2.2. The signs of the dipole coil currents indicate their relative orientations.

In Fig. 2.7 the trapping geometries are shown. The $|\vec{B}|$ field is calculated as a function of z for four radial distances ranging from $\rho = 0\,\text{mm}$ to $\rho = 6\,\text{mm}$, the latter corresponding to the inner radius of the present experimental cell.

The "short" geometry was used in the trapping experiment of van Roijen *et al.* [1, 2]. The minimum is located at $z_0 = 0.5\,\text{mm}$ and the field near the minimum can be characterized by (see Sect. 2.3.3) $B_0 = 0.05\,\text{T}$, $\alpha = 2.2\,\text{T/cm}$, and $\beta = 0.13\,\text{T/cm}^2$. The lowest field on the wall surrounding the trapping region is $B_w = 1.33\,\text{T}$, resulting in an effective well depth of $\epsilon_{tr}/k_B \equiv \mu_B(B_w - B_0)/k_B = 0.85\,\text{K}$. The shape of the potential is described very well by Eq. (2.19) up to relatively high fields, which simplifies calculations of several properties of the trapped gas (Chapter 3). A striking feature is the secondary minimum, located at $z = -74\,\text{mm}$, which plays a role in the transmission spectroscopy of the trapped gas (Chapter 6). By changing the current through the Majorana coil from $-5\,\text{A}$ to $+5\,\text{A}$, B_0 can be set anywhere between 0 and 1 T.

The "long" geometry is the trapping configuration most commonly used in the experiments described in this thesis, in particular for the measurements of evaporative cooling, described in Chapter 7. The effective trapping depth is $\epsilon_{tr}/k_B = 0.82\,\text{K}$, the minimum is located at $z_0 = -7.5\,\text{mm}$, and the field near the minimum can be characterized by $B_0 = 0.1\,\text{T}$, $\alpha = 2.2\,\text{T/cm}$, and $\beta = 0.022\,\text{T/cm}^2$. The main advantage of this geometry is the large number of atoms that can be trapped ($\sim 2.5\times$ more than in the "short" geometry at a given temperature and maximum density of the trapped gas), a property that can be decisive for the optical detection of gas samples at very low temperatures. Due to the combination of the strong axially

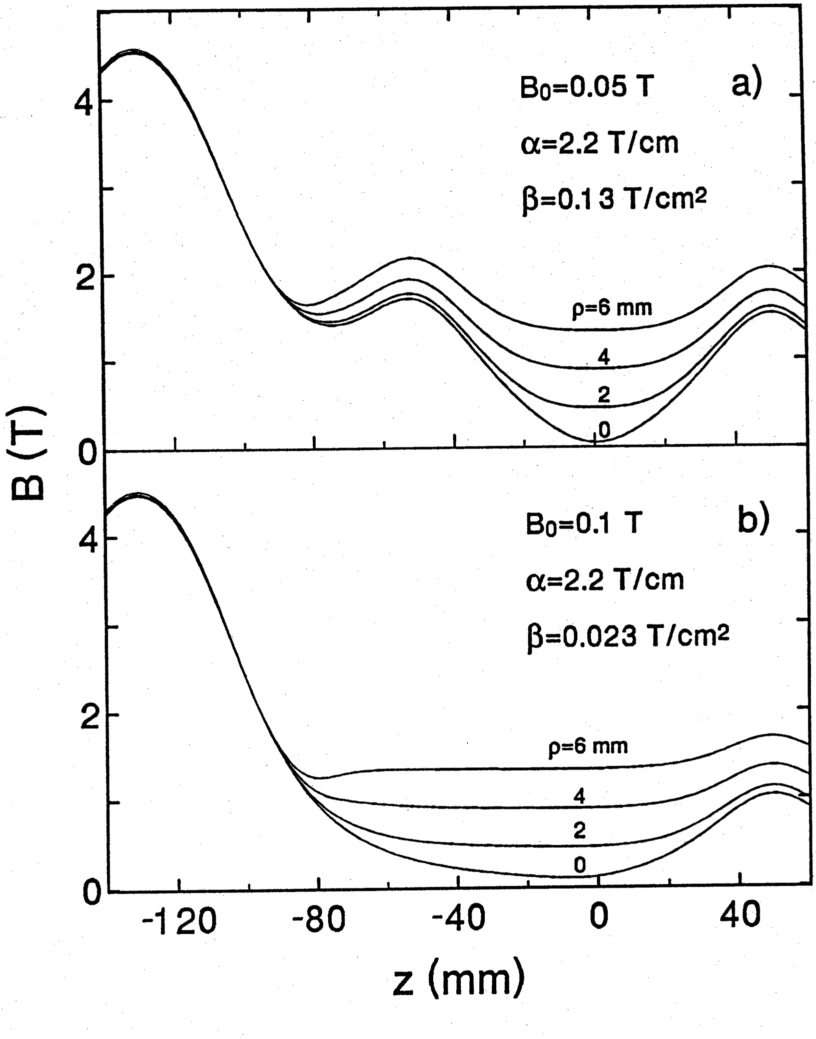

Figure 2.7: $|\vec{B}|$ versus z for $\rho = 0, 2, 4$, and 6 mm. a) "Short" trapping geometry. b) "Long" trapping geometry.

confining field of the dissociator coil and the rapidly decreasing radial field gradient for $z < -50\,\mathrm{mm}$, the $B_w = 1.33\,\mathrm{T}$ equipotential surface more or less coincides with the cylindrical side wall of the experimental cell for $z < 0$. This feature is especially useful in the description of evaporative cooling mediated by the cell walls (Chapter 7).

References

[1] R. van Roijen, J. J. Berkhout, S. Jaakkola, and J. T. M. Walraven, Phys. Rev. Lett. **61**, 931 (1988).

[2] R. van Roijen, Ph. D. thesis, University of Amsterdam (1989).

[3] Y. V. Gott, M. S. Ioffe, and V. G. Tel'kovskii, Nucl. Fusion, 1962 Suppl., Pt. 3, 1045 (1962).

[4] D. E. Pritchard, Phys. Rev. Lett. **51**, 1336, (1983).

[5] T. Bergeman, G. Erez, and H. J. Metcalf, Phys. Rev. A **35**, 1535 (1987).

[6] T. H. Bergeman, P. McNicholl, J. Kycia, H. Metcalf, and N. L. Balazs, J. Opt. Soc. Am. B **6**, 2249 (1989).

[7] I. D. Setija, H. G. C. Werij, O. J. Luiten, M. W. Reynolds, T. W. Hijmans, and J. T. M. Walraven, Phys. Rev. Lett. **70**, 2257 (1993).

[8] R. van Roijen, S. Jaakkola, J. T. M. Walraven, unpublished (1987).

Chapter 3

Trapped Atomic Hydrogen

In this chapter the properties of magnetostatically trapped H samples are discussed relevant to the experiments described in this thesis. The essential features of hydrogen trapping which were already addressed by Van Roijen *et al.* [1, 2] are reviewed, and some new insights are added. In Sect. 3.1 the potential energy of hydrogen atoms in a static magnetic field is treated. In Sect. 3.2 the thermodynamics of trapped hydrogen samples in thermal equilibrium is discussed. A simple but accurate approximative method is presented for calculating analytically the partition function of a gas sample in a Ioffe trap. This permits us to calculate directly several important (quasi-)equilibrium properties like the specific heat and the effective volume of the sample. In this section extra attention is paid to the influence of the vicinity of the cell walls on the sample properties, which is especially important for the description of the evaporative cooling process (Chapter 7). We also dwell on the calculation of the sample-averaged collisional rates, which determine the equilibration time and, ultimately, the lifetime of the gas. In Sect. 3.3 the processes of the loading of the trap and the thermalization of the H$\uparrow$ sample are discussed and a justification for the assumption of thermal equilibrium is given. In Sect. 3.4 several particle loss mechanisms are briefly discussed, in particular collisional relaxation. Finally, in Sect. 3.5, the heat-balance equation of the trapped sample is derived and the processes that affect the temperature of the gas are described.

3.1 Potential energy

Confinement of neutral particles in magnetostatic traps relies on the Zeeman interaction $E_Z = -\vec{\mu} \cdot \vec{B}(\vec{r})$ between the magnetic moments $\vec{\mu}$ of the particles and a nonuniform static magnetic field $\vec{B}(\vec{r})$. If the magnetic field experienced by a particle does not change too rapidly, the magnetic moment $\vec{\mu}$ will adiabatically follow the magnetic field vector $\vec{B}(\vec{r})$ and the energy of the particle in the external field will only depend on $B(\vec{r}) \equiv |\vec{B}(\vec{r})|$. More precisely, if the time dependent field experienced by a particle only contains Fourier components with frequencies much smaller than the transition frequencies $\Delta\omega_Z$ between the various Zeeman sublevels, the particle will remain adiabatically in the same Zeeman sublevel it started out with. In practice this condition is always fulfilled, except in zero-field regions [3]. This is of no concern to us, as we only consider field configurations with a non-zero minimum in $|\vec{B}|$. Particles in a Zeeman sublevel whose energy increases with $|\vec{B}|$, the so-called "low-field seekers", experience a force in the direction of decreasing field magnitude and can in principle be captured in a region with a minimum in $|\vec{B}|$. The potential energy of these particles with respect to the field minimum is

$$U_p(\vec{r}) = E_Z(\vec{r}) - E_Z(\vec{r}_0), \tag{3.1}$$

where $\vec{r}_0$ is the position of the minimum.

The interaction of hydrogen atoms in their electronic groundstate ($1^2S_{1/2}$) with an externally applied static magnetic field is somewhat more complicated due to the hyperfine interaction between the electron spin $\vec{s}$ and the proton spin $\vec{\imath}$. The interaction is described by the following effective Hamiltonian [4]:

$$H_{eff} = (g_e\mu_B\vec{s} - g_n\mu_n\vec{\imath}) \cdot \vec{B} + a_h\vec{\imath} \cdot \vec{s}. \tag{3.2}$$

where μ_B and μ_n are the Bohr magneton and the nuclear magneton, g_e and g_n the corresponding g-factors, and a_h the hyperfine splitting in zero-field, $a_h/k_B = 0.068\,\mathrm{K}$. Diagonalization of H_{eff} yields four hyperfine states, labeled a, b, c, and d in order of increasing energy (see Fig. 3.1):

$$\begin{array}{rcl} E_a & = & -\frac{1}{4}a_h - \frac{1}{2}a_h[1 + (\mu^+B/a_h)^2]^{1/2} \\ E_b & = & \frac{1}{4}a_h - \frac{1}{2}\mu^-B \\ E_c & = & -\frac{1}{4}a_h + \frac{1}{2}a_h[1 + (\mu^+B/a_h)^2]^{1/2} \\ E_d & = & \frac{1}{4}a_h + \frac{1}{2}\mu^-B, \end{array} \tag{3.3}$$

where $\mu^\pm = g_e\mu_B \pm g_n\mu_n$. The four eigenstates may be expressed in the $|m_s, m_i\rangle$ basis:

$$\begin{array}{rcl} |a\rangle & = & \sin\theta|\uparrow\downharpoonright\rangle - \cos\theta|\downarrow\upharpoonright\rangle \\ |b\rangle & = & |\downarrow\downharpoonright\rangle \\ |c\rangle & = & \cos\theta|\uparrow\downharpoonright\rangle + \sin\theta|\downarrow\upharpoonright\rangle \\ |d\rangle & = & |\uparrow\upharpoonright\rangle, \end{array} \tag{3.4}$$

where $\uparrow$, $\downarrow$, $\upharpoonright$, and $\downharpoonright$ denote respectively $m_s = 1/2$, $m_s = -1/2$, $m_i = 1/2$, and $m_i = -1/2$, and the hyperfine mixing angle θ is defined by

$$\tan 2\theta \equiv a_h/(\mu^+B) \approx a_h/(2\mu_BB). \tag{3.5}$$

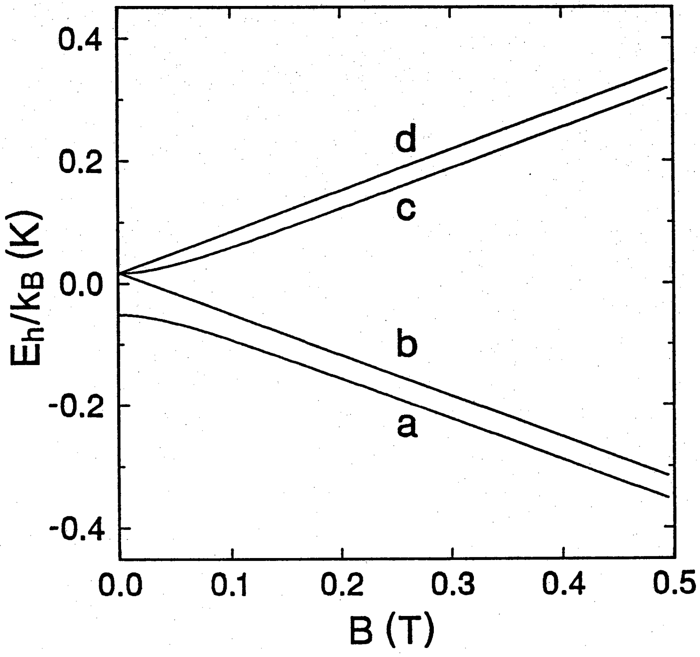

Figure 3.1: The hyperfine energies (in temperature units) of atomic hydrogen in the $1^2S_{1/2}$ electronic ground state as a function of magnetic field.

For $B \gg a_h/\mu^+ = 0.0507\,\mathrm{T}$ the Zeeman term is dominant in H_{eff} and the eigenstates approach pure $|m_s, m_i\rangle$ states. In the rest of this thesis we will replace both μ^+ and μ^- by $2\mu_B$, which is a good approximation ($< 1\%$ error). It is clear from Fig. 3.1 that atoms in the low-field seeking c and d states (H↑) will be attracted by a B-field minimum, and can be trapped, whereas atoms in the a and b states (H↓) will be repelled. Analogous to Eq. (3.1), the potential energy of an H atom in a trapping field is defined as

$$U_p(\vec{r}) = E_h(\vec{r}) - E_h(\vec{r}_0), \tag{3.6}$$

where h denotes the hyperfine state.

3.2 Equilibrium thermodynamics

Our method of calculating thermodynamic properties of the trapped sample hinges on two simplifying assumptions: First, the trapped gas can be treated as a classical ideal gas. This is true to a very good approximation because the interaction between spin-polarized H atoms is very weak and the thermal de Broglie wavelength is always much smaller than the mean interparticle spacing. Also the quantum mechanical level spacing in the trapping potential is always several orders of magnitude smaller than the average kinetic energy. Second, the trapped gas is in a state of internal thermal equilibrium; this is not *a priori* clear and a justification will be given in Sect. 3.3.

In addition we will make use of an approximative description of the magnetic field in a Ioffe trap, which enables the analytical calculation of the density of states and the partition function of the gas. From the partition function we derive expressions for the effective volume and the specific heat of the trapped gas.

We will pay extra attention in the following to the influence of boundary effects on the sample-averaged properties of the trapped gas. Usually these effects are assumed negligible, as the particle density at the edge of the potential well is strongly suppressed [1, 2, 5]. We will show, however, that they can be quite significant.

3.2.1 Density distributions

In thermal equilibrium the phase space distribution $f(\vec{r}, \vec{p})$ of a classical ideal gas in a potential field $U_p(\vec{r})$ is described by

$$f(\vec{r}, \vec{p}) = n_0 (2\pi m k_B T)^{-3/2} \exp[-(U_p(\vec{r}) + p^2/2m)/k_B T]. \tag{3.7}$$

The reference density n_0 is chosen in such a way that the phase space distribution function f is normalized to the total particle number $N = \int d^3r\, d^3p\, f(\vec{r}, \vec{p})$, where the integration is over the available phase space. By integrating over the entire momentum space we obtain the density distribution

$$n(\vec{r}) = n_0 \exp[-U_p(\vec{r})/k_B T]. \tag{3.8}$$

In the case of a complete thermal distribution in momentum space n_0 is equal to the density at the position $\vec{r_0}$ of the minimum in U_p. For d state atoms in a static magnetic field the potential energy takes the simple form $U_p(\vec{r}) = \mu_B[B(\vec{r}) - B_0]$, where $B_0 \equiv |\vec{B}(\vec{r_0})|$ is the field magnitude at the minimum. The potential energy of c state atoms has a more complicated dependence on $B(\vec{r})$ (see Eq. (3.3)), but for $B_0 \geq 0.1\,\mathrm{T}$, as is the case for most of the experiments described in this thesis, it is approximated quite accurately by the same expression as used for d state atoms.

The well depth of the trap ϵ_{tr} is equal to the potential energy corresponding to the minimum field strength B_w on the surfaces surrounding the trapping region. For d state atoms $\epsilon_{tr} = \mu_B(B_w - B_0)$. In the "long" trapping geometry $B_0 = 0.1\,\mathrm{T}$ and $B_w = 1.33\,\mathrm{T}$ (see Chapter 2), so at a typical temperature $T = 0.1\,\mathrm{K}$ the density of

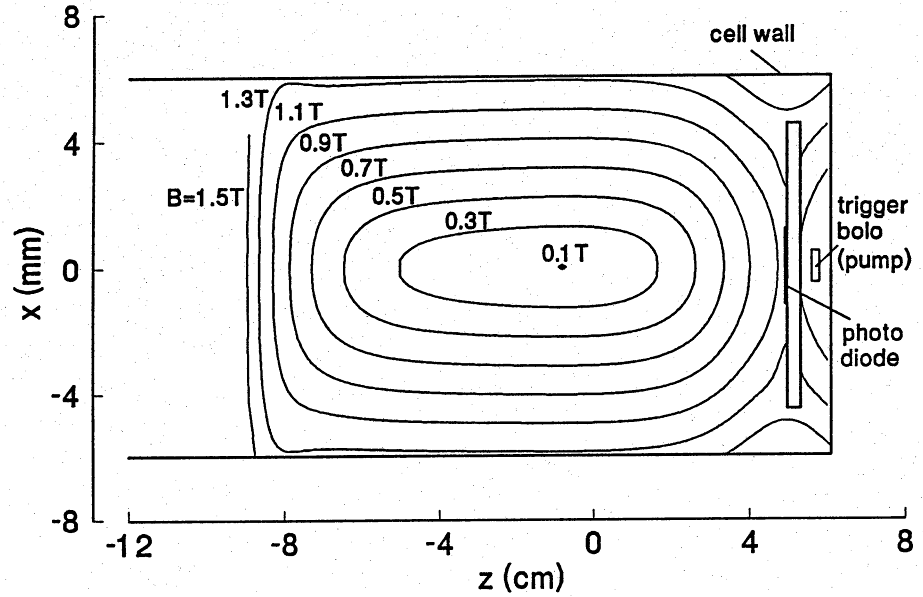

Figure 3.2: Magnetic field contours of the "long" trapping geometry. The cell walls are also indicated. Note the difference in x and z scales.

H↑ atoms at the wall is suppressed by $\exp(\epsilon_{tr}/k_BT) \approx 3 \times 10^3$ and the assumption that the wall influence is negligible is fully justified. At a temperature $T = 0.2\,\mathrm{K}$, the wall density is suppressed to $\sim 2\%$ of the central density, which still seems small. However, we will show that in the latter case the wall influence can no longer be neglected for the calculation of a number of quantities.

To include the cell wall explicitly in the density distribution, we make use of an approximation which is based on the particular shape of our trapping potential. In Fig. 3.2 the magnetic field contours of the "long" trapping geometry are shown. As the cylindrical side wall nearly coincides with the $B_w = 1.33\,\mathrm{T}$ equipotential surface, and the side wall surface area comprises the major part of the total wall surface area (note the length/width ratio of the trapping field), we may replace the cell wall in our calculations by the B_w equipotential surface.

To obtain a more realistic density distribution than $n(\vec{r})$ given in Eq. (3.8), we consider two limiting cases:

1) The cell wall is a perfectly reflective surface, so the density distribution is

simply a Maxwell-Boltzmann distribution, truncated in configuration space:

$$\begin{aligned} n_t(\vec{r}) &= n_0 \exp[-U_p(\vec{r})/k_B T] \quad , \quad U_p < \epsilon_{tr}, \\ n_t(\vec{r}) &= 0 \quad , \quad U_p > \epsilon_{tr}. \end{aligned} \tag{3.9}$$

2) The cell wall is a perfectly adsorptive surface. Strictly speaking all particles will then be adsorbed on the wall in thermal equilibrium.

Let us suppose, however, that we have a trapped gas surrounded first by perfectly reflective walls. After the gas has reached thermal equilibrium, the walls are switched instantaneously from perfectly reflective to perfectly adsorptive. The atoms with orbits intersecting the cell walls will be removed within a single oscillatory period. As these are the most energetic atoms, the average energy per trapped atom immediately after switching on the pumping walls will be lower than before. Thermalizing interatomic collisions will drive the remaining gas to a new equilibrium state at a lower temperature. The same collisions will also scatter more particles into wall-intersecting orbits, which are lost. Let us assume that the internal (collisional) equilibration rate of the sample is much faster than the rate at which the sample is depleted by the pumping wall. In that case the pumped sample will slowly lose particles and evolve in quasi-equilibrium towards lower temperatures. This process is called evaporative cooling.

If a particle comes out of a collision event with a total energy (kinetic energy plus potential energy) greater than ϵ_{tr}, then it has the possibility to reach the adsorbing wall. Taking into account constants of motion other than the total energy, which are associated with symmetries in the potential U_p, and the fact that the particle in a second collision may be scattered back into a low-energy trajectory, it is not clear how large the probability is to reach the wall. To enable an approximate determination of the distribution function of the pumped sample we make the second assumption that this probability is unity, i.e., any particle given a total energy $> \epsilon_{tr}$ will be removed. We shall return to these questions in more detail in Chapter 7. Starting from a thermal equilibrium phase space distribution (3.7) and integrating $f(\vec{r},\vec{p})$ over all momenta for which $U_p(\vec{r}) + p^2/2m \le \epsilon_{tr}$, we obtain the density distribution n_p of a sample pumped by the cell wall:

$$n_p(\vec{r}) = n(\vec{r})[\mathrm{erf}(\sqrt{\frac{\epsilon_{tr} - U_p(\vec{r})}{k_B T}}) - \frac{2}{\sqrt{\pi}}\sqrt{\frac{\epsilon_{tr} - U_p(\vec{r})}{k_B T}} \exp(-\frac{\epsilon_{tr} - U_p(\vec{r})}{k_B T})]. \tag{3.10}$$

Of course this distribution is described much more conveniently in phase space, where it is simply a Maxwell-Boltzmann distribution truncated at the $U_p(\vec{r}) + p^2/2m = \epsilon_{tr}$ surface. However, for some applications (e.g. spectroscopy of the gas during evaporative cooling, Chapter 7) an explicit expression is required. The density distribution (3.10) was used by Helmerson *et al.* [24] in their analysis of

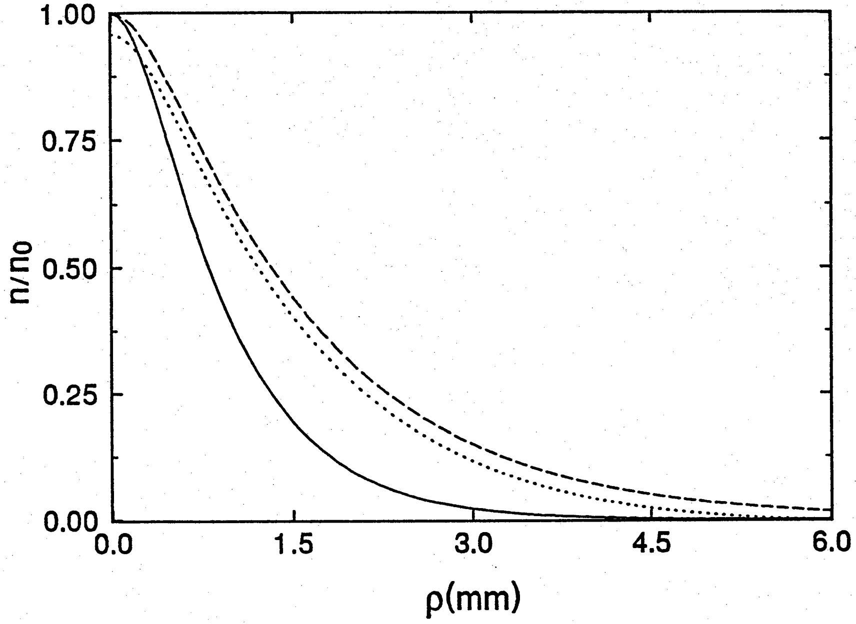

Figure 3.3: Density distributions n_t/n_0 and n_p/n_0 at $z = z_0$ as a function of the radial distance ρ from the center of the trap. Solid curve: n_t/n_0 for $T = 0.1\,\mathrm{K}$; dashed curve: n_t/n_0 for $T = 0.2\,\mathrm{K}$; dotted curve: n_p/n_0 for $T = 0.2\,\mathrm{K}$. The cylindrical side wall is at $\rho = 6\,\mathrm{mm}$.

experiments with magnetically trapped Na atoms. When U_p approaches ϵ_{tr}, the density n_p goes smoothly to zero as a function of U_p. Note that the pumped density distribution as defined by Eq. (3.10) is still characterized by a temperature T and a density n_0. However n_0 is no longer the central density, $n_p(\vec{r}_0) < n_0$, and strictly speaking T cannot be interpreted as the thermodynamic temperature of the system. In the case of a pumped distribution T and n_0 are convenient parameters characterizing an essentially non-equilibrium distribution.

A word of caution may be necessary on the terminology used: Both distributions considered are truncated Maxwell-Boltzmann distributions, one in phase space and one in configuration space, but in the following the term *truncated distribution* is reserved for distributions truncated in configuration space.

In Fig. 3.3 the radial density distributions n_t/n_0 and n_p/n_0 in our trap at $z = z_0$ are plotted for the gas temperatures $T = 0.1\,\mathrm{K}$ and $0.2\,\mathrm{K}$. At $T = 0.2\,\mathrm{K}$ there is a significant effect of the pumping wall on the density distribution, also in regions far from the wall. At $T = 0.1\,\mathrm{K}$ the difference between n_t and n_p is negligible. The sample is best described in terms of the truncated distribution n_t during the loading of the trap, when the wall temperature is relatively high ($\gtrsim$0.15 K) and the H$\uparrow$ gas is in thermal equilibrium with the wall (Sect. 3.3). The pumped distribution n_p should be used, for instance, when the wall temperature is low ($\lesssim$0.08 K) and the gas is evaporatively cooled.

3.2.2 Density of states

Before turning to the partition functions associated with the particle distributions discussed in the previous section, it is useful to first discuss the density of states in a Ioffe trap. In general, the density of states of a potential well U_p can be written as

$$\rho(\epsilon) = 2\pi(2m)^{3/2} \int_{U_p(\vec{r})\leq\epsilon} \sqrt{\epsilon - U_p(\vec{r})}\, d^3r. \tag{3.11}$$

Here the normalization is chosen in such a way that $\rho(\epsilon)d\epsilon$ is equal to the infinitesimal phase space volume occupied by the positions and momenta $(\vec{r}, \vec{p})$ for which $\epsilon < U_p(\vec{r}) + p^2/2m < \epsilon + d\epsilon$. Since we know the exact magnetic field $B(\vec{r})$ (see Chapter 2) and the B-dependence of the potential energy U_p (Sect. 3.1), the density of states $\rho(\epsilon)$ for both c and d state atoms can be calculated numerically. However, this procedure does not yield much insight and can be quite time-consuming, for instance when continuously changing field configurations are involved. The calculations can be simplified considerably by assuming a pure d state gas and using a convenient approximate description of the B-field.

In a Ioffe trap near the trap center ($\rho = 0, z = z_0$) the field magnitude B can be approximated by (see Chapter 2)

$$B \approx \sqrt{[B_0 + \beta(z - z_0)^2]^2 + \alpha^2\rho^2}, \tag{3.12}$$

where $B_0 = 0.1\,\mathrm{T}$, $\alpha = 2.2\,\mathrm{T/cm}$, and $\beta = 0.023\,\mathrm{T/cm^2}$, for the "long" geometry. Using Eqs. (3.11) and (3.12), we obtain a simple analytical expression for the density of states of a pure d state gas in a Ioffe trap:

$$\rho(\epsilon) = \frac{(2m\pi^2)^{3/2}}{2\mu_B^{5/2}\alpha^2\sqrt{\beta}}\epsilon^3(1 + \frac{2\mu_B B_0}{\epsilon}). \tag{3.13}$$

The value of β used corresponds to the exact axial field curvature at the minimum of the trap, so the approximation should work best at low energies. The description at higher energies can be improved by adjusting the values of β and z_0 appropriately. The approximation gives the most accurate results in field geometries whose axial field profiles have a close resemblance to the required parabolic shape (Eq. (3.12)), such as, for instance, the "short" geometry (see Chapter 2). However, as will be shown in Sects. 3.2.4 and 3.2.5, it works quite well for the "long" trapping geometry. When the axial field profile deviates very much from the required parabolic shape, as is for instance the case in the trapping experiments at MIT [5], the field may be approximated by the more general form

$$B \approx \sqrt{(B_0 + \beta|z - z_0|^{\delta})^2 + \alpha^2\rho^2}, \tag{3.14}$$

which still allows an analytical approach. For the trap used at MIT, for instance, $\delta \gg 2$. In our description we will restrict ourselves to the quadratic axial field approximation (3.12), which yields relatively simple expressions, while being sufficiently accurate for our case.

Another practical quantity is the "magnetic density of states" $\rho_M(B)$. Analogous to the energy density of states $\rho(\epsilon)$, $\rho_M(B')dB'$ is defined to be equal to the infinitesimal volume in configuration space occupied by the positions $\vec{r}$ for which $B' < B(\vec{r}) \leq B' + dB'$. In other words:

$$\rho_M(B') = \frac{d}{dB'}\int_{B(\vec{r})<B'} d^3r. \tag{3.15}$$

Using the field approximation Eq. (3.12), the magnetic density of states ρ_M can be derived in a straightforward manner:

$$\rho_M(B) = \frac{4\pi}{\alpha^2\sqrt{\beta}}[(B - B_0)^{3/2} + B_0(B - B_0)^{1/2}]. \tag{3.16}$$

The magnetic density of states is useful for calculating the partition function of a system of particles which is only limited in configuration space and for calculating sample averages of B-dependent quantities like, for instance, collisional relaxation rates. Furthermore, it is used for the interpretation of transmission spectra (Chapter 6) and the calculation of the evaporative cooling rate (Chapter 7).

3.2.3 Partition functions

The partition function of a classical ideal gas of N particles in a potential U_p is given by

$$Z = \frac{z^N}{N!}, \tag{3.17}$$

where the "single-particle partition function" z is defined as

$$z = h^{-3}\int \exp[-(U_p(\vec{r}) + p^2/2m)/k_BT]d^3p\,d^3r. \tag{3.18}$$

We will now calculate the partition functions z associated with the different particle distributions discussed in Sect. 3.2.1, using the approximation for the density of states developed in Sect. 3.2.2.

For an infinite distribution of particles, not disturbed by walls ($B_w \to \infty$), the partition function z_∞ can be written as

$$z_\infty = h^{-3} \int_0^\infty \rho(\epsilon) \exp(-\epsilon/k_BT) d\epsilon, \tag{3.19}$$

where ρ is the density of states as defined in Eq. (3.11). Using Eq. (3.13), z_∞ for a gas of d state atoms in a potential of the form (3.12) is readily obtained:

$$z_\infty = (T/T_1)^4 [1 + \frac{2}{3}(T_0/T)], \tag{3.20}$$

where $k_BT_0 = \mu_B B_0/k_B$ and $k_BT_1 = [(2m\pi^2)^{-3/2} h^3 \mu_B^{5/2} \alpha^2 \beta^{1/2}/3]^{1/4}$ can be interpreted as the temperature for which the thermal wavelength of the trapped particles in a Ioffe trap with $B_0 = 0$ becomes equal to their average classical oscillation amplitude. For the "long" geometry $T_1 = 2.87\,\mu$K and $T_0 = 0.067$ K.

To obtain an expression for the partition function z_p of a gas sample pumped by the cell wall we only need to replace the upper bound of the integration (3.19) by ϵ_{tr}, the potential energy on the surface of the cell wall, as we assume that all particles with a total energy greater than ϵ_{tr} will actually reach the wall and be removed. Using again Eq. (3.13), we find:

$$z_p = z_\infty \left\{ 1 - e^{-\eta} [1 + \eta + \frac{1}{2}\eta^2 + \frac{1}{6} \frac{\eta^3}{1 + \frac{2}{3}\xi\eta}] \right\}, \tag{3.21}$$

where we have introduced the dimensionless quantities $\eta \equiv \epsilon_{tr}/k_BT$ and $\xi \equiv B_0/(B_w - B_0)$. For the trap configuration under consideration $\eta T = 0.82$ K and $\xi = 0.08$. For $\eta = 4$ ($T \approx 0.2$ K) the correction due to the presence of the walls is $\sim 40\%$, which is quite significant. For $\eta \geq 10$ ($T \leq 0.08$ K) the correction is less than 1% and the factor in curly brackets may be replaced by unity.

The calculation of the partition function z_t of a gas surrounded by perfectly reflective walls, when the distribution is only truncated in configuration space, requires a different approach. In this case it is more convenient to carry out the integrations over momentum and configuration space separately:

$$z_t = \lambda_{th}^{-3} \int_{U_p(\vec{r}) \leq \epsilon_{tr}} \exp[-U_p(\vec{r})/k_BT] d^3r. \tag{3.22}$$

Here $\lambda_{th} \equiv h/\sqrt{2\pi m k_BT}$ is the thermal deBroglie wavelength; the integration over momentum space is contained in the factor λ_{th}^{-3}. For a pure d state gas Eq. (3.22) can be written as

$$z_t = \lambda_{th}^{-3} \int_0^{B_w} \rho_M(B) \exp[-\mu_B(B - B_0)/k_BT] dB, \tag{3.23}$$

where ρ_M is the magnetic density of states as defined in Eq. (3.15). Using the approximative form (3.16), we find:

$$z_t = z_\infty \left\{ 1 - \mathrm{erfc}\sqrt{\eta} - 2\sqrt{\eta/\pi}\frac{1+\frac{2}{3}(1+\xi)\eta}{1+\frac{2}{3}\xi\eta} e^{-\eta} \right\}. \tag{3.24}$$

For $\eta \geq 4$, the $\mathrm{erfc}\sqrt{\eta}$ term is negligible. For $\eta = 4$ and $\xi = 0.08$ the correction due to the presence of the walls in this distribution amounts to $\sim 13\%$.

As a first application we determine the fraction f_{ev} that is removed from a distribution in thermal equilibrium with the surrounding reflective walls, when the wall surfaces are switched to a perfectly adsorptive state. This "evaporation" fraction may be written as $f_{ev} = (z_t - z_p)/z_t$, which for $\eta \geq 4$ can be accurately approximated by

$$f_{ev} = e^{-\eta} \left\{ 1 + \eta + \frac{1}{2}\eta^2 + \frac{1}{6}\frac{\eta^3}{1+\frac{2}{3}\xi\eta} - 2\sqrt{\eta/\pi}\frac{1+\frac{2}{3}(1+\xi)\eta}{1+\frac{2}{3}\xi\eta} \right\}. \tag{3.25}$$

We find that for $\eta = 4$ ($T \approx 0.2\,\mathrm{K}$ in our trap) and $\xi = 0.08$ approximately 30% of the particles is removed immediately after switching on the evaporation. For $\eta = 8$ ($T \approx 0.1\,\mathrm{K}$) this fraction is $\sim 3\%$. Note that the evaporation fraction f_{ev} is independent of the detailed shape of the potential well, it only depends on $\eta = \epsilon_{tr}/k_BT$ and $\xi = B_0/(B_w - B_0)$.

The determination of the partition function is an important result enabling a straightforward derivation of the thermodynamic functions of the trapped gas. In general, it can be applied to the description of processes which are slow in comparison to the collisional equilibration rate. In this thesis the main application of the thermodynamic description is a quantitative analysis of the evaporative cooling process (Chapter 7). In the following sections we will use the expressions we have obtained to calculate the most basic sample-averaged quantities, the effective volume and the internal energy of a trapped sample.

3.2.4 Effective volume and sample dimensions

The effective volume of the sample is a practical quantity which is closely related to the single-particle partition function z. In general we can define the effective volumes of order $\ell = 1, 2, 3, \ldots$ by

$$V_{\ell e} \equiv \int^{V_{geo}} [n(\vec{r})/n_0]^\ell d^3r, \tag{3.26}$$

where the integration is over the geometrical volume V_{geo}, which is bounded by the cell walls. The effective volume of order $\ell = 1$ is simply given by $V_{1e} = N/n_0$, where N is the number of trapped particles. The effective volume of order $\ell = 2$ is useful when discussing sample-averaged rates of binary interatomic collisions (Sect. 3.2.6).

For thermal distributions not truncated in momentum space the simple relation $V_{\ell e}(T) = V_{1e}(T/\ell)$ holds.

The single-particle partition function z (Eq. (3.18)) and the first-order effective volume V_{1e} are by definition related through $V_{1e} = z\lambda_{th}^3$. Using Eq. (3.20) we can immediately write the expression for the first-order effective volume of a pure d state gas in an infinite potential well of the form (3.12):

$$V_{1e}^{\infty} = V_0(T/T_{tr})^{5/2}[1 + \frac{2}{3}(T_0/T)]. \tag{3.27}$$

Here $V_0 = 3\pi^{3/2}\alpha^{-2}\beta^{-1/2}(B_w - B_0)^{5/2}$, $T_{tr} = \epsilon_{tr}/k_B$, and $T_0 = \mu_B B_0/k_B$. For the "long" geometry $V_0 = 38\,\mathrm{cm}^3$, $T_{tr} = 0.82\,\mathrm{K}$, and $T_0 = 0.067\,\mathrm{K}$. The effect of the presence of the cell walls can be taken into account with the same correction factors as in Eqs. (3.24) and (3.21):

$$V_{1e}^{t} = V_{1e}^{\infty}\left\{1 - \mathrm{erfc}\sqrt{\eta} - 2\sqrt{\eta/\pi}\frac{1 + \frac{2}{3}(1+\xi)\eta}{1 + \frac{2}{3}\xi\eta}e^{-\eta}\right\}, \tag{3.28}$$

and

$$V_{1e}^{p} = V_{1e}^{\infty}\left\{1 - e^{-\eta}[1 + \eta + \frac{1}{2}\eta^2 + \frac{1}{6}\frac{\eta^3}{1 + \frac{2}{3}\xi\eta}]\right\}, \tag{3.29}$$

where the superscripts t and p refer as usual to distributions truncated in configuration space and pumped distributions, respectively.

To check the accuracy of the approximative method we calculated numerically the exact first-order effective volume V_{1e}^t of a d state gas as a function of temperature, using the experimental B field, and compared this to the approximative analytical expression (3.28) (see Fig. 3.4). Using $V_0 = 42\,\mathrm{cm}^3$ we find that the approximative expression (3.28) agrees within 1% with the exact calculation for $0.05 \le T \le 0.25\,\mathrm{K}$, which is the relevant temperature range for the experiments described in this thesis. Also shown in Fig. 3.4 is V_{1e}^{∞}, calculated using Eq. (3.27) with $V_0 = 38\,\mathrm{cm}^3$, which describes the first-order effective volume accurately for $T \ll 0.05\,\mathrm{K}$ and is also useful for making rough estimates at higher temperatures.

For convenience we also introduce here some length scales which are measures for the linear dimensions of a sample in an axially symmetric potential. The effective axial length ℓ_{eff} may be defined as

$$\ell_{eff} \equiv \int_{-\infty}^{\infty} n(0,z)/n_0\,dz, \tag{3.30}$$

where $n(\rho, z)$ is the density at the point (ρ, z). Using the approximate expression (3.12) for the B-field in our Ioffe trap, we find for a d state gas

$$\ell_{eff} = \sqrt{\pi k_B T/\mu_B\beta}. \tag{3.31}$$

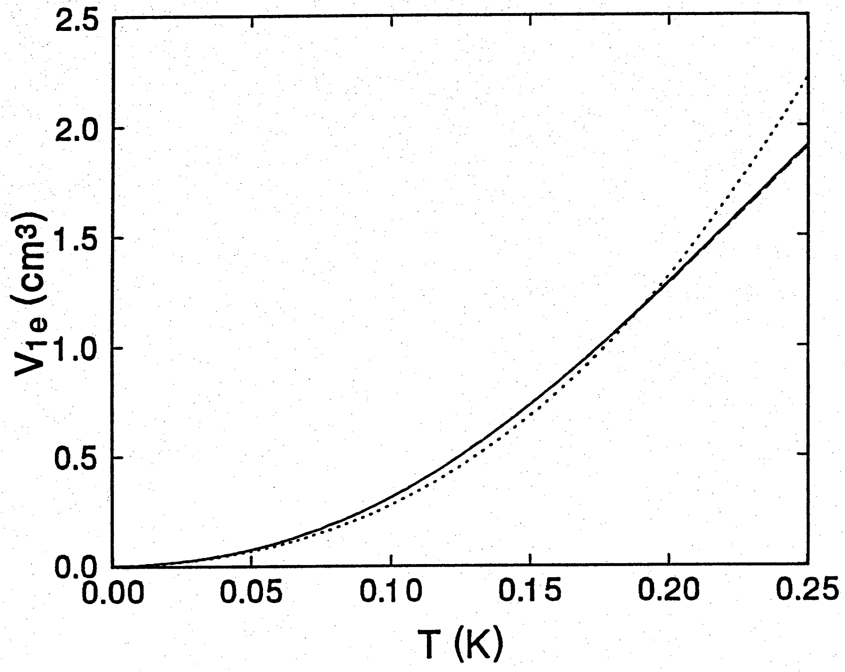

Figure 3.4: Effective volume V^t_{1e} in the "long" geometry versus temperature. Solid curve: numerically calculated V^t_{1e} using experimental B-field; dashed curve: V^t_{1e} from analytical expression (3.28) with $V_0 = 42\,\mathrm{cm}^3$, $\eta T = 0.82\,\mathrm{K}$, and $\xi = 0.08$; dotted curve: V^∞_{1e} of Eq (3.27) with $V_0 = 38\,\mathrm{cm}^3$.

For $\beta = 0.023\,\mathrm{T/cm}^2$ ("long" geometry), the effective axial length $\ell_{eff}/\sqrt{T} = 14\,\mathrm{cmK}^{-1/2}$, so at $T = 0.1\,\mathrm{K}$ $\ell_{eff} \approx 4\,\mathrm{cm}$. The effective area A_{eff} in the $z = z_0$ plane may be defined as

$$A_{eff} \equiv \int_0^\infty 2\pi\rho\, n(\rho, z_0)/n_0\, d\rho, \tag{3.32}$$

and the effective sample radius ρ_{eff} by

$$\rho_{eff} \equiv \sqrt{A_{eff}/\pi}. \tag{3.33}$$

Using again Eq. (3.12), one may easily derive for a d state gas

$$\rho_{eff} = \frac{\sqrt{2}k_B T}{\mu_B \alpha}\sqrt{1 + T_0/T}. \tag{3.34}$$

The potential experienced by the particles is harmonic for temperatures $T \ll T_0$. The ratio between the effective length and width of the sample is then independent of temperature: $\ell_{eff}/2\rho_{eff} = \sqrt{\pi\alpha^2/8\beta B_0}$, which means for the "long" geometry $\ell_{eff}/2\rho_{eff} \approx 30$. If $T \gg T_0$, then the effective sample radius is proportional to the temperature: $\rho_{eff} = \sqrt{2}k_BT/\alpha\mu_B$. For the "long" geometry we then find $\rho_{eff}/T \approx 1\,\mathrm{cmK}^{-1}$.

3.2.5 Internal energy

The internal energy E of a classical ideal gas in thermal equilibrium can be expressed in terms of z, the single-particle partition function:

$$E = Nk_BT^2\frac{1}{z}\frac{\partial z}{\partial T}. \tag{3.35}$$

Using Eq. (3.20) we easily obtain the internal energy E_∞ of a pure d state gas in an infinite potential of the form (3.12):

$$\frac{E_\infty}{Nk_BT} = 4\frac{1+\frac{1}{2}(T_0/T)}{1+\frac{2}{3}(T_0/T)}, \tag{3.36}$$

where $k_BT_0 = \mu_BB_0$. Note that the internal energy is independent of the Ioffe trap parameters α and β (or V_0). For $T \ll T_0$ the average energy $E_\infty \approx 3Nk_BT$, reflecting the approximately harmonic trapping potential experienced by d state atoms at very low energies (see Chapter 2). For the "long" geometry ($B_0 = 0.1\,\mathrm{T}$) at $T = 0.2\,\mathrm{K}$, $E_\infty/Nk_BT = 3.82$. Using Eqs. (3.21) and (3.24) we can also derive expressions for the internal energy E_t of a sample truncated by reflective walls:

$$\frac{E_t}{Nk_BT} = \frac{E_\infty}{Nk_BT} - \frac{4}{3\sqrt{\pi}}\frac{z_\infty}{z_t}\eta^{5/2}e^{-\eta}[1+\xi+\frac{\frac{2}{3}\xi}{1+\frac{2}{3}\xi\eta}], \tag{3.37}$$

and for the internal energy E_p of a sample surrounded by adsorptive walls:

$$\frac{E_p}{Nk_BT} = \frac{E_\infty}{Nk_BT} - \frac{1}{6}\frac{z_\infty}{z_p}\frac{\eta^4e^{-\eta}}{1+\frac{2}{3}\xi\eta}[1+2\xi+\frac{\frac{2}{3}\xi}{1+\frac{2}{3}\xi\eta}]. \tag{3.38}$$

Note that the internal energies of the truncated and the pumped distributions are also independent of the Ioffe trap parameters α and β. The temperature dependence is completely determined by B_0 and B_w. In the limit $T \ll T_0$ ($\xi\eta \gg 1$) the expressions for a harmonic potential are obtained. The internal energies E_∞/Nk_BT, E_t/Nk_BT, and E_p/Nk_BT, calculated using respectively Eqs. (3.36), (3.37), and (3.38) with $B_0 = 0.1\,\mathrm{T}$ and $B_w = 1.33\,\mathrm{T}$ ($\xi = 0.08$ and $\eta T = 0.82\,\mathrm{K}$), are plotted in Fig (3.5) as a function of temperature. Clearly, the corrections due to the presence of the cell wall can be quite substantial in the temperature range relevant to the experiments described in this thesis ($0.05\,\mathrm{K} < T < 0.2\,\mathrm{K}$). Also shown in Fig. 3.5 is the exact internal energy of a truncated sample, E_t/Nk_BT, calculated numerically

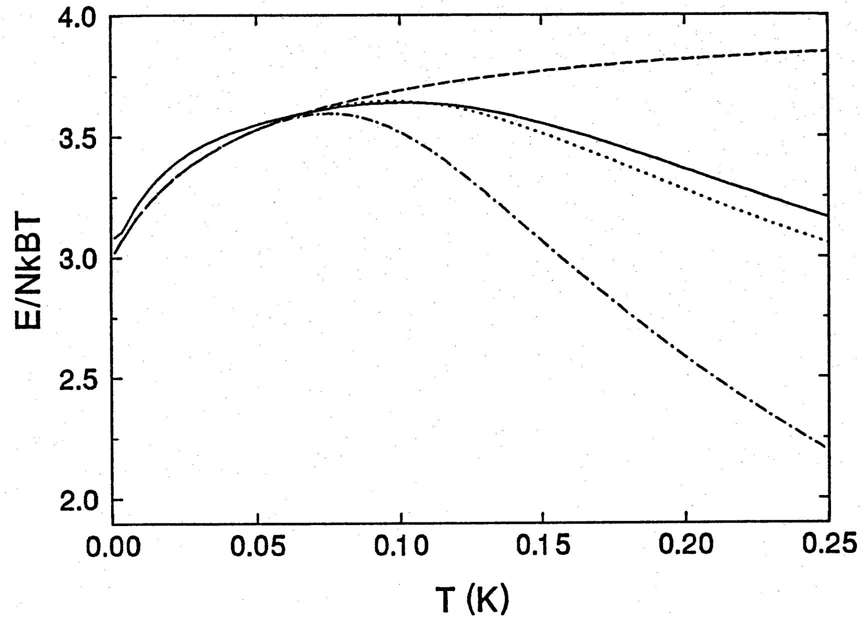

Figure 3.5: Internal energy of the trapped gas in units Nk_BT versus temperature. Dashed curve: E_∞/Nk_BT; dotted curve: E_t/Nk_BT; dash-dotted curve: E_p/Nk_BT. All three broken curves were calculated using the analytical expressions based on the approximation of the B-field. Solid curve: numerically calculated $E_t(T)/Nk_BT$ using the experimental B-field of the "long" geometry.

using the experimental B-field. The analytical expression (3.37), based on the approximation of the B-field, agrees within 7% with the exact numerical calculation for $T \leq 0.2\,\mathrm{K}$. We would like to stress that there are no adjustable parameters in Eq. (3.37); the differences arise from the deviations in the detailed *shape* of the experimental field from the approximative form (3.12).

When the distribution is truncated only in configuration space, the internal energy E can be split up into a kinetic energy $(3/2)Nk_BT$ and a potential energy $\gamma_{1e}Nk_BT$, where $\gamma_{1e} \equiv (T/V_{1e})(\partial V_{1e}/\partial T)$. One can easily show that for a pumped distribution (truncated in phase space) the equality $E = (\gamma_{1e}+3/2)Nk_BT$ also holds. In the latter case, however, the two terms can no longer be identified as pure kinetic energy and potential energy contributions. We can define more generally effective average potential energies of order $\ell = 1, 2, 3, \ldots$ by

$$\gamma_{\ell e}k_BT \equiv V_{\ell e}^{-1} \int^{V_{geo}} U_p(\vec{r})[n(\vec{r})/n_0]^\ell d^3r, \tag{3.39}$$

in analogy with definition (3.26). For a thermal distribution not truncated in momentum space $\gamma_{\ell e}(T) = \gamma_{1e}(T/\ell)/\ell$. The quantity γ_{2e} is a practical quantity when discussing heating of the sample due to particle loss associated with binary atomic collisions.

3.2.6 Sample-averaged collision rates

Consider a volume V filled homogeneously with a single-component gas of N particles in thermal equilibrium. In the usual approach (see, e.g., Ref. [4]) the ℓ-body collision event rate Γ_ℓ in the gas is written in terms of an ℓ-body rate constant G_ℓ:

$$\Gamma_\ell = \frac{1}{\ell!} n^\ell G_\ell V, \tag{3.40}$$

where $n = N/V$ is the particle density. In general G_ℓ depends on externally applied fields and thus in an inhomogeneous system on position, so we may write

$$\Gamma_\ell = \frac{1}{\ell!} \int d^3r\, G_\ell(\vec{r}) n^\ell(\vec{r}) = \frac{1}{\ell!} n_0^\ell G_{\ell e} V_{\ell e}, \tag{3.41}$$

where the system-averaged rate constant $G_{\ell e} \equiv V_{\ell e}^{-1} \int d^3r\, G(\vec{r})[n(\vec{r})/n_0]^\ell$, n_0 is a reference density, and $V_{\ell e}$, the ℓ^{th} order effective volume, is defined in Eq. (3.26).

In experiments with trapped H↑ densities are always so low that only binary collisions have to be considered. Therefore we will omit the subscript denoting the number of particles involved in a collision from now on. For two-body collisions the rate constant $G = \langle v_r \sigma \rangle$, where the brackets $\langle\rangle$ denote averaging over a thermal velocity distribution. Here v_r is the relative velocity of the colliding pair and σ is the effective cross section, i.e. the total cross section for a collision between two particles with relative velocity $\vec{v}_r$ averaged over all directions of $\vec{v}_r$ [6]. The effective cross section σ, which may apply to both elastic and inelastic collisions, contains all necessary information about a single collision event, including particle-indistinguishability effects.

In the definition of the two-body rate constant G thermal equilibrium is implicitly assumed, so in the case of a pumped distribution the above averaging procedure is not applicable. For any thermal distribution we may write

$$\Gamma = \frac{1}{2m} \int d^3r \int d^3p_1 \int d^3p_2\, |\vec{p}_2 - \vec{p}_1| \sigma f(\vec{r}, \vec{p}_1) f(\vec{r}, \vec{p}_2), \tag{3.42}$$

where $f(\vec{r}, \vec{p})$ is the thermal distribution function (3.7) and the integration is over the available phase space. In general σ depends both on $|\vec{p}_2 - \vec{p}_1|$ and on $\vec{r}$. For a pumped distribution the integration is over all $(\vec{r}, \vec{p})$ for which $U_p(\vec{r}) + p_{1,2}^2/2m \leq \epsilon_{tr}$. Since the momentum space integrations depend on $\vec{r}$, the evaluation of Γ generally involves a complicated nested integral which is different for each choice of the trapping potential U_p.

Fortunately, in the case of atomic hydrogen the relevant rate constants can often be approximated by very simple forms. As we will discuss in more detail in Sect. 3.3, the elastic scattering cross section is to a good approximation independent of the external field and the relative velocity of the colliding atoms, which simplifies the calculation of the elastic collision event rate considerably. For inelastic collision processes, i.e. collisions in which untrapped high-field seeking states are produced (Sect. 3.4), σ is inversely proportional to the relative velocity at very low collision energies. In this case $G = \langle v_r \sigma \rangle = v_r \sigma$ is independent of temperature and the calculation of the total event rate for inelastic collisions only involves an integration over $\vec{r}$ space:

$$\Gamma = \frac{1}{2} \int d^3r \, G(\vec{r}) n_p(\vec{r})^2 = \frac{1}{2} n_0^2 G_e V_{2e}^p, \tag{3.43}$$

where n_p is the pumped density distribution (3.10).

3.3 Loading of the trap and thermalization

As far as neutral atom trapping is concerned, H$\uparrow$ is unique because it can be captured in a magnetostatic trap without the use of a resonant radiation source. This is due to the fact that spin-polarized atomic hydrogen is the only gas that can be manipulated and cooled using material surfaces at temperatures comparable to the well depth of magnetic traps ($\epsilon_{tr}/k_B \lesssim 1$ K). This can be accomplished by covering all surfaces with a layer of superfluid helium. In the loading process the confining cryogenic surfaces serve two purposes: First, they cool the H gas to temperatures low enough for trapping. Second, collisions between the atoms are necessary to scatter them into trapped states and the surfaces surrounding the trapping region are essential for building up the relatively high densities required for efficient filling through collisions. The densities of trapped particles that can be achieved in this way are so high that the trapped atoms undergo many collisions with each other during their trapped lifetime. As a result the trapped sample reaches a state of internal (quasi) equilibrium shortly after loading.

3.3.1 Interaction with helium surfaces

The interaction of H atoms with a surface of liquid helium at sub-Kelvin temperatures has some remarkable properties [4]. When an H atom impinges on a ℓ-He surface it is either adsorbed on the surface or reflected. When the atom is adsorbed it floats on top of the surface and does not dissolve into the liquid. The interaction is extremely weak: The adsorption potential for H on ℓ-^{4}He supports only one bound state with a binding energy $\epsilon_a/k_B = 1.011(10)$ K [7]. The shallow adsorption potential is essential for spin-polarized hydrogen research as it allows a gas of H atoms to exist in thermal equilibrium with the walls of its container at temperatures below 1 K. In the experiments described in this thesis all inner surfaces of the experimental cell were covered with a (saturated) superfluid film of ^{4}He with a thickness of ~ 100 Å.

At sub-Kelvin temperatures the thermal wavelength of the H atoms, $\lambda_{th}\sqrt{T} = 17.5\,\text{Å}\text{K}^{1/2}$, is longer than the range of the He surface adsorption potential (< 10 Å). As the wavelength λ_{th} of the H atoms colliding with the surface increases with decreasing T, the overlap of the incoming plane wave with a surface bound state becomes smaller, giving rise to the phenomenon of quantum reflection: The probability that an H atom impinging on the ℓ-He surface is adsorbed, the so-called sticking probability s, decreases with decreasing temperature. If the atom is not adsorbed it is reflected specularly. Berkhout *et al.* measured the sticking probability in the temperature range $0.07\,\text{K} \leq T \leq 0.5\,\text{K}$: $s/T \approx 0.33\,\text{K}^{-1}$ [8, 9]. For the experiments described in this thesis $s \lesssim 0.07$, so the helium covered surfaces act as highly reflective mirrors.

An H atom adsorbed on the He surface comes off again after some time τ_a through a thermally activated desorption process. Using a simple argument this residency time τ_a can be estimated [4] from

$$\tau_a = \frac{h}{sk_BT_w}\exp(\epsilon_a/k_BT_w), \tag{3.44}$$

where T_w is the wall temperature. We find for $T_w = 0.2\,\text{K}$ $\tau_a \approx 0.5\,\mu\text{s}$ and for $T_w = 0.07\,\text{K}$ $\tau_a \approx 50\,\text{ms}$. Clearly the residency time has a very strong temperature dependence in the relevant temperature range. As a consequence the loading process is very sensitive to the temperature of the cell walls.

3.3.2 Elastic H-H collisions

Elastic collisions between H atoms play a crucial role in our experiments. The cross section for elastic scattering between H atoms is well known. For elastic collisions between d state atoms the $T = 0$ s-wave scattering cross section is given by $\sigma_{el} = 8\pi a_T^2$, where $a_T = 0.72$ Å is the triplet scattering length, calculated using the well-known H-H interaction potential [12, 13]. At finite temperatures there are in principle contributions due to higher order partial waves and the energy dependence of the collisional phase shifts. For the collisional energies encountered in our experiments, however, these corrections are always small and can be safely neglected. In this thesis we therefore always use the $T = 0$ elastic scattering cross section $\sigma_{el} = 13\,\text{Å}^2$. The $T = 0$ cross section for elastic collisions between c and d state atoms is also independent of B, but twice as small due to distinguishability of the particles. The $T = 0$ cross section for elastic collisions between c state atoms, however, is B-dependent and is given by

$$\sigma_{el}^{cc} = 8\pi[a_T^2 + \frac{1}{16}\sin^4 2\theta\,(a_T - a_S)^2 - \frac{1}{2}\sin^2 2\theta\, a_T(a_T - a_S)], \tag{3.45}$$

where θ is the hyperfine mixing angle (Eq. (3.5)) and $a_S = 0.17\,\text{Å}$ is the singlet scattering length. For $B \gg 0.05\,\text{T}$ ($\theta \to 0$) the $c - c$ cross section becomes equal to $\sigma_{el} = 8\pi a_T^2$. For $B \geq 0.1\,\text{T}$ we find that $\sigma_{el}^{cc} \geq 0.9\sigma_{el}$, so for our experiments we may approximate σ_{el}^{cc} by the field independent value $8\pi a_T^2$.

3.3.3 Loading process

Hydrogen atoms are produced in all four hyperfine states by dissociation of H_2 in a low-temperature ($T \approx 0.6\,\text{K}$) rf discharge in high field (Chapter 4). The low-field seeking H↑ atoms are pulled through a narrow tube towards the trapping region while the H↓ atoms stay behind in the high-field region. While travelling through the narrow tube the "hot" H↑ gas exchanges heat through inelastic collisions with the helium covered inner surface of the tube and is cooled to the wall temperature T_w of the trapping region.

The passage of the gas through the tube connecting the dissociator to the trapping region is the most critical phase in the loading process. The surface coverage depends exponentially on T_w (see Eq. (3.44)), so if T_w is too low the H atoms will recombine through two-body surface recombination [4] on the inside of the transport tube before they reach the trapping region. For a ℓ-^{4}He coverage it is experimentally found that there is a critical minimum wall temperature $T_w \approx 0.15\,\text{K}$ for efficient filling [2]. The above sketched picture is confirmed by the fact that when the surfaces are covered with a ^{3}He-^{4}He mixture, in which case $\epsilon_a/k_B \approx 0.4\,\text{K}$ [10], the critical wall temperature for filling is much lower.

When the H↑ gas enters the trapping region it is of course not immediately trapped. An additional mechanism is required to scatter particles which move close to the trap minimum into trapped orbits. In the case of H↑ we rely entirely on elastic collisions between the atoms.

The H↑ gas is sprayed out of the filling tube into the trapping region, a long cylindrical volume ($\sim 20\,\text{cm}^3$) enclosed by ℓ-^{4}He covered walls (see Fig. 3.2). Typically a flux of a few times 10^{12} atoms per second can be produced, so within a second an average density of the order of $10^{11}\,\text{cm}^{-3}$ can be built up. An atom will rattle around between the walls until it collides near the trap center and loses enough kinetic energy in the event to be trapped.

Due to the elongated shape of the potential well the radial oscillatory motion is much faster than the axial motion so every atom collides with the walls approximately twice every radial oscillation period $\tau_r \approx 0.4\,\mathrm{ms}$. The diameter of the cylindrical trapping region $d = 12\,\mathrm{mm}$. Assuming an average density $n = 10^{11}\,\mathrm{cm}^{-3}$ and a mean free path $(n\sigma_{el})^{-1} \approx 80\,\mathrm{m}$ we can estimate the time τ_c in which every atom has collided on average once:

$$\tau_c \sim \frac{\tau_r}{2nd\sigma_{el}} \approx 1\,\mathrm{s}. \tag{3.46}$$

We expect that H↑ atoms are scattered into trapped states within a time of the order of $\tau_c \approx 1\,\mathrm{s}$. Once a small number of atoms is trapped, the central density increases and the process is accelerated. Eventually the gas will settle into a thermal density distribution. This filling procedure is only possible due to the presence of confining walls, which allow the build-up of density in the trapping region.

During the loading heat is carried off to the surrounding walls. Heat exchange with the walls happens on a time scale τ_w, which is the average time between two sticking wall collisions: $\tau_w \sim \tau_r/2s$. For $T = 0.2\,\mathrm{K}$ the sticking probability $s \approx 0.07$, so $\tau_w \approx 3\,\mathrm{ms} \ll \tau_c$, and we expect the excess heat to be carried off immediately during the thermalization process. Once the gas settles into a trapped distribution, the wall contact is reduced. For a thermal distribution the fraction of particles colliding with the walls is given by the evaporation fraction f_{ev} given by Eq. (3.25), so the time constant for heat exchange then is $\tau_w \sim \tau_r/2sf_{ev}$. For $T = 0.2\,\mathrm{K}$ $f_{ev} \approx 30\%$ and $\tau_w \sim 0.01\,\mathrm{s}$, which is still much smaller than τ_c. Clearly, if no other heating or cooling processes are involved, the trapped gas will thermalize directly to the wall temperature T_w at these densities.

Using the equilibrium description developed in the previous section we can estimate the amount of heat carried off during the trapping process. Before any particle is scattered into a trapped state, the energy with respect to the trap minimum of a cloud of N atoms sprayed into the trapping region is $E_i = N(\epsilon_{tr} + (3/2)k_BT_w)$. After the gas has settled into a thermal density distribution, truncated by the reflective walls, its internal energy is $E_f = (\gamma_{1e}(T_w) + 3/2)Nk_BT_w$. Therefore, the energy absorbed by the surrounding walls equals $E_i - E_f = N(\epsilon_{tr} - \gamma_{1e}(T_w)k_BT_w) \approx 10^{-11}\,\mathrm{J}$ for $N = 10^{12}$ and $T_w = 0.2\,\mathrm{K}$ (see Sect. 3.2.5).

3.3.4 Thermalization time

For our description of the trapped gas we rely heavily on the fact that the gas is in a state of internal (quasi) equilibrium. All kinds of processes are possible which disturb the equilibrium state of the sample (evaporation, collisional relaxation, optical pumping, etc.). For our equilibrium assumption to be valid it is essential that the timescale of collisional internal equilibration is much shorter than any timescale associated with disruption of the equilibrium state.

We assume that the elastic collision event rate per atom Γ_c/N is a good measure for the internal equilibration rate: Every particle in the sample will have collided In a time $\tau_c = (2\Gamma_c/N)^{-1}$ on average once with another particle. For a thermal distribution of a pure d state gas (see 3.2.6)

$$\Gamma_c = \frac{\sigma_{el}}{2m} \int d^3r \int d^3p_1 \int d^3p_2 \, |\vec{p}_2 - \vec{p}_1| f(\vec{r}, \vec{p}_1) f(\vec{r}, \vec{p}_2). \tag{3.47}$$

As usual, we introduce center-of-mass and relative momentum coordinates $\vec{P} \equiv (\vec{p}_1 + \vec{p}_2)/2$ and $\vec{q} \equiv \vec{p}_2 - \vec{p}_1$. Using $d^3p_1 \, d^3p_2 = d^3P \, d^3q$ and the definition (3.7) of f, we get:

$$\Gamma_c = \frac{\sigma_{el} n_0^2 (2\pi m k_B T)^{-3}}{2m} \int d^3r \, e^{-2U_p(\vec{r})/k_BT} \int d^3P \, e^{-P^2/mk_BT} \int d^3q \, q e^{-q^2/4mk_BT}. \tag{3.48}$$

In the case of a pumped distribution, i.e., the integration over phase space restricted to $U_p + p_{1,2}^2/2m \leq \epsilon_{tr}$, the $\vec{P}$ and $\vec{q}$ integration boundaries depend on each other which makes the calculation of Γ_c slightly tricky. We will come back to this in detail in Chapter 7 where a similar calculation is required for the evaporation rate. For now we will calculate Γ_c for a distribution truncated in configuration space, as is the case, for instance, for a trapped sample in thermal equilibrium with the cell walls. The $\vec{P}$ and $\vec{q}$ integrations can then be carried out straightforwardly and we find:

$$\Gamma_c = \frac{1}{\sqrt{2}} n_0^2 \bar{v} \sigma_{el} V_{1e}^t(T/2), \tag{3.49}$$

where $\bar{v} = \sqrt{8k_BT/\pi m}$ is the average thermal velocity and V_{1e}^t the first order effective volume (see 3.2.4). The collision frequency per atom is

$$\tau_c^{-1} = \sqrt{2} n_0 \bar{v} \sigma_{el} \frac{V_{1e}^t(T/2)}{V_{1e}^t(T)}. \tag{3.50}$$

For a typical central density $n_0 = 5 \times 10^{11}\,\mathrm{cm}^{-3}$ and a temperature $T = 0.2\,\mathrm{K}$ we find $\tau_c = 0.8\,\mathrm{s}$ for the "long" geometry. As can be seen in Fig. 3.5, γ_{1e} does not depend strongly on T. For constant $\gamma_{1e} = \gamma$ one can easily derive that $V_{1e} \sim T^\gamma$. Thus in our case the collision frequency for $T \leq 0.2\,\mathrm{K}$ can be approximated to within $\sim 25\%$ by

$$\tau_c^{-1} \approx 2^{-\gamma+1/2} n_0 \bar{v} \sigma_{el}, \tag{3.51}$$

where $1.5 \leq \gamma \leq 2$. Note that τ_c^{-1} is independent of the Ioffe trap parameters α and β in this approximation. For $k_BT \ll \mu_B B_0$, i.e. for a harmonic trap, $\gamma_{1e} = \gamma = 1.5$ and Eq. (3.51) holds exactly.

Although in the case of a pumped distribution the calculation of τ_c is somewhat more complicated, it is given to a good approximation by Eq. (3.50) for $\eta = \epsilon_{tr}/k_B T \geq 8$.

3.4 Particle loss mechanisms

As can be seen at first glance from the Zeeman diagram (Fig. 3.1), a gas of magnetostatically trapped H$\uparrow$ is not in its lowest energy state. The population of only the H$\uparrow$ states is a non-equilibrium situation and the spins will ultimately relax to non-trapped H$\downarrow$ states. The most fundamental spin-flip process is relaxation through binary interatomic collisions. We will show, however, that these do not play any role of importance in the experiments in this thesis. Other spin-flip mechanisms are possible (collisions with trapped electrons, Majorana transitions, optical pumping, and impurity relaxation on the wall), but can be avoided. If the helium film is locally removed from the wall surface, particles may also leave the trap without having their spins flipped if they have aquired enough kinetic energy to reach the bare surface. Thermal escape of H$\uparrow$ atoms then leads to evaporative cooling of the sample. This loss mechanism will be treated in detail in Chapter 7. The H$\uparrow$ atoms may also escape after collisions with highly energetic particles of a spurious, "hot", background gas. The latter mechanism is thought to be determining the lifetime of the trapped gas in the experiments described in this thesis (a lifetime of typically a few minutes).

3.4.1 Collisional relaxation

The collisional properties of H atoms are very well known. In fact, due to its simple structure, H is the only system for which interparticle collisions can be treated exactly from first principles. The scattering of two H atoms is actually a four-particle problem, containing the mutual interactions of two electrons and two protons [6]. Since the final reaction products are again H atoms (for recombination to the molecular state a third body is required), the H-H collision can be described effectively by a spin-dependent interatomic potential, which has been calculated from first principles by Kolos and Wolniewicz [13].

By far the most dominant scattering mechanism is due to the Coulomb interaction, which gives rise to the singlet and triplet interatomic potentials. Ignoring for the moment the nuclear spin, H atoms in the electronic groundstate interact through the singlet potential curve if $S = 0$ and through the triplet potential curve if $S = 1$, where $\vec{S} = \vec{s}_1 + \vec{s}_2$ is the total electron spin (see Fig. 3.6). In a gas of

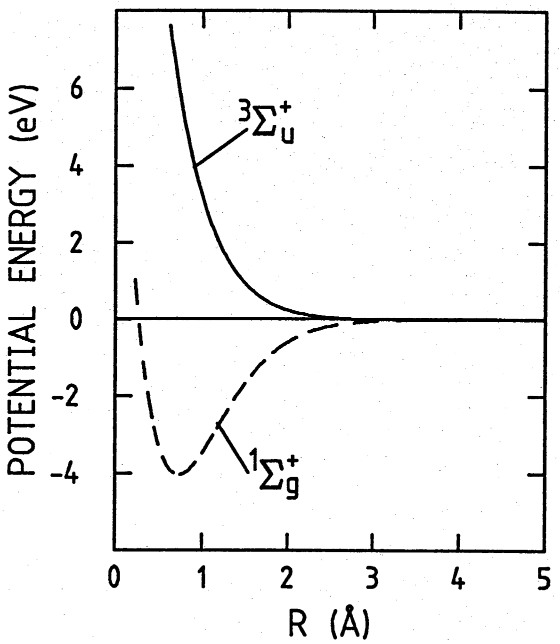

Figure 3.6: The singlet (dashed) and triplet interatomic potentials of hydrogen.

spin-polarized hydrogen (H↑ or H↓) the atoms interact through the mainly repulsive triplet potential. The elastic scattering cross section of H↑ atoms, which we used in the previous section, was calculated using the singlet/triplet potential curves.

Since the Coulomb interaction only depends on the interatomic distance, orbital angular momentum is conserved during collisions and thus the total spin. Consequently, for the description of inelastic (spin-flip) collisions other contributions to the interatomic interaction have to be included.

At large interatomic distances the spin eigenstates of H atoms in a magnetic field are the hyperfine states a, b, c, and d, as given in Eq. (3.4). Since the a and c states are superpositions of electron spin-up ($m_s = 1/2, \uparrow$) and electron spin-down ($m_s = -1/2, \downarrow$) states, the two-particle spin states $|h_1 h_2\rangle$ ($h_1, h_2 = a, b, c, d$) are in general superpositions of singlet ($S = 0$) and triplet ($S = 1$) states or, in other words, the asymptotic two-particle spin states $|h_1 h_2\rangle$ are in general not eigenstates of the singlet/triplet interaction. As a result H atoms can be scattered in collisions from one hyperfine state to the other. This spin-flip mechanism is called spin-exchange relaxation. For an H↑ gas, consisting of c and d state atoms, mainly collisions between c state atoms lead to spin-exchange relaxation. For $c-d$ collisions spin-exchange relaxation only proceeds via odd partial waves, which have a negligible contribution at low temperatures. Spin-exchange can be a very efficient mechanism, leading to a rapid depletion of the *c* state population of the trapped gas. Since the *d* state is a pure electron spin-up state, the remaining *d* state gas is stable against spin-exchange relaxation. The collisional decay of a *d* state sample is much slower as it is mainly induced by the relatively weak dipole-dipole interaction between the magnetic moments of the electrons. In principle several other processes contribute in a H-H collision event. It turns out, however, that it is sufficient for an accurate description of inelastic collisions to take into account only the spin-exchange and electron-electron dipolar interactions [6].

The collision event rate constants for inelastic H-H collisions have been calculated by Lagendijk *et al.* and Stoof *et al.* [14, 15]. Van Roijen *et al.* have measured the collisional decay of a sample of trapped *d* state atoms and found it to be in agreement with theoretical predictions for dipolar decay [1, 2].

We will now estimate the relaxation lifetimes for both spin-exchange and dipolar decay under conditions typical for the experiments in this thesis. As was already mentioned in Sect. 3.2.6, both the spin-exchange and the dipolar event rate constants go to a constant value if $T \to 0$. We will approximate the inelastic event rate constants by their $T = 0$ values, which is good enough for a rough estimate. For a pure *d* state sample the dipolar collision event rate is given by (see 3.2.6)

$$\Gamma_{dip} = \frac{1}{2} n_0^2 G_e^{dip} V_{2e}, \tag{3.52}$$

where G_e^{dip} is the sample-averaged event rate constant for dipolar relaxation. Eq. (3.52) holds for both distributions considered. In the dominant process ($d + d \to a + a$) two high-field seekers are produced per event, so the dipolar decay rate $\tau_{dip}^{-1} \equiv \dot{N}/N \approx 2\Gamma_{dip}/N$ becomes

$$\tau_{dip}^{-1} \approx n_0 G_e^{dip} V_{2e}/V_{1e}. \tag{3.53}$$

Approximating the field averaged rate constant by its value G_0 at the trap minimum ($B_0 = 0.1\,\mathrm{T}$) we have $G_e^{dip} \approx G_0 = 2 \times 10^{-15}\,\mathrm{cm}^3/\mathrm{s}$. Using a typical central density $n_0 = 5 \times 10^{11}\,\mathrm{cm}^{-3}$ and $T = 0.2\,\mathrm{K}$ we find $\tau_{dip} \approx 2 \times 10^3\,\mathrm{s}$. If the event rate constant is correctly averaged over the inhomogeneous trapping field τ_{dip} can be up to $\sim 2\times$ smaller [1, 2]. Similarly, we may approximate the field averaged spin-exchange rate constant by its value at the trap minimum, $G_e^{ex} \approx 10^{-13}\,\mathrm{cm}^3/\mathrm{s}$. For a pure *c* state sample under the same conditions we then find for the spin-exchange relaxation lifetime $\tau_{ex} \approx 40\,\mathrm{s}$. Since the electron spin-down admixture of the *c* state decreases with increasing magnetic field, the spin-exchange rate decreases as well, so after correct field averaging a somewhat larger value for τ_{ex} is obtained. Taking

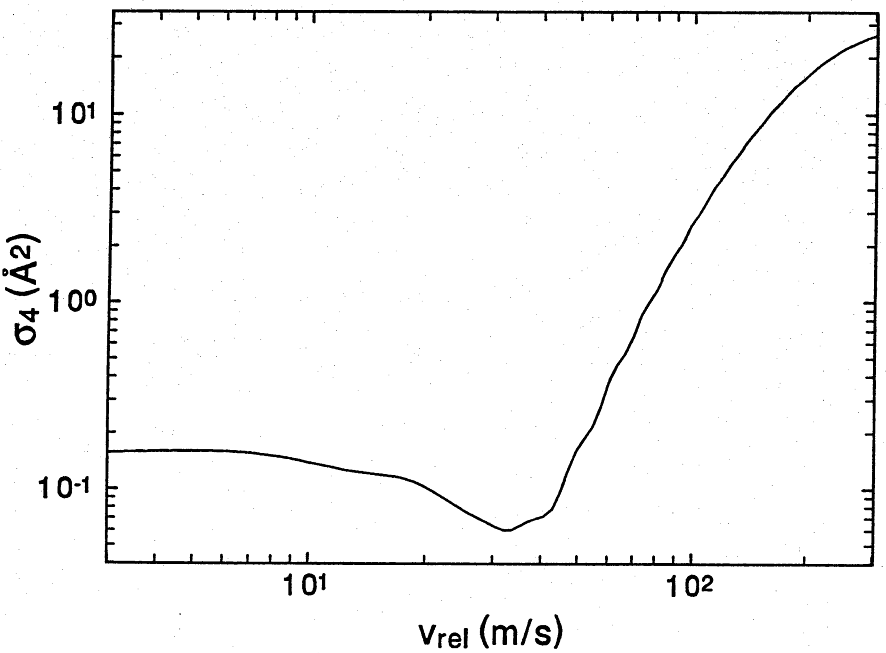

Figure 3.7: ^{4}He-H elastic scattering cross section as a function of the relative velocity.

into account that in practice the c density is smaller than $n_0/2$, the spin-exchange lifetime in our experiments is always at least a few minutes.

For the experiments described in this thesis collisional relaxation of the trapped gas is negligible.

3.4.2 ^{4}He background gas

In experiments with trapped alkali atoms the presence of a "hot" background gas is often the lifetime determining factor. Due to the necessarily sub-Kelvin cell wall temperatures helium is the only gas which may give rise to such problems in H$\uparrow$ experiments.

The scattering cross section for ^{4}He-H collisions can be calculated using the so-called R2 potential [16, 19]. Recent measurements of the diffusion of H in ^{4}He gas at sub-Kelvin temperatures [17] show good agreement with calculations based on the R2 potential. In Fig. 3.7 the ^{4}He-H elastic scattering cross section σ_4 is plotted as a function of the relative velocity v_{rel}. The $T = 0$ cross section is very small, about 1% of the $T = 0$ H-H elastic cross section. Due to the negative sign of the scattering length, $a_4^{\ell=0} = -0.108$ Å, the s-wave phase shift goes through zero, giving rise to a minimum in σ_4 at $v_{rel} \approx 30\,\mathrm{m/s}$. At higher relative velocities contributions due to higher order partial waves become appreciable and σ_4 increases rapidly.

We can estimate the effect for a homogeneous cell wall temperature T_w. For $T_w = 0.2\,\mathrm{K}$ the ^{4}He vapor density $n_4 \approx 10^4\,\mathrm{cm}^{-3}$. If we take for the ^{4}He-H scattering cross section a worst case value $\sigma_4 = 10\,\mathrm{\AA}^2$ and approximate the relative speed by the ^{4}He average thermal velocity, we find that an H atom collides with a ^{4}He atom once every $\tau_4 \sim 10^7\,\mathrm{s}$. Clearly, this is a completely negligible effect in the usual H$\uparrow$ trapping experiments. At slightly higher temperatures, however, this effect can already become significant, as the ^{4}He vapor density is a very steep function of temperature in this temperature region: $n_4 \sim \exp(-L_4/k_B T)$, where L_4 is the latent heat per atom, $L_4/k_B = 7.1688\,\mathrm{K}$ [18].

In the experiments described in this thesis there was a substantial temperature gradient over the length of the cell due to a spurious radiative heat load (Chapter 4). The hottest part of the cell was the entrance window (4 mm diameter) at a temperature of $\sim 0.5\,\mathrm{K}$, situated at a distance of $\sim 20\,\mathrm{cm}$ from the H$\uparrow$ sample (see Fig. 4.2). The particle flux Φ coming off a liquid ^{4}He surface with a temperature T_w and a surface area A is given by [20]

$$\Phi = \frac{A}{4\pi^2}\frac{m_4}{\hbar^3}k_B^2 T_w^2 e^{-L_4/k_B T_w}, \tag{3.54}$$

where m_4 is the atomic mass of ^{4}He. In view of the strong temperature dependence it is clear that only the effect of the hottest part of the cell has to be considered. Furthermore, since ^{4}He atoms colliding with a liquid ^{4}He surface are absorbed with a probability close to unity, only ^{4}He atoms flying off the hot window surface in a small solid angle subtended by the sample can reach the trapped H$\uparrow$ (see Chapter 4). Assuming the H$\uparrow$ velocities are negligible with respect to the ^{4}He velocities and using the value $\sigma_4 = 5\,\mathrm{\AA}^2$ for the cross section, we may estimate the ^{4}He-H collision rate per H$\uparrow$ atom:

$$\tau_4^{-1} = \frac{\Phi}{\pi}\frac{\sigma_4}{L^2}, \tag{3.55}$$

where L is the distance from the surface to the H$\uparrow$ sample. For a surface with a temperature $T = 0.5\,\mathrm{K}$ and a diameter of 4 mm at a distance $L = 20\,\mathrm{cm}$ we find $\tau_4 = 50\,\mathrm{s}$. Since we do not know the exact temperature and surface area of the "hot spot" we cannot make any precise statements, but the effect is clearly of the same order of magnitude as the observed lifetime of a few minutes. In addition, elimination of the radiative heat load recently resulted in much longer lifetimes, probably only limited by collisional relaxation [21].

Only those ^{4}He atoms which come off the window surface with enough energy to kick H$\uparrow$ atoms directly over the $\epsilon_{tr}/k_B = 0.8\,\mathrm{K}$ evaporation barrier contribute to particle loss. The rest of the ^{4}He kinetic energy deposited in the sample is distributed through elastic H-H collisions and leads to uniform heating of the gas, as will be discussed in Sect. 3.5.

3.4.3 Other loss mechanisms

If the magnetic field experienced by the trapped particles changes too rapidly, transitions between different hyperfine states are induced, as was already discussed in Sect. 3.1. These so-called Majorana transitions are induced, for instance, in zero-field regions at very low temperatures [3], which is clearly of no concern to us. Atoms moving in a surface-adsorbed state along the cell wall may also experience a wildly fluctuating field due to ferromagnetic impurities in the substrate [22]. For a trapped H↑ sample in contact with the surrounding walls this can lead to very efficient $d \rightarrow c$ relaxation on the wall. Subsequently this results in particle loss either by two-body recombination on the wall surface or, after desorption, by spin-exchange relaxation of the bulk gas. We have observed that the lifetime of a sample in contact with the wall at $T \approx 0.2\,\mathrm{K}$ is considerably shorter than the lifetime at lower gas temperatures ($T < 0.1\,\mathrm{K}$), when the wall contact becomes negligible (Chapter 7). The difference in lifetime is attributed to a wall-induced decay mechanism.

Probing the sample with Lyman-α introduces some extra loss processes. Obviously atoms are expelled from the trap due to optical pumping to non-trapped H↓ states. This effect can be quite significant in our case since the number of photons absorbed per second can be of the same order as the number of trapped particles. We will come back to this in Chapter 6. Another possible loss process associated with the Lyman-α probe is due to photo emission of electrons. The photoelectric yield at the Lyman-α wavelength is $\sim 3\%$ for copper [23], so per second up to $\sim 10^6$ electrons with an energy of a few eV may be ejected from the cell wall. These electrons may get trapped and lead to decay of the H↑ sample through e-H collisions.

3.5 Heating and cooling

The same processes that give rise to particle loss in general also lead to a change of temperature. Consider a number of processes causing both particle loss $\dot{N} = \sum_i \dot{N}_i$ and change of the total energy $\dot{E} = \sum_i \dot{E}_i$. For a sample in a state of (quasi) equilibrium the internal energy E may be written as (see 3.2.5)

$$E = Nk_BT(\gamma_{1e} + 3/2), \tag{3.56}$$

so we can easily derive

$$\dot{T} = \frac{\sum_i \dot{E}_i - \sum_i \dot{N}_i k_B T(\gamma_{1e} + 3/2)}{N k_B(\gamma_{1e} + T\partial\gamma_{1e}/\partial T + 3/2)}. \tag{3.57}$$

This is the basic equation for calculating temperature changes of the trapped gas. For temperatures $T \ll \epsilon_{tr}/k_B$ we have $T\partial\gamma_{1e}/\partial T \ll \gamma_{1e}$ and the heat capacity $Nk_B(\gamma_{1e} + T\partial\gamma_{1e}/\partial T + 3/2) \approx 3Nk_BT$. However, for a pumped distribution at temperatures $k_BT \gtrsim \epsilon_{tr}/8$ one should be more careful since the heat capacity can be strongly reduced due to the truncation of the distribution. For instance, for a pumped distribution in our trap at $T = 0.2\,\mathrm{K}$ the heat capacity is less than $(3/2)Nk_B$. This has important consequences for the onset of the evaporative cooling process, which will be described in detail in Chapter 7.

Eq. (3.57) can be written in the form $\dot{T} = \sum_i \dot{T}_i$, where $\dot{T}_i$ is the rate of temperature change due to the i^{th} process. In general, the different processes give rise to different rates of heating and only the dominant ones have to be taken into account. In our experiments the temperature evolution during the limited lifetime of the sample was determined mainly by evaporative cooling and probably to a lesser extent by heating due to the ^{4}He background gas. We will now discuss some heating processes and the associated timescales.

3.5.1 Intrinsic collisional heating

Collisions between H$\uparrow$ atoms are most frequent in high density regions, so particle loss due to inelastic collisions takes place preferentially at the center of the trap. This results in an increase of the average energy of the remaining atoms and thus in heating of the sample. Heating of the trapped gas due to collisional relaxation is fundamentally unavoidable. Ultimately, the lowest temperatures that can be reached in trapped H$\uparrow$ gas will be limited by dipolar heating. However, we will make a simple estimate showing that the influence of collisional heating in the experiments described in this thesis is negligible, due to the limited lifetime of the gas.

Consider an inelastic collision process, characterized by a rate constant G^{inel}, in which both colliding H$\uparrow$ atoms are scattered into non-trapped H$\downarrow$ states. Due to this process energy is extracted from the gas at a rate

$$\dot{E}_{inel} = \int G^{inel}(\vec{r})[U_p(\vec{r}) + (3/2)k_BT]n^2(\vec{r})\,d^3r. \tag{3.58}$$

Approximating $G^{inel}(\vec{r})$ by its value G_0 at the center of the trap (like in Sect. 3.4.1), we have

$$\dot{E}_{inel} \approx G_0 n_0^2 V_{2e}(\gamma_{2e} + 3/2)k_BT \approx \dot{N}_{inel}(\gamma_{2e} + 3/2)k_BT, \tag{3.59}$$

where $\dot{N}_{inel}$ is the particle loss rate due to inelastic collisions. Using Eq. (3.57) we arrive at the following equation for the heating due to collisional relaxation:

$$\frac{\dot{T}_{inel}}{T} \approx \frac{\gamma_{2e} - \gamma_{1e}}{\gamma_{1e} + T\partial\gamma_{1e}/\partial T + 3/2} \frac{\dot{N}_{inel}}{N}. \tag{3.60}$$

For a thermal distribution $\gamma_{2e}(T) = (1/2)\gamma_{1e}(T/2)$. If $T \ll \epsilon_{tr}/k_B$ we may aproximate $\gamma_{1e} \approx 1.5$, so $\dot{T}_{inel}/T \approx (1/4)\dot{N}_{inel}/N$. Apparently, the heating rate associated with collisional relaxation events in which both atoms are turned into high-field seekers, is comparable to the collisional relaxation rate itself. This is true in general, so this heating process is completely negligible in our experiments.

Collisional relaxation events in which only one of the colliding atoms is lost from the trap (e.g., $d{+}d \rightarrow a{+}d$) give rise to so-called recoil heating. Due to conservation of momentum, half of the energy gained in the exothermic reaction is dumped in kinetic energy of the atom that remains trapped. At temperatures relevant to this work these processes give rise to a similar heating behavior as described above.

3.5.2 Wall heating

As was shown in Sect. 3.3, inelastic wall collisions determine the temperature of the gas during the loading process. Once the gas has settled into a trapped thermal distribution, the influence of the walls is suppressed. We estimated crudely also for this case the time constant τ_w of heat exchange with the walls:

$$\tau_w \sim \tau_r/2f_{ev}s, \tag{3.61}$$

with τ_r the radial oscillation period and $s/T \approx 0.33\,\mathrm{K}^{-1}$ the sticking probability. In a more accurate approach, the event rate of wall collisions of a trapped sample in thermal equilibrium is given by

$$\Gamma_w = \frac{1}{4} n_w \bar{v} A_w, \tag{3.62}$$

where $n_w = n_0 \exp(-\epsilon_{tr}/k_B T)$ is the density at the wall, $\bar{v}$ the average thermal velocity, and $A_w \approx 40\,\mathrm{cm}^2$ the wall surface area. From Eq. (3.62) immediately follows

$$\tau_w^{-1} = \frac{s\Gamma_w}{N} = \frac{s}{4}\frac{A_w}{V_{1e}^t}\bar{v}e^{-\epsilon_{tr}/k_B T}, \tag{3.63}$$

where V_{1e}^t is the effective volume as given by Eq. (3.28). For $T = 0.2\,\mathrm{K}$ we find $\tau_w \approx 0.02\,\mathrm{s}$ and for $T = 0.1\,\mathrm{K}$ $\tau_w = 0.7\,\mathrm{s}$. For $T = 0.05\,\mathrm{K}$ $\tau_w \approx 10^3\,\mathrm{s}$ and the gas can be considered completely isolated from the walls. Although based on a completely different picture, the crude estimate (3.61) agrees for $0.05\,\mathrm{K} < T < 0.25\,\mathrm{K}$ within a factor ~ 3 with the more accurate expression (3.63).

Implicitly we have assumed that the collisional internal equilibration rate τ_c^{-1} is much larger than τ_w^{-1}. However, this is only the case for relatively low temperatures and high densities. For instance, for typical conditions $T = 0.1\,\mathrm{K}$ and $n_0 = 5 \times 10^{11}\,\mathrm{cm}^{-3}$, we find $\tau_c \approx 1\,\mathrm{s}$. Clearly a very efficient cooling mechanism, like evaporative cooling, is required to cool the gas below the wall temperature.

3.5.3 ^{4}He background gas

As was already mentioned in the previous section, the energetic ^{4}He atoms evaporating from hot spots on the cell wall in principle give rise to both particle loss and heating. The exact temperature of the ^{4}He source is not known, so it is not possible to make any precise quantitative statements about this heating process, but we can make a rough estimate of an upper bound.

Assuming the H$\uparrow$ atoms have negligible velocities, on average a fraction $\frac{8}{25}$ of the ^{4}He kinetic energy is transferred to the H atom per ^{4}He-H elastic collision event. The average kinetic energy of the ^{4}He atoms is $2k_BT_w$, with T_w the wall temperature [20]. Assuming that all ^{4}He-H collisions lead to heating of the gas and not to direct particle loss, we find with the help of Eq. (3.57) for the heating rate:

$$\dot{T}_4 \approx \frac{16}{75} T_w \tau_4^{-1}. \tag{3.64}$$

For example, for $T_w = 0.5\,\mathrm{K}$ and $\tau_4 = 50\,\mathrm{s}$ (Eq. (3.55)) we find $\dot{T}_4 \approx 10^{-3}\,\mathrm{Ks}^{-1}$. Assuming τ_4^{-1} is a realistic value for the H-He collision rate, this is clearly an overestimate for the heating rate, since the ^{4}He atoms with a kinetic energy greater than $(25/8)\epsilon_{tr}/k_B \approx 2.5\,\mathrm{K}$ will lead to direct particle loss and not to heating. In addition, the scattering cross section increases with collision energy (Fig. 3.7), which means that energetic collisions in which H$\uparrow$ atoms are kicked out of the trap are favored.

References

[1] R. van Roijen, J. J. Berkhout, S. Jaakkola, and J. T. M. Walraven, Phys. Rev. Lett. **61**, 931 (1988).

[2] R. van Roijen, Ph. D. thesis, University of Amsterdam (1989).

[3] T. H. Bergeman, P. McNicholl, J. Kycia, H. Metcalf, and N. L. Balazs, J. Opt. Soc. Am. B **6**, 2249 (1989).

[4] I. F. Silvera and J. T. M. Walraven, in *Progress in Low Temperature Physics*, D. F. Brewer, ed. (North Holland, Amsterdam, 1986), Vol. **X**, p. 139 (1986).

[5] J. M. Doyle, Ph. D. thesis, Massachusetts Institute of Technology (1991).

[6] J. van den Eijnde, Ph. D. Thesis, Technical University of Eindhoven (1984).

[7] W. N. Hardy, M. D. Hürlimann, and R. W. Cline, Jap. J. Appl. Phys. **26**, Suppl. 26-3, 2065 (1987).

[8] J. J. Berkhout, E. J. Wolters, R. van Roijen, and J. T. M. Walraven, Phys. Rev. Lett. **57**, 2387 (1986).

[9] J. J. Berkhout, O. J. Luiten, I. D. Setija, T. W. Hijmans, T. Mizusaki, and J. T. M. Walraven, Phys. Rev. Lett. **63**, 1689 (1989).

[10] G. H. van Yperen, A. P. M. Matthey, J. T. M. Walraven, and I. F. Silvera, Phys. Rev. Lett. **47**, 800 (1981).

[11] I. F. Silvera and J. T. M. Walraven, Phys. Rev. Lett. **45**, 1268 (1980).

[12] D. G. Friend, and R. D. Etters, J. Low Temp. Phys. **39**, 409 (1980).

[13] W. Kolos and L. Wolniewicz, Chem. Phys. Lett. **24**, 457 (1974); W. Kolos and L. Wolniewicz, J. Mol. Spectrosc. **54**, 303 (1975).

[14] A. Lagendijk, I. F. Silvera, and B. J. Verhaar, Phys. Rev. B **33**, 626 (1986).

[15] H. T. C. Stoof, J. M. V. A. Koelman, and B. J. Verhaar, Phys. Rev. B **38**, 4688 (1988).

[16] R. Jochemsen, A. J. Berlinsky, and W. N. Hardy, Can. J. Phys. **62**, 751 (1984).

[17] T. Arai, A. Matsubara, S. Hotta, J. S. Korhonen, N. Masuhara, T. Suzuki, A. Masaike, T. Mizusaki, and A. Hirai, Internal report Kyoto University (1993); Proceedings of the 20th International Conference on Low Temperature Physics, Eugene, U.S.A. (1993).

[18] W. N. Hardy and M. Morrow, J. Phys. (Paris), **42**, C8-171 (1981).

[19] M. W. Reynolds, private communication.

[20] A. F. G. Wyatt, Phys. Rev. Lett. **69**, 1785 (1992).

[21] I. D. Setija, H. G. C. Werij, O. J. Luiten, M. W. Reynolds, T. W. Hijmans, and J. T. M. Walraven, Phys. Rev. Lett. **70**, 2257 (1993).

[22] A. J. Berlinsky, W. N. Hardy, and B. W. Statt, Phys. Rev. B **35**, 4831 (1987).

[23] J. A. R. Samson, *Techniques of Vacuum Ultraviolet Spectroscopy* (John Wiley and Sons, 1967).

[24] K. Helmerson, A. Martin, and D. E. Pritchard, J. Opt. Soc. Am. B **9**, 483 (1992).

Chapter 4

Cryogenic apparatus

In contrast to other trapable particles (neutrons, alkali atoms, electrons, ions) a cryogenic environment is an essential requirement for trapping of H$\uparrow$. The available magnetostatic traps have a well depth of the order of one Kelvin, so H atoms have to be precooled to sub-Kelvin temperatures in order to be trapped. Since radiation sources capable of stopping an atomic beam, such as used for the trapping of alkalis, are not (yet) available for H, it is necessary to use the cryogenic techniques originally developed for experiments with H$\downarrow$ gas. The H$\uparrow$ gas is manipulated and precooled by interaction with surfaces covered with a layer of superfluid helium. For trapping experiments the temperature of the surfaces should be preferably below $\sim 0.3\,\mathrm{K}$, since at higher temperatures the He vapor density starts limiting the lifetime of the trapped gas. Consequently, the experiments are carried out in a ^{3}He-^{4}He dilution refrigerator.

4.1 Overview

An overview of the cryogenic apparatus is shown in Fig. 4.1. We use a commercial dilution regrigerator (Oxford Instruments), which has been modified to enable optical access from below, along the symmetry axis. The dilution unit has a maximum cooling capacity of $250\,\mu$W at a mixing chamber temperature of 100 mK and a maximum circulation rate of $500\,\mu$mole/sec.

The can, which houses the trapping magnet, is situated inside a 4 K radiation shield and is suspended from the main ^{4}He bath. During operation the magnet can is filled with liquid ^{4}He at a temperature of 4.2 K. The trapping magnet assembly inside the magnet can consists of three dipole coils, a set of quadrupole coils, and the dissociator solenoid (see Chapter 2). Together they generate a magnetic field with a minimum on the symmetry axis, at a height determined by the four currents sent

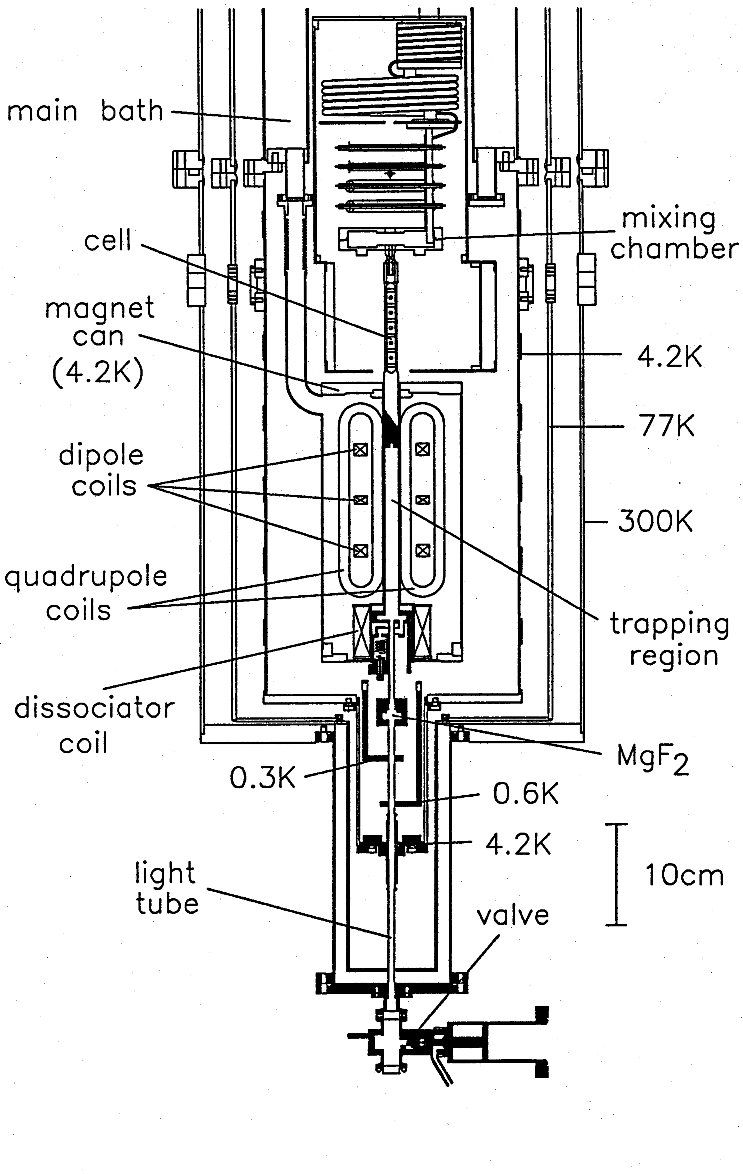

Figure 4.1: Cryogenic apparatus. Indicated are some of the main components and temperatures of various parts.

through the three dipole coils and the dissociator coil. In the field configurations considered in this thesis the position of the minimum is always approximately at the center of the middle (Majorana) dipole coil. The calculation of the trapping field is extensively treated in Chapter 2, including all experimental details relevant to the calculation: The locations, orientations, and dimensions of the coils, their numbers of windings, and their maximum allowable currents. A detailed description of the construction of the magnet can and the trapping magnet assembly is given in Ref. [1].

The construction of the experimental cell is in principle straightforward: In view of the compact construction of the trapping magnet and the presence of the dilution unit above, optical access to the $H\uparrow$ gas trapped in the field minimum is most easily accomplished from below, along the symmetry axis. Therefore, the main body of the experimental cell is a tube-like structure, suspended from the mixing chamber, hanging freely in the bore of the magnet can. A cryogenic MgF_2 window at the lower end of the cell allows light to enter the cell while keeping the superfluid helium film confined to the inner surface. Technical complications arise as a cryogenic dissociator, thermally isolated from the main cell body, a filling tube with an intermediate thermal accommodation stage, and a trigger bolometer have to be installed in the high field region of the dissociator coil (free accessible bore 40 mm), without blocking the light path. Moreover, light detectors have to be installed inside the limited space of the trapping region (free accessible bore 16 mm) without sacrificing too much of the effective trapping depth: the attainable trapping depth is proportional to the radial distance of the material surface closest to the symmetry axis. Any object sticking out from the side wall will reduce the trapping depth. We have been able to mount four fluorescence detectors on the cylindrical side wall of the trapping region and a transmission detector and a trigger bolometer in the top part of the trapping region, while keeping a clear radial aperture 12 mm across, corresponding to a maximum well depth of $\Delta B = 1.3\,\mathrm{T}$.

The experimental cell extends from the mixing chamber to the holder for the MgF_2 entrance window over a total length of approximately 46 cm. Optical access from room temperature is provided by a thin-walled light tube between the cell entrance window and the room temperature vacuum jacket. The optical access and the various parts of the experimental cell are discussed in more detail in the following.

4.2 Optical access

The use of Lyman-α radiation imposes some severe restrictions on the way the light is guided into the cryostat.

In the first place, the best available optical materials typically transmit per component only ~ 50% at the Lyman-α wavelength (121.6 nm), so as few optical components as possible should be used. In our setup the entrance window to the cell is the only optical component inside the cryostat. In principle even this single window could be dispensed with by making use of a film burner construction or by lining the optical entrance to the cell with cesium, which inhibits superfluid film flow [2]. In the case of a film burner one should take care that the fluxing helium vapor cannot reach the trapping region.

In the second place, Lyman-α radiation is very strongly absorbed in N_2, H_2O, all organic solvents, vacuum greases, pumping oils, etc., so it is essential that the light path is kept free from these kinds of contaminance. This is true in particular in a cryogenic environment where the optical components act as very efficient sorption pumps. For this reason the light in our setup is guided to the experimental cell through a tube, isolating the light path from the contaminated cryostat vacuum spaces. The light tube contains only metal parts and was cleaned meticulously. Furthermore, in the room temperature vacuum space, which is in open connection with the light tube vacuum and which contains various vacuum optical components, only all-metal vacuum seals were used, strongly out-gassing materials were avoided as much as possible, and all components were cleaned very thoroughly. These precautions turned out to be sufficient to avoid the build-up of cryo-deposits coming from room temperature. During the initial cool-down the transmission of the MgF_2 entrance window decreased, which was probably due to contaminations inside the experimental cell, condensing on the window. However, during the subsequent run of three months, in which the MgF_2 window was kept continuously at sub-Kelvin temperatures, the Lyman-α transmission showed no sign of further deterioration.

The construction of the light tube is such that it provides a clean light path, while simultaneously keeping the different parts of the cryostat thermally isolated. It consists of two parts: A stainless steel tube (6 mm outer diameter and 0.2 mm wall thickness) connects the room temperature vacuum jacket to the 4 K vacuum jacket and radiation shield. Halfway, the stainless steel tube is thermally anchored to liquid nitrogen temperature by means of a copper rod and braid (not shown in Fig. 4.1) connected to the 77 K shield. The copper rod is soft-soldered to the stainless steel tube. In the light tube a diaphragm with a 3 mm dia. aperture is situated at the height of the 4 K shield. A CuNi tube, 6 mm o.d. and 0.2 mm wall thickness, connects the 4 K shield to the cell entrance window. To minimize the conductive heat load on the experimental cell, the CuNi tube, coming from 4 K, is pinned to the still (typical temperature 0.6 K) and the cold plate (typically at 0.3 K) of the dilution umit. (The cold plate is the thermal stage between the continuous heat exchanger and the discrete heat exchangers.) The pinning is realized by copper rods, soldered with Woods metal to the CuNi tube, and copper braids (not shown in Fig. 4.1).

With all the precautions mentioned, the conductive heat load through the light tube is reduced to the negligible level of $< 1\,\mu$W. However, the optical access unavoidably introduces a heat load due to thermal radiation as well. This effect was underestimated at first and it led to substantial heating of the cell in the first run. The room temperature radiation reaching the MgF_2 window directly, without reflections, or via reflections on the stainless steel surface, is entering in such a small solid angle that it causes negligible heating ($\leq 1\,\mu$W). However, the inner surface of the CuNi tube, although oxidized, turns out to be a fairly good reflector of room temperature radiation. As a result the window flange heated up to a temperature of $\sim 0.45\,$K. The mixing chamber could not be cooled below 0.15 K. On the basis of the temperature of the mixing chamber and the ^{3}He circulation rate we estimate that the radiative heat load was approximately $300\,\mu$W, which means that at least 10% of the radiation entering the CuNi tube was absorbed in the cell. In a follow-up experiment [3] radiation baffles were inserted in both parts of the light tube, eliminating the problem completely.

4.3 Experimental cell

In Fig. 4.2 a more detailed drawing of the experimental cell is shown, together with a plot of the trapping field. The experimental cell is suspended from the mixing chamber and is almost entirely made out of copper to ensure good thermal conductivity. It consists of three main parts, which will be described separately in more detail. The upper part which contains the actual trapping region and extends from $z = -113$ mm upwards to the mixing chamber. The lower part, which consists of, amongst others, the dissociator and the window flange is located inside and below the dissociator coil. The detection unit, which is a cylindrical device, shaped like an apple corer, is slid inside the upper part of the cell and contains the transmission photodiode, the bolometric fluorescence detectors, and the "evaporation pump". The upper part and the lower part of the cell are connected by an indium seal.

4.3.1 Upper part

The upper part of the cell is a plain copper tube, outer diameter 15 mm and inner diameter 13 mm, soft soldered to a solid copper rod. The copper tube is hanging freely in the 16 mm bore of the magnet can and surrounds the H$\uparrow$ trapping region.

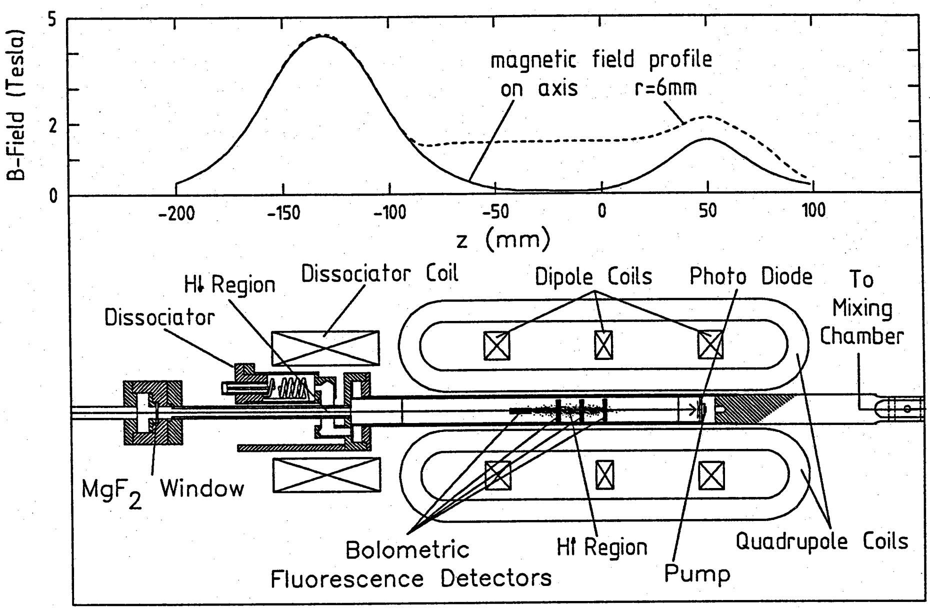

Figure 4.2: Lower part: Experimental cell and coils. Upper part: Trapping field which is generated if only the dissociator coil, the upper dipole coil, and the quadrupole coils are energized with their maximum allowable currents.

The top end of the solid rod is connected to the mixing chamber by an 8 mm screwed joint, tightened with the maximum allowable torque of ~ 3 Nm to ensure good thermal conductivity [4].

The solid rod is made of high purity copper [5], with a low temperature thermal conductivity $\kappa T^{-1} = 54\,\mathrm{WK^{-2}m^{-1}}$. To improve the thermal conductivity of the tube, which is made of plain copper, it was annealed during ~ 10 hr in a ~ 10^{-4} mbar O_2 environment at ~ 1000 K [6, 7], which resulted in a low temperature thermal conductivity $\kappa T^{-1} = 270\,\mathrm{WK^{-2}m^{-1}}$. The values for the thermal conductivity were inferred from measurements of the ratio of the room temperature electrical resistivity of the copper to that at 4.2 K [4].

Owing to the high thermal conductivities of the tube and the solid rod the cell walls surrounding the trapping region could be kept at a temperature of ~ 0.2 K with a temperature gradient of less than 10%, in spite of an excessive heat load. The improvement of the thermal conductivity of, in particular, the copper tube with respect to earlier trapping experiments [1], was vital for the success of the first optical experiment.

The copper of the trapping volume and all other parts to which the H$\uparrow$ gas is exposed, were electrolytically etched to remove possible magnetic impurities implanted by machining. Such impurities may induce spurious hyperfine relaxation of H$\uparrow$ atoms to H$\downarrow$ when they are moving on or near the wall [8].

4.3.2 Lower part

The lower part of the cell is the service section, containing the MgF_2 entrance window, the cryogenic dissociator for producing H gas, a trigger bolometer for the removal of H$\downarrow$ atoms, and all electrical feedthroughs.

The MgF_2 window (10 mm o.d., 1 mm thick, 60% Lyman-α transmission at room temperature) is mounted in a brass window flange. The window is clamped with indium seals on both sides, with a clear aperture of 6 mm. The flange is connected by a copper tube (4 mm i.d., 6 mm o.d.) to the rest of the cell.

The cryogenic dissociator is a helical resonant cavity whose inner surfaces are covered with a layer of solid H_2 underneath the superfluid helium film. By striking a pulsed microwave discharge H atoms are produced, which subsequently find their way to the trapping region through a filling tube. The dissociator is similar in design and operation to the one described in some detail by Van Roijen [1]. The resonant frequency of the cavity at low temperatures is $f = 795\,\mathrm{MHz}$, with a quality factor $Q \approx 400$. The dissociator is thermally anchored to the still of the dilution unit at a typical temperature of 0.6 K.

The H gas produced in a discharge is transported to the main body of the cell through a thin-walled CuNi tube. The function of this filling tube is to isolate the dissociator thermally from the main body of the cell and to precool the H gas. The discharge produces large amounts of He vapor as well, which, if allowed to reach the main body of the cell, lead to heating of the cell and a spurious decay of the trapped sample. Therefore, halfway the filling tube there is an optically tight copper baffle, the so-called thermal platform (not shown in Fig. 4.2), to condense the fluxing He vapor. The first half of the filling tube is a 14 mm long CuNi tube, 6 mm o.d., with a wall thickness of 0.2 mm. The second half is a 11 mm long CuNi tube, 4 mm o.d., with a wall thickness of 0.2 mm. The thermal platform between the two tube sections is a small copper block with a hole running through. The thermal platform is pinned to the cold plate of the dilution unit at a temperature of, typically, 0.3 K. Its inner surface area is enlarged by means of a few mm^3 of silver sinter ("French powder") in order to accommodate the heat deposited by the condensing He effectively. The second half of the filling tube is connected to the main cell body in such a way that H atoms or He atoms entering the trapping region have to undergo at least a few wall collisions before they can reach the trapped sample.

In the present setup a flux of a few times 10^{12} H$\uparrow$ at/s can be produced easily. If the microwave pulse parameters (peak power, pulse duration, and repetition rate) and the number of pulses fed into the resonant cavity are kept constant the number of atoms which are loaded into the trap is reproducible within a few percent.

The cell contains two trigger bolometers which can be used to locally remove H atoms. A trigger bolometer is usually a small resistor, suspended by thin conductive wires. If the resistor is heated with an electrical current sufficiently to evaporate more He than can be replenished by superfluid film flow along the supporting wires, then the liquid He film will be removed from the resistor surface. Once the surface is bare, H atoms will be strongly adsorbed and recombine rapidly. One trigger bolometer is located in in the high field region, at the height of the center of the dissociator coil, approximately 12 mm off axis (not shown in Fig. 4.2). It is a small carbon chip ($\sim 1\,\mathrm{mm}^3$), cut out of a Speer resistor, suspended by two 50 μm thick superconducting wires (Niomax). Approximately 15 μW is required to burn off the He film and thus trigger recombination of H$\downarrow$ atoms caught in the high field region. To keep the heat load on the main body of the cell minimal, the copper housing of the trigger bolometer is thermally anchored to the cold plate of the dilution unit and connected to the main body of the cell by a thin-walled CuNi tube. The inner surface area of the copper housing is enlarged by means of a few mm^3 of silver sinter in order to carry off the heat efficiently. The second trigger bolometer (denoted as "pump" in Fig. 4.2), located in the top part of the trapping region, behind the photo diode, will be described below.

4.3.3 Detection unit

The detection unit is a thin-walled copper supporting structure, 166 mm long, 13 mm outer diameter, and 0.5 mm wall thickness. A length of 130 mm of the cylindrical wall has been removed over half the circumference, yielding the shape of an apple corer and enabling access to the inner surface. It fits tightly inside the copper tube which is suspended from the mixing chamber. The lower end of the "apple corer" is screwed to the lower part of the experimental cell.

At the upper end of the detection unit a GaAsP Schottky photodiode (Hamamatsu G1126) is mounted, facing the light beam. For a discussion of its detection characteristics, see Chapter 5, Sect. 5.5.1.

On the back of the photodiode a trigger bolometer is mounted. This bolometer is a graphite film resistor, suspended by two 16 μm thick tungsten wires. The resistive film is Aquadag, an aqueous dispersion of graphite particles [9], which is painted on a 2.5 mm × 2.5 mm Kapton foil, 50 μm thick. The tungsten wires are attached with silver epoxy to copper electrodes, which are vacuum evaporated on the foil. Approximately 4 μW is required to burn off the He film. When triggered, this bolometer efficiently pumps energetic H$\uparrow$ atoms, thus enabling evaporative cooling of the trapped sample. The photo diode acts as a shield, protecting the H$\uparrow$ sample against the He vapor fluxing off the trigger bolometer.

A 50 μm thick foil of Kapton is attached with Stycast 1266 epoxy to the inner surface of the detection unit. Four thin ($\sim$ 1 μm) Aquadag film resistors are painted on the Kapton surface, which act as bolometric light detectors at low temperatures. For a discussion of the use of these graphite film resistors as pulsed light detectors, see Chapter 5, Sect. 5.5.2. The leads of the film resistors and the wiring of the photodiode and the trigger bolometer are vacuum deposited on the Kapton surface. In this way the fluorescence detectors and the wiring in the trapping region protrude negligibly from the cell wall and a satisfactory trapping well depth can be attained.

The flat copper wiring on the Kapton foil inside the "apple corer" was made using a photo-lithographic technique. First a relatively thick layer of copper ($\sim$ 1 μm) is vacuum evaporated on a thoroughly cleaned Kapton foil. The copper bonds very well to the Kapton substrate and can be kept for at least several weeks in a normal atmosphere without showing any signs of deterioration. A photo-resistive layer is sprayed on the copper. Using a positive mask, part of the photo-resistive layer is exposed to UV light. After developing the photo-resistive layer, the Kapton foil is submersed for $\sim$ 10 s in a Fe_3Cl solution at $\sim$ 45° C to etch off the copper at the exposed sites. The resulting printed circuit is cleaned with water and acetone and the foil is glued to the inner surface of the "apple corer". Kapton foil with a 30 μm copper layer and a photo-resistive layer already present is commercially available. However, due to the thickness of the copper layer this foil is not flexible enough to be glued to the curved inner surface of the "apple corer" (radius of curvature 6 mm), and was therefore not suitable for our purposes.

The printed circuit on the Kapton is shown In Fig. 4.3. The foil is 127 mm long and 19 mm wide, corresponding to half the circumference of the inner surface of the detection unit. Copper wires are soldered to the four pads on the top (right) side copper wires to connect the photodiode and the trigger bolometer on top. The wires are soldered with Woods metal; if higher temperature solders are used, the copper layer may heat up too much, with the result that it comes off. From the twelve soldering pads on the bottom (left) side the circuit is connected to the vacuum feedthroughs in the lower part of the cell. The four pairs of thicker strips in the middle are the electrodes of the four Aquadag film resistors. For each the resistive area is 10 mm wide and 2 mm long. The resistor films are labeled 1, 2, 3, and 4 from

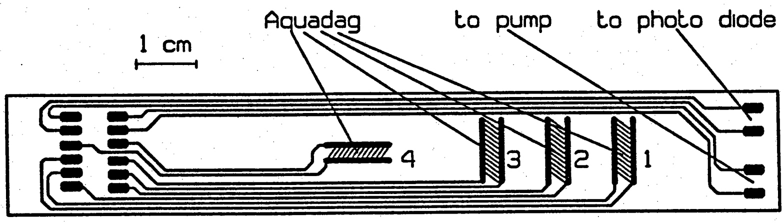

Figure 4.3: Printed circuit of the detection unit.

top to bottom (right to left in the figure) and the z-coordinates of the centers of the resistors are, respectively, $z_1 = 0$, $z_2 = -11\,\mathrm{mm}$, $z_3 = -21.5\,\mathrm{mm}$, and $z_4 = -43\,\mathrm{mm}$.

4.3.4 Thermometry

The temperatures of the various parts of the experimental cell are monitored using a $200\,\Omega$ Matsushita carbon resistor [10] and three RuO_2 thick film resistors (Philips, type RC-01) [11]. The resistances are measured using an AC method described in Ref. [12]. We calibrated the four resistors in a separate run against a ^{3}He melting curve thermometer [13].

Two of the resistors are attached to the main body of the experimental cell, one to the solid rod of the upper part of the cell and the other to the window flange at the low end of the cell. Further, one resistor is used to monitor the temperature of the dissociator, and one to measure the temperature of the thermal platform.

References

[1] R. van Roijen, Ph. D. thesis, University of Amsterdam (1989).

[2] P. J. Nacher and J. Dupont-Roc, Phys. Rev. Lett. **67**, 2966 (1991).

[3] I. D. Setija, H. G. C. Werij, O. J. Luiten, M. W. Reynolds, T. W. Hijmans, and J. T. M. Walraven, Phys. Rev. Lett. **70**, 2257 (1993).

[4] T. Sonnemans, "Eigen Werk 3", University of Amsterdam (1993, unpublished).

[5] Certified grade according to ASTM f68/77, manufactured by Outokumpu Oy (Finland).

[6] S. S. Rosenblum, W. A. Stoyert, and F. R. Fickett, Cryogenics **17**, 645 (1977).

[7] The annealing was done at the Kamerlingh Onnes Laboratory, University of Leiden, for which we thank R. Jochemsen and P. van de Haar.

[8] A. J. Berlinsky, W. N. Hardy, and B. W. Statt, Phys. Rev. B **35**, 4831 (1987).

[9] Acheson Colloids Co., U.S.A.

[10] S. Saito and T. Sato, Rev. Sci. Instrum. **46**, 1226 (1975).

[11] W. A. Bosch, F. Mathu, H. C. Meijer, and R. W. Willekers, Cryogenics **26**, 3 (1986).

[12] G. H. van Yperen, Ph. D. thesis, University of Amsterdam (1984).

[13] D. S. Greywall and P. A. Busch, J. Low Temp. Phys. **46**, 451 (1982).

Chapter 5

Optical Apparatus

5.1 Introduction

In general, optical techniques are both essential and very convenient tools in experiments with magnetically trapped atoms (see, for instance, Ref. [1]). The system of trapped atomic hydrogen stands out for two reasons. In the first place, H is the only atom that can be trapped without the use of optical techniques, as the H gas can be manipulated and cooled by liquid-helium covered surfaces. Secondly, the use of a resonant radiation source is rather cumbersome in the case of H due to the awkward Vacuum Ultra Violet (VUV) wavelength ($\lambda = 121.6\,\mathrm{nm}$) of the $1^2S \rightarrow 2^2P$ Lyman-α (L_α) transition, in particular when combined with the cryogenic requirements for trapping H. The main difficulty lies in the production of sufficiently intense narrow-band VUV radiation, which at present can only be generated using pulsed lasers and non-linear optical techniques. Furthermore, as L_α radiation does not propagate in air and, in particular, is very strongly absorbed in water, organic solvents, pump oils, vacuum greases, etc., one has to work under very clean vacuum conditions or in a very clean inert gas environment. The number of windows and lenses should be kept at a minimum because of strong absorption of L_α in all available materials (a 1 mm thick MgF_2 element typically has 50-65% transmission). Moreover, at cryogenic temperatures great care should be taken to avoid cryo-deposits on cold windows, which can quickly reduce the transmission to zero. For an overview of the requirements of VUV spectrocsopy, see Ref. [2]. In designing the optical system we were led by the following considerations: *i)* In order to perform accurate spectroscopy and to allow for the possibility of optical cooling, the bandwidth should preferably be close to the natural width of the relevant lines (100 MHz). *ii)* An intensity close to the saturation intensity of the transitions ($\sim 4\,\mathrm{W\,cm^{-2}}$) is desirable to facilitate optical cooling. *iii)* The measurement of both transmission and fluorescence should be possible. *iv)* The light source should be reproducibly tunable over the range of the H-spectrum. *v)* The system should exhibit a long-term reliability and relative ease of operation, since cryogenic measuring runs typically last several months. The system we describe in this chapter meets the above criteria, be it that the intensity of our L_α source is slightly less than desired (the intensity at the location of the sample amounts to about $0.25\,\mathrm{W\,cm^{-2}}$).

5.2 Generation of narrow-band Lyman-α

5.2.1 Experimental setup

Our light source is based on pulsed amplification of the light of a single-frequency cw ring dye laser (Coherent 699-21), operating at a wavelength of 729.6 nm. The amplified light is frequency-doubled in a KDP crystal and the L_α radiation is obtained by third-harmonic generation (THG) in a phase-matched mixture of Kr and Ar [3, 4, 5]. A XeCl excimer laser (Lambda Physik LPX 210i, 308 nm) is the pump source for pulsed amplification, as the relatively long pulses from this laser ensure the smallest possible bandwidth. It has the additional advantage of providing a relatively high pulse rate (100 Hz maximum). A similar, but Nd:YAG based scheme was used by Cabaret *et al.* [6] to study Stark shifts in an atomic H beam.

A schematic diagram of the setup is shown in Fig. 5.1. The dye laser is pumped by an Ar^+ laser (Coherent Innova 200). With cooling of the dye (pyridine 2) to 9 °C, the single-mode output of the dye laser (effective line width 1.5 MHz) amounts to ~ 750 mW at 6.5 W pump power. After passing an optical isolator the main part of the cw light is sent through a three-stage Rhodamine 700 pulsed dye amplifier (Lambda Physik 2003). After frequency-doubling, the ensuing Ultra Violet (UV) light (364.8 nm) is amplified once more in a DMQ dye cuvette. At a repetition rate of 50 Hz the energy of the amplified UV light is typically ~ 18 mJ/pulse. The bandwidth of the 365 nm light was determined using a confocal etalon of 150 MHz free spectral range (FSR) and found to be $40 - 60$ MHz, a factor 2-3 larger than that of a Fourier-limited Gaussian pulse of equivalent duration (20 ns). From this we obtain an estimate for the upper bound to the bandwidth of the L_α beam of 150 MHz.

To produce L_α, the UV light beam (typical beam radius 2 mm) is focused by an $f = 15$ cm lens into a mixture of, typically, 160 mbar Kr and 480 mbar Ar. Here Kr is the nonlinear medium for third-harmonic generation, whereas Ar is added for phase-matching purposes [7]. The typical power of the generated L_α radiation corresponds to $2 \times 10^9\,L_\alpha$ photons per 10 ns pulse (conversion efficiency $\sim 10^{-7}$). The power is

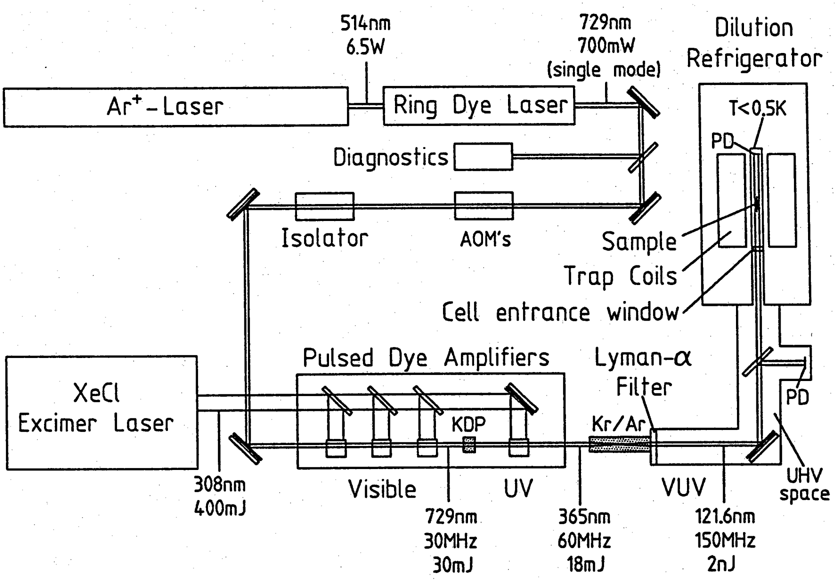

Figure 5.1: Schematic of the optical setup. Diagnostics stands for the reference cavities and the wavemeter, the photodiodes are denoted by PD.

limited by the occurrence of dielectric breakdown in the Kr/Ar mixture at too high an energy of the UV pulses. The frequency tripling is discussed in more detail in Sect. 5.2.2. After tripling the L_α radiation has to be separated from the, 10^7 times stronger, copropagating UV light. This is done by employing the refraction and dispersion of two MgF_2 lenses. Subsequently the L_α beam is sent into the cryostat from below, via a 45° mirror. A MgF_2 beam splitter between the mirror and the cryostat offers the possibility to perform ratio measurements, largely eliminating the noise due to the $\sim 10\%$ pulse-to-pulse fluctuations of the L_α intensity. With the beam splitter in place, about 2% (5×10^7 photons/pulse) of the L_α power produced in the tripling cell reaches the H sample. The monochromator and the VUV optics will be described in more detail in Sect. 5.2.3.

5.2.2 Tripling efficiency

Third harmonic generation (THG) of a lowest order Gaussian beam in an isotropic medium with negligible depletion of the fundamental beam, is described by [7]:

$$P_3 = \frac{3\pi^2}{\epsilon_0^2 c^2 \lambda_1^4} N^2 \mid \chi^{(3)} \mid^2 P_1^3 F, \tag{5.1}$$

where P_3 is the third harmonic power, P_1 the power of the fundamental beam, λ_1 the fundamental wavelength, $\chi^{(3)}$ the third-order susceptibility per atom for THG, N the particle density of the nonlinear medium, and F the dimensionless phase-matching function, which accounts for the interference between third harmonic light generated in different parts of the beam. When the dimensions of the beam focus are much smaller than the size of the tripling cell, F only depends on the confocal parameter b and the difference in refractive index $\Delta n = n(\lambda_1) - n(\lambda_1/3)$ of the medium. The generated third harmonic beam is also in the lowest order Gaussian mode with the same confocal parameter b and propagating in the same direction as the fundamental beam. Constructive interference of the generated third harmonic light, i.e., $F \neq 0$, is only possible if $\Delta n < 0$. The phase-matching function is then given by $F(x) = \pi^2 x^2 \exp(x)$, with $x = 6\pi b \Delta n / \lambda_1$. If the tripling cell only contains the nonlinear medium, x depends linearly on N and optimum THG can be achieved at a density $N = N_{opt}$ for which the quantity $N^2 F(x)$ maximal. For $N = N_{opt}$, $x = -4$, so $F_{opt} = F(-4) \approx 2.9$. By adding a positive dispersive linear medium ($\Delta n > 0$), $F(x)$ can be maximized independent of N, $F_{max} = F(-2) \approx 5.3$. The efficiency of THG is then in principle only limited by the maximum attainable particle density N of the nonlinear medium.

Due to the $4p^6(^1S_0) - 4p^5 5s(^3P_1)$ resonance transition at 123.58 nm, krypton gas has the required negative dispersion and also an appreciable third-order susceptibility, $\chi^{(3)} \approx 1.0(5) \times 10^{-50}\,\mathrm{V^{-2}m^5}$ [3, 4], at L_α (121.6 nm), making it very well suited for THG of L_α, as was first shown by Mahon *et al.* [3]. Argon gas, having a positive dispersion and a negligible $\chi^{(3)}$ at L_α, is added for phase-matching at high Kr densities. We use commercially supplied mixtures of predetermined Kr/Ar ratio for easy approximate phase-matching.

To analyze the performance of our tripling system we measured the L_α yield P_3 as a function of the 365 nm pump-beam power P_1 for various phase-matched gas mixtures, as shown in Fig. 5.2. The absolute L_α flux was measured with an ionization chamber filled with 8 torr of purified NO [2, 9], assuming 50% transmission for the $\mathrm{MgF_2}$ entrance window. The data obtained in 100 torr pure Kr show the desired cubic dependence of the third harmonic power on the fundamental power, except at the highest powers. The data obtained in Kr/Ar and Kr/$\mathrm{H_2}$ mixtures

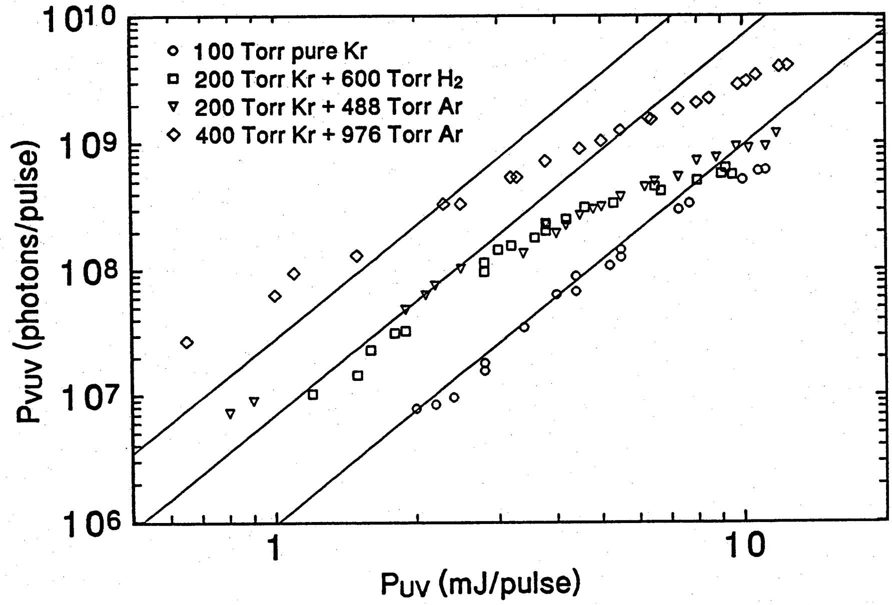

Figure 5.2: L_α yield versus 365 nm pump beam power for four different phase-matched gas mixtures. The solid lines are theoretically calculated curves (see text).

however, show strong deviations from this behaviour. The 200 torr Kr and the 400 torr Kr data sets exhibit approximately the expected quadratic dependence on Kr pressure. The two 200 torr Kr data sets, which were obtained using different positively dispersive phase-matching gases, show convincingly that the tripling efficiency depends on the Kr pressure only. The L_α yields calculated using Eq. (5.1), with $\chi^{(3)} = 0.9 \times 10^{-50}\,V^{-2}m^5$, are also shown in Fig. 5.2. The 100 torr pure Kr data show good agreement with theory, the 200 torr Kr data only at the lowest powers. The agreement with the 400 torr Kr data is less satisfactory. We believe that the deviations from theory at high pump powers are due to intensity-dependent changes of the refractive indices which break up the phase-matching [4, 10, 11]. This is a third order nonlinear process (Kerr effect) which was not taken into account in the theoretical description given above. The deviations are not due to linear absorption of L_α in Kr and Ar as was argued by Hilbig and Wallenstein [5]. In the first place, we observe roughly the correct Kr pressure dependence. Secondly, the extinction of L_α was measured by passing the L_α beam through a separate volume filled with Kr and Ar. We find values of $4(1) \times 10^{-6}$ (cm torr)$^{-1}$ and $6(1) \times 10^{-6}$ (cm torr)$^{-1}$ respectively for the extinction coefficients in Kr and Ar, consistent with the data of

Langer *et al.* [4]. These values are an order of magnitude too small to account for the observed reduction in yield at high gas pressure.

The maximum L_α yield is ultimately limited by dielectric breakdown in the Kr/Ar mixture at high UV powers. Such a discharge results in large fluctuations of the L_α intensity. Therefore, we adjust a diaphragm in front of the tripling cell to make the discharge just disappear. We also observed that the UV beam profile shows an increasingly severe higher-order mode structure for aging amplifier dyes, negatively affecting the conversion efficiency [8] and the threshold for dielectric breakdown. The tripling cell is indium-sealed and closed by an all-metal valve. No degrading of performance, associated with deteriorating gas purity, was observed during a period of three months.

We find a somewhat lower L_α yield than was reported by the authors of Ref. [5]. We attribute this to the lower breakdown intensity threshold I_{th} which is known to be associated with longer pump pulses: $I_{th} \sim p^{-1}\tau_p^{-0.7}$ [12, 13], where p is the pressure of the gas mixture and τ_p the pulse duration. Using Eq. (5.1), one can easily derive that when operating just below the threshold for dielectric breakdown, the number of third harmonic photons generated per pulse scales like $\sim b^2\tau_p^{-1.4}$. The combination of a shorter pulse ($\tau_p \approx 5$ ns versus $\tau_p \approx 10$ ns), a larger confocal parameter $b \approx 3$ mm (we typically have $b = 1.2$ mm), and approximately half of our UV pulse energy allowed the authors of Ref. [5] to go to much higher Kr gas pressures before dielectric breakdown occurs. In view of this analysis, a higher L_α yield may be achieved in our setup by increasing the confocal parameter b, thus moving the breakdown threshold to higher pump beam powers and higher gas pressures. This would require a longer tripling cell to prevent damaging the entrance and exit optics. Lowering the UV intensities by stretching the pulse length would have an adverse effect on the L_α yield.

The non-resonant tripling scheme with Kr was selected for its relative simplicity and reliability. Various resonant four-wave mixing schemes for generating VUV have been described in the literature which provide higher yields. A particularly efficient scheme suitable for L_α generation has been described by Marangos *et al.* [14]. However, these resonant schemes generally require two dye laser-amplifier chains, and are hence significantly more complex. An interesting new development is the generation of L_α using frequency doubling in atomic H gas, in which the inversion symmetry has been broken by a strong external static electric field [15]. Presently, the L_α intensities obtained using this method are comparable to the non-resonant scheme we use, but the method has potential for being more efficient.

5.2.3 VUV optics and UV-VUV separation

When working with L_α, only two materials are available with a non-zero transmission (Tr): LiF and MgF_2. LiF has a slightly higher transmission than MgF_2 but its transmission at L_α decreases when exposed to a normal laboratory atmosphere, as it deteriorates under the influence of moisture. For this reason we chose to use only MgF_2 optical components, most of which were supplied by Harshaw [16]. MgF_2 is birefringent, but in all our optical components the orientation of the optic axis is perpendicular to the surface, so there should be no retardation effects when the L_α beam propagates at right angles through the optics. Table 5.1 gives the refractive indices of MgF_2 at 19.5°C for the ordinary (n_o) and extraordinary (n_e) rays at some relevant wavelengths [17].

Table 5.1: The refractive indices n_o and n_e of MgF_2 for some relevant wavelengths.

	λ(nm)	n_o	n_e
"HeNe"	643.85	1.37682	1.38858
UV	365.01	1.38614	1.39834
VUV	121.53	1.6275	1.6320

After tripling, the L_α and the 10^7 times stronger, copropagating 365 nm UV light are separated in the monochromator, using the refraction and dispersion of two MgF_2 lenses. The first lens (L_1) [18], which is placed off-axis with respect to the incoming beam, focuses the L_α beam onto a 0.5 mm diameter aperture, while the fundamental beam is collimated and deflected via a mirror onto a beam dump (see Fig. 5.3). This technique of harmonic separation, which eliminates the additional

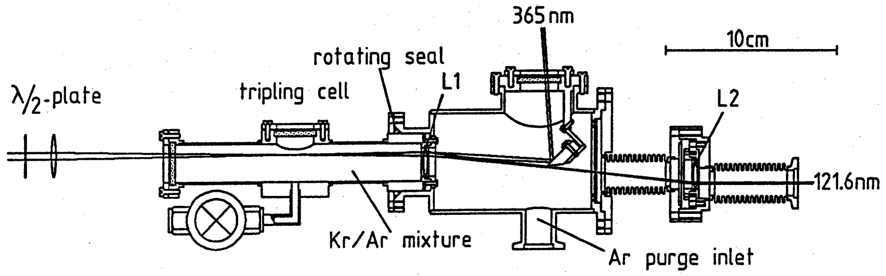

Figure 5.3: The tripling cell and monochromator.

absorption losses in a separate prism, was also used by VonDrasek *et al.* [20]. The off-axis beam path enables selection of an unspoiled part of the lens, by a simple rotation of the tripling cell with respect to the monochromator housing. This is convenient, as the transmission of L_1 decreases after several weeks of irradiation by the strong UV beam. A second MgF_2 lens (L_2) [19], which collimates the L_α beam, is also used off-axis to provide additional spectral filtering. The double filter arrangement reduces the intensity of the 365 nm radiation by more than 9 orders of magnitude. Lens L_2 is mounted in a bellows assembly to allow three-axial positioning for collimation and alignment purposes. The L_α beam is sent into the cryostat from below, via a 45° high quality (reflectivity $\sim 85\%$) VUV mirror [21], which is also mounted in a bellows assembly, allowing horizontal displacement in the direction of the incoming beam and small adjustments in both angular degrees of freedom of the reflecting plane. The H sample is located ~ 75 cm above the mirror. The combination of the VUV mirror and L_2 enables complete control of the L_α beam in the cryostat. A slight drawback of the off-axis use of the lenses is that it introduces astigmatism. Nevertheless, by adjusting the horizontal position of L_2, we were able to obtain a nearly circular beam cross section with a diameter of about 2 mm at the center of the trap, located 1.2 m from the tripling cell.

The volume between L_1 and L_2 is constantly being flushed with pure Ar at a pressure of about 20 torr. This is essential, since impurities sputtered by the UV beam will otherwise coat the lenses, making those impermeable for L_α radiation. The vacuum system behind L_2 is separated from the trapping volume by a 1 mm thick, indium sealed, MgF_2 window ($Tr \approx 60\%$), at sub-Kelvin temperatures. To avoid deposition of background gases onto this window we exclusively use all-metal seals, thus eliminating diffusive leaks due to the permeability of rubber O-rings. Furthermore, we minimize the gas load onto the cold window by closing a valve separating the cryostat from the room-temperature vacuum system, when not taking data. This allowed us to operate the system during a period of several months in which the MgF_2 window was kept at temperatures well below 1 K.

The L_α power can be measured in the room-temperature part of the setup by moving a VUV mirror into the beam on a UHV translation stage which directs the beam onto a solar blind vacuum diode (Hamamatsu R1187). A 1 mm thick retractable MgF_2 beam splitter ($Tr \approx 60\%$), mounted at 45° on a second translation stage, couples 5-10% of the beam into a second vacuum diode and thus enables ratio measurements.

Although the generated L_α light is linearly polarized [22, 23], we found that its polarization inside the H cell varied dramatically with small adjustments of the alignment. In spite of the fact that the beam does not travel at right angles through the lenses and the beam splitter, this cannot be due to retardation effects associated with the normal birefringence because in all four MgF_2 components both the VUV polarization and the optic axis lie in the horizontal plane of refraction. Instead we attribute the change in polarization to the dielectrically coated aluminum 45° VUV mirror [21]. By altering the orientation of the linear polarization of the incoming UV light using a half-wave plate, we can continuously change the L_α polarization in the sample cell from left-circular via linear to right-circular.

5.3 Frequency tuning

The frequency of the pulsed L_α radiation can be varied by tuning the cw dye laser frequency. This is perfectly suitable for relatively slow scans. In some cases, however, the possibility of pulse-to-pulse frequency switching is desirable to monitor the spectrum at specific discrete points during transient conditions when the spectrum changes rapidly. The latter method was used in our experiments to infer the temperature and density of the trapped H↑ gas during evaporative cooling. Furthermore, during optical cooling experiments it allows for occasional excursions to different parts of the spectrum, e.g., for thermometry, while the sample is irradiated at the optimal cooling frequency most of the time. To enable the fast switching, the cw dye laser light is guided through an arrangement of three acousto-optic modulators (AOM's), which is depicted schematically in Fig. 5.4. The alignment of the mirrors in Fig. 5.4 is such that, if either one of the three AOM's is switched on, the first-order diffracted beam enters the amplifier section along the same path, while there is no admixture of the zeroth-order undeflected light. With this AOM chain, the frequency of the cw beam is shifted either −80 MHz, +80 MHz or +150 MHz with respect to the incoming frequency. For the L_α light this corresponds to two

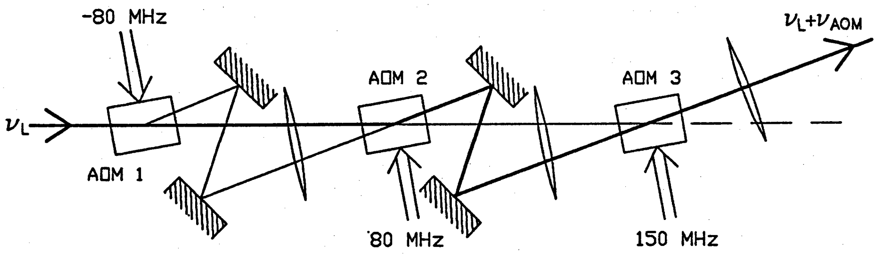

Figure 5.4: Layout of the AOM arrangement. For clarity, the angles have been exaggerated. The thick line denotes the light path when AOM 2 (+80 MHz) is switched on.

incremental steps of 0.96 GHz and 0.42 GHz respectively. The requirement for the alignment of the diffracted beams is rather stringent, since the distances from the AOM chain to the pulsed dye amplifiers and the H$\uparrow$ sample in the cryostat are 7 m and 15 m, respectively. To avoid drifting of the beam alignment due to rf heating, the AOM's are driven only during a 0.3 ms pulse, synchronized with the firing of the excimer laser. Once the three beams are made to overlap while using this method of pulsed AOM driving, the alignment procedure generally does not have to be repeated during several days.

We have repeatedly checked whether the polarization of the generated L_α light was dependent on the particular AOM used. When scanning across the H spectrum, while simultaneously switching rapidly between the three AOM's, we always found that, apart from the desired frequency shift, all three spectra were identical.

5.4 Frequency stability

In order to determine the L_α frequency to within one natural line width (100 MHz), the cw dye laser frequency should be known to within $\sim$ 20 MHz. For this purpose part of the cw 729.6 nm light is sent to a wavemeter and two temperature-stabilized reference cavities. The resolution of the commercial wavemeter (Burleigh WA-20) is insufficient (0.3 GHz). The accuracy of the frequency measurement is improved by using a piezo-driven confocal Fabry-Perot etalon, scanning $\sim$ 6 GHz at a repetition rate of 10 Hz. The FSR of the etalon is 3.0 GHz and its measured finesse is 175. This implies that the resolution is indeed better than the required 20 MHz. Since the uncertainty of the wavemeter reading is smaller than the FSR of the etalon, there is no ambiguity as to which order of the etalon is observed. Hence, after an initial calibration, we are able to obtain the cw laser frequency from a measurement of the applied piezo voltage. To remove errors arising from the inherent drift of the piezo material, even at constant temperature and pressure, we use a second etalon, without piezo material, which has the same FSR and resolution. This etalon serves as a standard for calibration of the piezo-driven etalon.

In order to obtain a good stability the design of both etalons was made as simple as possible, minimizing long term settling effects. The body of the etalons was made of an invar metal with a thermal expansion coefficient $\alpha \approx 1 \times 10^{-6}\,\mathrm{K}^{-1}$. The choice of the piezo material (Quartz & Silice, P7-62) was motivated by its small α ($\sim 2 \times 10^{-6}\,\mathrm{K}^{-1}$) and low power dissipation. Using a cylindrical piezo of length 9 mm and wall thickness 1 mm the piezo-driven etalon is measured to scan $\sim$ 18 MHz/V. The linearity of the piezo has been measured using the transmission peaks of a 150 MHz FSR etalon as frequency markers. Over a scanning range of

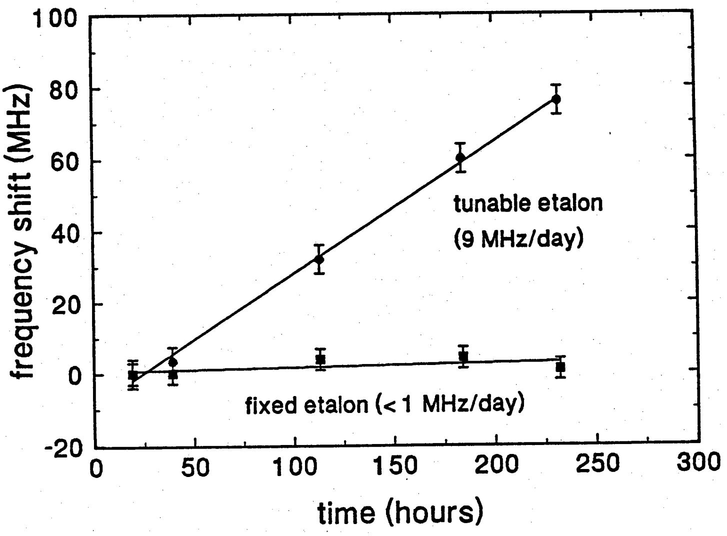

Figure 5.5: Frequency drifts of the reference cavities versus time, measured against a Doppler-free atomic line of potassium.

6 GHz the deviation from linearity was less than the accuracy of the measurement (~ 5 MHz).

Based upon the thermal expansion coefficients mentioned above we calculate a frequency shift of the order of 1 MHz/mK for both etalons. Therefore, the etalons are mounted in an extremely stable thermostat, developed for critical point experiments by Michels and Van Lieshout in our laboratory [25]. The short-term stability of this thermostat is better than 20 μK/h. In order to determine the long-term stability of the thermostat-etalon combination we monitored the drift of the etalon transmission peaks with respect to an atomic transition frequency. For that purpose we use the $4^2S_{1/2} \rightarrow 6^2S_{1/2}$ two-photon transition in potassium [26], which has a wavelength of 728.6 nm. When using counterpropagating laser beams we obtain a Doppler-free spectrum by observing the $6^2S_{1/2} \rightarrow 4^2P_{1/2,3/2}$ cascade fluorescence. In Fig. 5.5 we show the result of this measurement. Over a period of 10 days the tunable etalon showed a constant drift of 365 kHz/h, while the fixed etalon remained stable within 5 MHz.

5.5 Cryogenic VUV detection

Due to the construction of the trapping magnet in the cryostat we have only very limited optical access to the H↑ sample, along the symmetry axis of the cryostat. The bottom entrance was reserved for the L_α beam, and a detector on the top of the cryostat, apart from requiring major changes to the cryostat, would have a very small detection angle. Therefore, we decided to install the VUV transmission detector in the experimental cell. For the measurement of the scattered light intensity there was no other option but *in situ* detection. This puts some severe constraints on the detectors that can be used: *i)* The detectors have to operate reliably in magnetic fields up to ~ 1.5 T at temperatures as low as ~ 0.1 K. *ii)* The transmission detector has to fit inside the 12 mm diameter experimental cell and the fluorescence detectors have to be mounted on the cylindrical cell wall, sticking out as little as possible, as an object protruding from the cell wall by as little as 0.5 mm will already reduce the effective trapping depth by about 10%.

5.5.1 Transmission measurement

The optical transmission of the trapped H↑ gas is measured with a GaAsP Schottky photodiode (Hamamatsu G1126) mounted at the end of the cell. With the protective window removed, this diode is found to have a quantum efficiency (QE) of 14% for L_α from room temperature to well below liquid nitrogen temperature. An important property of this type of diode is that it has a good long-term reproducibility under VUV-irradiation [27]. At liquid helium temperature or below the properties are different, the QE dropping to about 10% at the specified maximum bias voltage of 5 V. At low temperatures the characteristics of the detector are not affected by magnetic fields up to 1.5 T.

The semiconductor device probably no longer operates as a diode at sub-Kelvin temperatures. We believe that the VUV detection properties are then the result of photoemission of electrons from the GaAsP substrate or from the gold layer on top. The QE is somewhat higher than the photoelectric yield of a room temperature Au photocathode at 120 nm [28]. We observed that the L_α sensitivity drops abruptly by approximately a factor of two when helium is admitted to the experimental cell, indicating partial blocking of the electron emission by the ~ 100 Å layer of superfluid helium. Furthermore, if the L_α beam was slightly misaligned a comparable signal with the opposite sign was obtained, probably due to photoemission from the photodiode housing, which is connected to the diode ground. The main advantage of using the diode instead of a (solar blind) metal photocathode lies in the sensitivity to both UV and HeNe-laser light at room temperature. This allows for 365 nm background checks and facilitates the rather delicate alignment of the optics (the clearance of the light beam inside the cryostat is restricted to 3 mm in order to avoid excessive heating due to room temperature radiation).

In prior tests with similar diodes we found that the low temperature QE could be significantly increased by applying a larger bias voltage. However, in the present experiments on trapped H$\downarrow$ we have chosen not to take the chance of breakdown and resulting damage to the diode. Therefore, the diode is operated at 5 V bias voltage throughout.

5.5.2 Fluorescence measurement

For the measurement of the resonance fluorescence we take advantage of the cryogenic environment by applying a low-temperature bolometric detection technique. In general, a bolometer is a resistor which has a large temperature coefficient dR_{bolo}/dT and a very small heat capacity and which is poorly thermally linked to its environment. The energy dissipated in the resistor can be determined from the change in resistance. We have installed four 1 μm thick carbon film resistors on the inside of the cylindrical cell wall, which turn out to function as sensitive pulsed-light detectors, while protruding negligibly into the trap volume. Similar devices have been used before in many spin-polarized H experiments, e.g. to measure the kinetic energy carried by H$\downarrow$ atoms [30].

For our resistor films we use Aquadag [29], an aqueous dispersion of carbon powder, which is painted on a 50 μm thick Kapton substrate glued to the copper cell wall. The resistance is measured through 1 μm thick copper leads, vacuum-evaporated on the Kapton substrate. The resistor films are rectangles, 10 mm wide and 2 mm long. (For more information on the manufacturing of these detectors and on their exact positions in the experimental cell, see Chapter 4.) The carbon film consists of $\sim$ 250 Å thick graphite flakes with a typical diameter of 1 μm, regularly stacked with a packing fraction of $\sim$ 50% [31]. The superfluid ^{4}He film that covers all surfaces in the cell, will fill up the layer of stacked graphite flakes, so the resistor is effectively submersed in a $\sim$ 1 μm thick layer of liquid ^{4}He (see Fig. 5.6). The resistivity ρ at room temperature is $\sim$ 0.2 Ωcm, corresponding to a square resistance $R_\square = \rho/d = 2\,\mathrm{k}\Omega$ for a film of thickness $d = 1\,\mu$m. The resistive behaviour is completely different from that of semi-metallic graphite, as the electron transport is not bottlenecked by the graphite particles but by the inter-particle contact resistance. We measured the resistance of the bolometers as a function of temperature and fitted the data to an expression of the form $R_\square = (\rho_0/d)\exp[(T_0/T)^\beta]$ [30] (see Fig. 5.7). We find that the temperature dependence between 0.08 K and 4.2 K is in

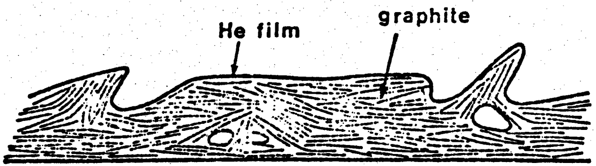

Figure 5.6: Schematic illustration of an Aquadag resistor film, covered with a thin layer of liquid helium [31].

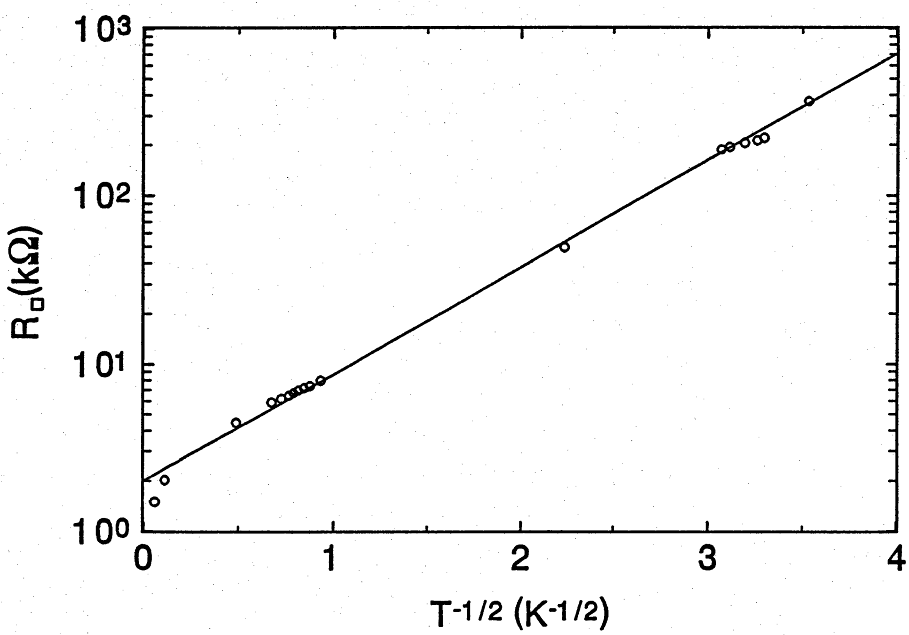

Figure 5.7: Square resistance of a ~ 1 μm thick Aquadag film resistor versus temperature. The solid line is a fit to theory (see text).

agreement with $\beta = 0.5$ and $T_0 = 2.15\,\mathrm{K}$. The temperature dependence is the same for all bolometers. For the particular bolometer of Fig. 5.7 we find $\rho_0/d = 2\,\mathrm{k\Omega}$. The temperature coefficient of this bolometer is $dR_\square/dT \approx 5\,\mathrm{k\Omega/mK}$ at $T = 0.1\,\mathrm{K}$ and $dR_\square/dT \approx 0.4\,\mathrm{k\Omega/mK}$ at $T = 0.2\,\mathrm{K}$.

The thermal behaviour of a bolometer is governed by its heat capacity C_{th} and the thermal resistance R_{th} to the environment. If relatively slow processes are studied, i.e. on time scales much longer than the thermal time constant $\tau_{th} = R_{th}C_{th}$, the response is only determined by R_{th}. In our application we want to measure pulsed heat loads so it is essential to incorporate the relevant heat capacities in the description. A simple model will now be presented which allows us to estimate the sensitivity and the response time of the Aquadag bolometers.

We assume the light pulse impinging on the bolometer is completely absorbed in the graphite particles, heating up the resistor. The heat capacity C_C of a 1 cm^2 graphite layer, 1 μm thick, packing fraction 50%, is given by $C_C/T \approx 1.2 \times 10^{-10}\,\mathrm{JK}^{-2}$, for $T \lesssim 0.2$ K [32]. Subsequently the heat will be transferred from the graphite particles to the substrate, either through direct contact with the Kapton or via the ^{4}He film. We assume that the thermal conductance associated with the direct contact is negligible. The thermal boundary (Kapitza) resistance R_{K1} between the graphite and the liquid for $T \lesssim 0.2$ K may be estimated using the expression $R_{K1}A_{K1}T^3 \approx 10^{-2}\,\mathrm{W}^{-1}\mathrm{K}^4\mathrm{m}^2$ [32] for the Kapitza resistance between a metal and liquid ^{4}He (A_K1 is the Kapitza surface area). Assuming that 50% of the graphite surface area contributes to A_K1, we find for a 1 μm thick, 1 cm^2 Aquadag film $R_{K1}T^3 \approx 5\,\mathrm{W}^{-1}\mathrm{K}^4$. The time constant $\tau_1 = R_{K1}C_C$ is then given by

$$\tau_1 T^2 \approx 6 \times 10^{-10}\,\mathrm{sK}^2, \tag{5.2}$$

so for $T = 0.2\,\mathrm{K}$ we find $\tau_1 \approx 15$ ns. This time constant, which is essentially the thermalization time of a single graphite flake, is independent of the thickness and the surface area of the resistor. This estimate suggests that the graphite thermalizes with the surrounding liquid on a very short time scale, comparable to the pulse duration of the incoming light. In reality the graphite is inhomogeneously heated, since the number of incident photons per pulse ($\lesssim 10^5$) is much smaller than the number of graphite platelets ($\sim 10^9$) in the film resistor. The above estimate (Eq. (5.2)) is only valid if the heat is first homogeneously distributed among the graphite platelets before it is transferred to the liquid. Probably, however, the "hot" platelets in the upper layers of the graphite film will give their heat to both the neighbouring platelets and the surrounding liquid so the distribution of heat in the graphite film and the liquid helium cannot be separated.

The heat capacity C_{He} of a 1 cm^2, 0.5 μm thick layer of liquid ^{4}He for $T \lesssim 0.5$ K is given by [32]

$$C_{\mathrm{He}}T^{-3} \approx 1.5 \times 10^{-7}\,\mathrm{JK}^{-4}. \tag{5.3}$$

For the relevant temperatures ($T \geq 0.1\,\mathrm{K}$) the heat capacity C_C of the graphite film can be neglected with respect to C_{He}. The Kapitza resistance R_{K2} between the liquid and the Kapton substrate is given by $R_{K2}A_{K2}T^3 = 7 \times 10^{-4}\,\mathrm{K}^4\mathrm{m}^2\mathrm{W}^{-1}$ [33], where A_{K2} is the geometrical surface area of the resistor film. For $A_{K2} = 1\,\mathrm{cm}^2$ this gives

$$R_{K2}T^3 = 7\,\mathrm{K}^4\mathrm{W}^{-1}. \tag{5.4}$$

The resulting time constant $\tau_2 = R_{K2}C_{\mathrm{He}}$ of the heat transport from the liquid to the substrate is proportional to the thickness of the resistor, but independent of the temperature and the surface area:

$$\tau_2 \approx 1\,\mu\mathrm{s}. \tag{5.5}$$

A comparison of the three relevant time scales, $\tau_p \approx \tau_1 \ll \tau_2$, gives rise to the following picture: The impinging VUV pulse heats up the ^{4}He film to a temperature determined by the pulse energy E_p and the heat capacity C_{He}; the graphite only acts as an intermediate absorber, converting the VUV energy instantly into heat. The bolometer R_{bolo} resistance changes simultaneously by an amount

$$\Delta R_{bolo} = (E_p/C_{\mathrm{He}})\frac{dR_{bolo}}{dT}. \tag{5.6}$$

Subsequently R_{bolo} relaxes to its original value on a time scale of approximately 1 μs. This is roughly in agreement with the experimentally observed (thermal/electronic) time constant of a few μs.

To determine the resistance change ΔR_{bolo} we send a DC bias current I_b through the resistor and measure the voltage drop. The maximum I_b that can be sent through is limited by DC heating of the bolometer, which results in a decrease in sensitivity. In general, the sensitivity is a very complicated function of the substrate temperature T_w and the bias current I_b. After a proper analysis, based on the above model (the heating of the resistor is completely determined by R_{K2} and C_{He}), we find that theoretically the largest signal is obtained for the lowest possible value of T_w and the value of the bias current $I_{b,max}$ for which the resistor film and the helium are heated up to approximately 10% above T_w. We find for a substrate temperature $T_w = 0.1\,\mathrm{K}$, $I_{b,max} \approx 4\,\mu\mathrm{A}$ and for $T_w = 0.2\,\mathrm{K}$ $I_{b,max} \approx 25\,\mu\mathrm{A}$, for 1 cm × 1 cm film resistors. It is clear that $I_{b,max}$ scales for a fixed temperature like $A_{K2}^{1/2}R_{bolo}^{-1/2}$, i.e. $I_{b,max} \sim w\sqrt{d}$, where w is the width of the resistor film.

We can now make an estimate of the detection sensitivity. At $T = 0.1\,\mathrm{K}$ absorption of one L$_\alpha$ photon by a 1 cm × 1 cm resistor will give rise to a signal $\Delta V = I_{b,max}\Delta R_{bolo} \approx 8 \times 10^{-8}\,\mathrm{V}$. Since the change in resistance $\Delta R_{bolo} \sim w^{-2}d^{-1}$ for a fixed heat load, the maximum achievable signal per incident photon $\Delta V \sim w^{-1}d^{-1/2}$. Our film resistors are 10 mm wide, 2 mm long, and approximately 1 μm thick, so at $T_w = 0.1\,\mathrm{K}$ $I_{b,max} \approx 4\,\mu\mathrm{A}$ and $\Delta V \approx 8 \times 10^{-8}\,\mathrm{V}$ per incident photon. At $T_w = 0.2\,\mathrm{K}$ the estimated maximum achievable signal ΔV is approximately 10× smaller than at $T_w = 0.1\,\mathrm{K}$.

References

[1] Special issue on laser cooling and trapping of atoms, edited by S. Chu and C. Wieman, J. Opt. Soc. Am. B **6**, No. 11 (1989).

[2] J. A. R. Samson, *Techniques of Vacuum Ultraviolet Spectroscopy* (John Wiley & Sons, 1967).

[3] R. Mahon, T. J. McIlrath, and D. W. Koopman, Appl. Phys. Lett. **33**, 305 (1978).

[4] H. Langer, H. Puell, and H. Röhr, Opt. Commun. **34**, 137 (1980).

[5] R. Hilbig and R. Wallenstein, IEEE J. Quantum Electron. QE-**15**, 1566 (1981).

[6] L. Cabaret, C. Delsart, and C. Blondel, Opt. Commun. **61**, 116 (1987).

[7] G. C. Bjorklund, IEEE J. Quantum Electron. QE-**11**, 287 (1975).

[8] Y. M. Yiu, T. J. McIlrath, and R. Mahon, Phys. Rev. A **20**, 2470 (1979).

[9] As the photoelectric yield of NO at L_α is very well known and the method of intensity measurements utilizing the photo ionization of a gas is very accurate and reproducible, NO ionization chambers are the standard for determining absolute L_α intensities.

[10] K. N. Drabovich, I. A. Kulagin, and T. Usmanov, Kvantovaya Electron. **12**, 616 (1985); Sov. J. Quantum Electron. **15**, 402 (1985).

[11] R. A. Ganeev, V. V. Gorbushin, I. A. Kulagin, and T. Usmanov, Appl. Phys. B **41**, 69 (1986).

[12] G. M. Weyl, D. I. Rosen, J. Wilson, and W. Seka, Phys. Rev. A **26**, 1164 (1982).

[13] Y. R. Shen, *The Principles of Nonlinear Optics* (John Wiley & Sons, 1984), Chapter 27.

[14] J. P. Marangos, N. Shen, H. Ma, M. H. R. Hutchinson, and J. P. Connerade, J. Opt. Soc. Am. B **7**, 1254 (1990).

[15] K. Hakuta, L. Marmet, and B. P. Stoicheff, Phys. Rev. A **45**, 5152 (1992).

[16] Solon Technologies, Inc. / Harshaw Crystal & Dosimetry Products, Solon, Ohio, U.S.A.

[17] *Handbook of Optics*, Optical Society of America (McGraw-Hill, 1978), p.7-95.

[18] L_1 is a biconvex lens, focal length at L_α $f = 44$ mm, $Tr = 57\%$, supplied by Harshaw.

[19] L_2 is a plano-convex lens, focal length at L_α $f = 48$ mm, $Tr = 60\%$, ground and polished by M. Groeneveld from a Harshaw-supplied MgF_2 window.

[20] W. A. VonDrasek, S. Okajima, and J. P. Hessler, Appl. Opt. **27**, 4057 (1988).

[21] Acton Research Corporation, U.S.A.

[22] P. P. Bey and H. Rabin, Phys. Rev. **162**, 794 (1967).

[23] P. P. Bey, J. F. Giuliani, and H. Rabin, Phys. Lett. **26A**, 128 (1968).

[24] H. Metcalf and J. C. Baird, Appl. Opt. **5**, 1407 (1966).

[25] A. C. Michels and T. v. Lieshout, unpublished.

[26] D. C. Thompson, M. S. O'Sullivan, B. P. Stoicheff, and G.-X. Xu, Can. J. Phys. **61**, 949 (1983).

[27] M. Krumrey, E. Tegeler, J. Barth, M. Krisch, F. Schäfers, and R. Wolf, Appl. Opt. **27**, 4336 (1988).

[28] R. B. Cairns and J. A. R. Samson, J. Opt. Soc. Am. **56**, 1568 (1966).

[29] Acheson Colloids Co., U.S.A.

[30] K. T. Salonen, I. F. Silvera, J. T. M. Walraven, and G. H. van Yperen, Phys. Rev. B**25**, 6002 (1982).

[31] K. T. Salonen, Rep. Ser. TURKU-FTL-R38, Department of Physical Sciences, University of Turku, Finland (1982).

[32] O. V. Lounasmaa, *Experimental Principles and Methods Below 1 Kelvin* (Academic Press, London, 1974).

[33] P. J. Nacher, P. Schleger, I. Shinkoda, and W. N. Hardy, Cryogenics **32**, 353 (1991).

[34] E. Tjukanov, M. Mertig, S. Vasilyev, and S. Jaakkola, unpublished data (1992).

[35] A. F. G. Wyatt, Phys. Rev. Lett. **69**, 1785 (1992).

Chapter 6

Lyman-α spectroscopy

6.1 Introduction

The application of resonant optical techniques to trapped H$\uparrow$ is very appealing for several reasons. It offers the possibility of *in situ*, non-destructive detection of the trapped particles, with a sensitivity much higher than that of the traditional (destructive) bolometric techniques [1, 2]. It also provides an independent means for determination of the temperature of the trapped gas, either by directly probing the spatial distribution of the particles in the trapping field, or by measuring the frequency dependence of the light scattering, which yields information about both the spatial distribution (Zeeman shifts) and the velocity distribution (Doppler shifts). In addition, the large resonant 1-photon absorption cross section opens the way to efficient optical manipulation (in particular optical cooling) of the gas. The Lyman-α transition (L_α, the first in the Lyman series) between the groundstate ($1S$) and the first excited state ($2P$) in atomic hydrogen [3], is experimentally the most accessible optical 1-photon transition for groundstate H atoms. In spite of its high transition frequency, which is far in the ultra-violet, it is therefore the most obvious one for the application of resonant optical techniques to trapped H$\uparrow$. The energy difference between the $1S$ state and the $2P$ state is 10.2 eV, corresponding to a transition frequency $\nu_\alpha = 2.47 \times 10^6\,\mathrm{GHz}$ and a wavelength $\lambda_\alpha = 121.6\,\mathrm{nm}$. The natural linewidth of the $2P$ state is $\Gamma/2\pi = 100\,\mathrm{MHz}$, corresponding to a radiative lifetime of $\Gamma^{-1} = 1.6\,\mathrm{ns}$.

Groundstate H atoms can also be excited by 2-photon absorption on the $1S \rightarrow 2S$ transition at a wavelength $2\lambda_\alpha = 243\,\mathrm{nm}$, a method developed for precision spectroscopy [4]. The 2-photon scheme offers a potentially much higher spectral resolution due to the narrow linewidth ($\sim 1\,\mathrm{Hz}$) of the metastable $2^2S_{1/2}$ state, the elimination of the first order Doppler effect, and the narrow bandwidth associated with the cw radiation sources available at 243 nm. A disadvantage is the low detection sensitivity due to the small 2-photon absorption cross section. Since our objective is not high resolution spectroscopy but sensitive detection and optical cooling of the trapped gas, we opted for the 1-photon L_α scheme. The application of the 2-photon scheme to trapped H$\uparrow$ is under development at MIT [5].

In this thesis the first optical experiments with magnetically trapped H$\uparrow$ are presented. The emphasis in this work is on diagnostics, i.e., the optical determination of the density and the temperature of the gas by L_α spectroscopy. The special conditions under which the spectroscopy is performed give rise to rather complicated spectra, generally consisting of five distinct, but partially overlapping lines with different strengths and asymmetric lineshapes. As we shall see, the main features of the spectra can be understood qualitatively as arising from averaging of the Zeeman shifted fine structure lines over the density distribution in the inhomogeneous trapping field. To extract reliable information on the density and the temperature of the gas, however, a more detailed understanding of the spectra is required which involves incorporating Doppler shifts, the position dependence of the absorption cross sections, strong attenuation of the light beam due to local optical thickness, effects associated with the varying angle between the polarization vector of the light and $\vec{B}$, and optical activity of the sample. In this chapter the calculation is treated in detail and the diagnostic method is illustrated with several examples of fits to the experimental spectra. Obviously, a detailed knowledge of the trapping field is required, for which the results of Chapter 2 are essential.

This chapter is organized as follows: In Sect. 6.2 the $1S \rightarrow 2P$ transition frequencies and probabilities are treated, in particular their magnetic field dependence. In Sect. 6.3 the relevant aspects of the general theory of the extinction of a light beam in a gas of resonant scatterers are reviewed. In Sect. 6.4 the results of the first two sections are applied to the calculation of transmission spectra of H$\uparrow$ samples in our specific geometry. In Sect. 6.5 several examples are given of experimental transmission spectra and their general features are explained. Some transmission spectra are analyzed thoroughly by fits using the exact theory of Sect. 6.4. The accuracy of this method for determining the temperature and the density of the trapped gas is discussed. Furthermore, an example is presented of a transmission spectrum of cold (non-trapped) atomic deuterium gas in our experimental cell. In Sect. 6.6 some examples of fluorescence spectra are given, which are analyzed using a simple preliminary model. This potentially powerful detection method has not yet been explored to the fullest.

6.2 Transition frequencies and probabilities

Due to its simple atomic structure, the energy levels and eigenstates of H can be calculated from first principles. For this reason the H atom has been the ideal testing ground for quantum electrodynamics and theoretical predictions of its energy levels have been verified experimentally to an extremely high degree of accuracy [4]. However, as our interest is not in high resolution spectroscopy, it is sufficient to know the absolute $1S \rightarrow 2P$ transition frequencies to the extent that we can tune the L_α frequency conveniently within the range of the $2P$ multiplet ($\gtrsim 10\,\mathrm{GHz}$), using a commercial wavemeter (Chapter 5). For our diagnostics it is of course essential that we have accurate expressions for the B-field dependence of the relative transition frequencies and of the transition probabilities.

In this section the B-field dependent fine structure of the $2P$ states is reviewed, mostly ignoring the effect of the nuclear spin. On the basis of the excited state fine structure and the ground state hyperfine structure the B-dependent transition frequencies and probabilities are deduced. Since the hyperfine structure of the $2P$ states can be completely ignored for $B > 0.05\,\mathrm{T}$, this is accurate enough for our purposes. For completeness, however, the hyperfine structure of the $2P$ states is also briefly discussed.

6.2.1 2P fine structure and 1S hyperfine structure

Neglecting the magnetic moment of the nucleus, the interaction of hydrogen atoms in the $2P$ state with an externally applied B-field is described by the following effective Hamiltonian:

$$H_{FS} = E_1 + (2/3)\Delta\,\vec{\ell}\cdot\vec{s} + \mu_B(\vec{\ell} + g_e\vec{s})\cdot\vec{B}. \tag{6.1}$$

Here $E_1 = \frac{3}{4}hcR_\infty(1 + m_e/m_n)^{-1} + E_{LS}$ is a reference energy, with R_∞ the Rydberg constant, m_e and m_n the mass of the electron and of the nucleus, respectively, and E_{LS} contains Lamb shift corrections. Further, Δ is the $B = 0$ fine structure splitting, $\vec{\ell}$ the electron orbital angular momentum, $\vec{s}$ the electron spin, and g_e the electron g-factor. The total electronic angular momentum is denoted by $\vec{j} = \vec{\ell} + \vec{s}$. We define zero energy as the $B = 0$ energy of the $1^2S_{1/2}$ groundstate when the hyperfine interaction is neglected (as in Chapter 3, Sect. 3.1). The $2P$ reference energy E_1 for hydrogen is given by $E_{1H}/h = 2\,466\,068\,\mathrm{GHz}$, and for deuterium by $E_{1D}/h = 2\,466\,739\,\mathrm{GHz}$ [6]. The fine structure splitting for hydrogen is $\Delta_H/h = 10.969\,\mathrm{GHz}$ and for deuterium $\Delta_D/h = 10.973\,\mathrm{GHz}$. For $B = 0$, the Hamiltonian H_{FS} yields two discrete energy levels corresponding to the $2^2P_{3/2}$ state ($j = \ell + s = 3/2$) and

Table 6.1: Energy levels and eigenstates of the ground state hyperfine structure and the first excited state fine structure of hydrogen in a magnetic field.

	m_j	energy	state
$2^2P_{3/2}$	$\frac{3}{2}$	$E_1+\Delta/3+(1+g_e/2)\mu_B B$	$\|1\uparrow\rangle$
	$\frac{1}{2}$	$E_1-\Delta/6+\mu_B B/2+(\Delta/2)\sqrt{1+2x/3+x^2}$	$\sin\theta_+\|0\uparrow\rangle+\cos\theta_+\|1\downarrow\rangle$
	$-\frac{1}{2}$	$E_1-\Delta/6-\mu_B B/2+(\Delta/2)\sqrt{1-2x/3+x^2}$	$\sin\theta_-\|-1\uparrow\rangle+\cos\theta_-\|0\downarrow\rangle$
	$-\frac{3}{2}$	$E_1+\Delta/3-(1+g_e/2)\mu_B B$	$\|-1\downarrow\rangle$
$2^2P_{1/2}$	$\frac{1}{2}$	$E_1-\Delta/6+\mu_B B/2-(\Delta/2)\sqrt{1+2x/3+x^2}$	$-\cos\theta_+\|0\uparrow\rangle+\sin\theta_+\|1\downarrow\rangle$
	$-\frac{1}{2}$	$E_1-\Delta/6-\mu_B B/2-(\Delta/2)\sqrt{1-2x/3+x^2}$	$-\cos\theta_-\|-1\uparrow\rangle+\sin\theta_-\|0\downarrow\rangle$
	h		
$1^2S_{1/2}$	d	$a_h/4+\mu^- B/2$	$\|0\uparrow\Uparrow\rangle$
	c	$-a_h/4+(a_h/2)[1+(\mu^+ B/a_h)^2]^{1/2}$	$\cos\theta\|0\uparrow\Downarrow\rangle+\sin\theta\|0\downarrow\Uparrow\rangle$
	b	$a_h/4-\mu^- B/2$	$\|0\downarrow\Downarrow\rangle$
	a	$-a_h/4-(a_h/2)[1+(\mu^+ B/a_h)^2]^{1/2}$	$\sin\theta\|0\uparrow\Downarrow\rangle-\cos\theta\|0\downarrow\Uparrow\rangle$

the $2^2P_{1/2}$ state ($j=\ell-s=1/2$):

$$\begin{aligned} E(2^2P_{3/2}) &= E_1+\Delta/3 \\ E(2^2P_{1/2}) &= E_1-2\Delta/3. \end{aligned} \tag{6.2}$$

For $B\neq 0$ the degeneracy in $m_j=m_\ell+m_s$ is lifted and straightforward diagonalization of H_{FS} results in six different energy levels, which are tabulated in Table 6.1 together with the corresponding eigenstates. Also tabulated are the hyperfine energies and states of the $1^2S_{1/2}$ hydrogen groundstate (see Chapter 3), which is convenient for the calculation of transition frequencies and probabilities.

The $2P$ energy levels are given in terms of the dimensionless field parameter x, which is defined by

$$x\equiv\frac{\mu_B B}{(g_e-1)\Delta}=\frac{B}{0.7819\,\mathrm{T}}. \tag{6.3}$$

The $2P$ eigenstates are expressed in the $|m_\ell, m_s\rangle$ basis, which is shorthand for the $|n, \ell, m_\ell, s, m_s\rangle$ basis with obvious values for n, ℓ, and s. The fine structure mixing angles $\theta_\pm$ are defined by

$$\sin\theta_\pm \equiv \sqrt{\frac{1+\delta_\pm}{2}}, \tag{6.4}$$

where

$$\delta_\pm = \frac{x \pm 1/3}{\sqrt{1 \pm 2x/3 + x^2}}. \tag{6.5}$$

Each $2P$ state has two-fold degeneracy with respect to the orientation of the nuclear spin $\vec{\imath}$. Therefore, for each $2P$ fine structure state in Table 6.1 one should read two hyperfine states, one $m_i = 1/2$ state ($\Uparrow$) and one $m_i = -1/2$ state ($\Downarrow$).

The $1^2S_{1/2}$ hyperfine states are expressed in the $|m_\ell, m_s, m_i\rangle$ basis, again in obvious notation. The ground state hyperfine parameters were already discussed in Chapter 3: The hyperfine splitting is $a_h/h = 1.420$ GHz, the hyperfine mixing angle θ is defined by $\tan 2\theta = a_h/(\mu^+ B)$, and $\mu^+ \approx \mu^- \approx 2\mu_B$. In Fig. 6.1(a) the $n = 1$ and $n = 2$ energy levels of H are plotted as a function of magnetic field. Also shown are the $2^2S_{1/2}$ levels, which are used in 2-photon spectroscopy, and the hyperfine structure of the $n = 2$ states, which will be discussed in 6.2.5.

6.2.2 H↑ fine structure transitions

The basis in which the eigenstates are expressed in Table 6.1 is very convenient to determine the allowed transitions, making use of general selection rules. In electric dipole transitions the electron spin $\vec{s}$ and the nuclear spin $\vec{\imath}$ are unaffected, i.e., $\Delta m_s = \Delta m_i = 0$, and m_ℓ may either change by unity or remain unchanged, $\Delta m_\ell = 0$ or ± 1 [3]. Transitions with $\Delta m_\ell = 0$ can only be excited by linearly polarized light with the polarization vector *parallel* to the quantization axis, and are called π transitions. Transitions with $\Delta m_\ell = \pm 1$ can only be excited if the polarization is perpendicular to the quantization axis, and are called σ (*senkrecht*) transitions. More specifically, for $\Delta m_\ell = 1$ (σ^+ transitions) one requires circularly polarized light with the electric field vector rotating clockwise for an observer looking in the direction of the quantization axis, and for $\Delta m_\ell = -1$ (σ^- transitions) circularly polarized light with the electric field vector rotating counter clockwise. The quantization axis is always defined by the local direction of the magnetic field vector, so the angle between the polarization vector and $\vec{B}$ determines which fraction of the light participates in the excitation of a certain transition. In an inhomogeneous field this gives rise to position dependent light absorption.

Assuming a pure d state gas in our trap, or, equivalently, neglecting the hyperfine structure of the ground state, one σ^+, two σ^-, and two π transitions are allowed,

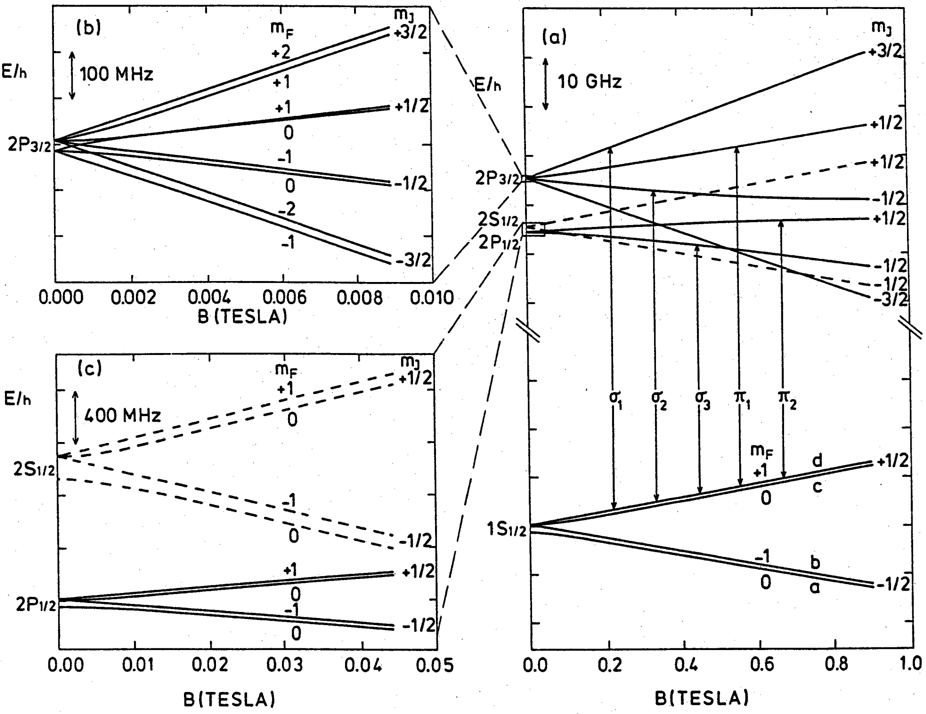

Figure 6.1: Energy levels of the ground state and first excited state of H. (a) An overview; (b) and (c) exploded views of the $2^2P_{3/2}$ and the $2^2P_{1/2}$, $2^2S_{1/2}$ manifolds, respectively, revealing the hyperfine structure of the $n = 2$ states. The arrows denote the allowed optical transitions from the d state.

which we label, respectively, σ_1, σ_2, σ_3, π_1, and π_2 (see Fig. 6.1). The nomenclature refers to the following excited states: $2^2P_{3/2}, m_j = 3/2$ (σ_1), $2^2P_{3/2}, m_j = 1/2$ (π_1), $2^2P_{3/2}, m_j = -1/2$ (σ_2), $2^2P_{1/2}, m_j = 1/2$ (π_2), and $2^2P_{1/2}, m_j = -1/2$ (σ_3). The corresponding transition frequencies, calculated using Table 6.1, are plotted as a function of B in Fig. 6.2.

Of the five allowed transitions from the d state only the σ_1 transition forms a closed cycle: The $2^2P_{3/2}|1\uparrow\Uparrow\rangle$ state can only decay to the d state. The other excited states have finite probabilities of decaying also to the c and a ground states, which can be easily calculated using Table 6.1. For example, the probability per unit time $\Gamma_{\pi1}$ for decay of the $2^2P_{3/2}|m_j = 1/2, \Uparrow\rangle$ state to the d state is $\Gamma_{\pi1} = \Gamma \sin^2\theta_+$, where Γ is the natural line width. Analogously, $\Gamma_{\pi2}/\Gamma = \cos^2\theta_+$, $\Gamma_{\sigma2}/\Gamma = \sin^2\theta_-$,

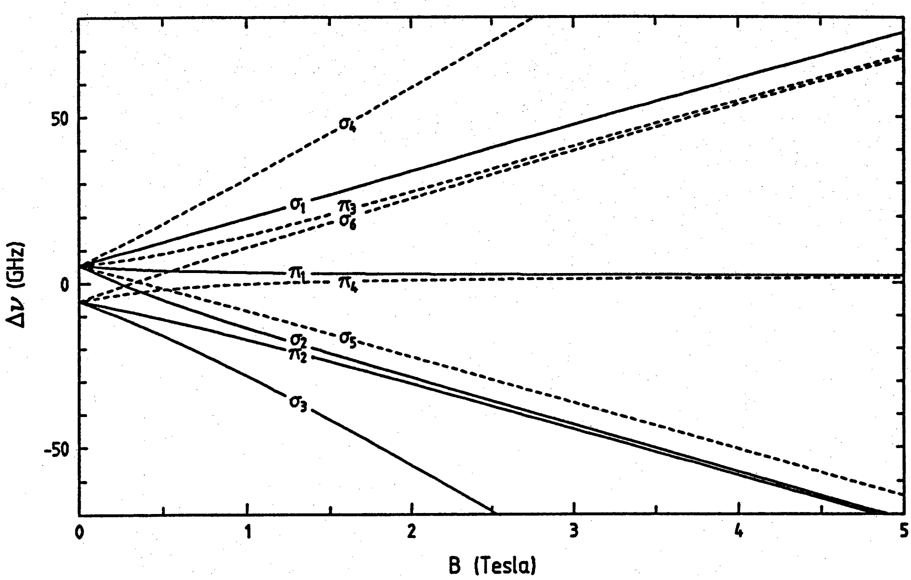

Figure 6.2: Frequencies of the 10 allowed $1S \to 2P$ fine structure transitions versus magnetic field. Solid curves: H↑ transitions; dashed curves: H↓ transitions. The frequencies are relative to $(E_1 - \Delta/6)/h$. In our experiments the relevant region for H↑ is $0.05\,\mathrm{T} \leq B \leq 1.5\,\mathrm{T}$ and for H↓ $B \approx 4.5\,\mathrm{T}$.

and $\Gamma_{\sigma 3}/\Gamma = \cos^2\theta_-$. In Fig. 6.3 the relative transition probabilities are plotted as a function of B. If $B \to \infty$ the relative transition probabilities either go to 1 or 0 which is due to the fact that all fine structure states approach pure m_s states in high field.

Clearly, when doing spectroscopy on any line except σ_1, one should take into account that particles are lost from the trap due to optical pumping to H↓ states. For instance, when shining in on the π_2 transition more than 2/3 of the excited atoms decay to a high-field seeking state.

The σ_1 transition in a finite magnetic field is effectively a two-level system. Consequently, monochromatic light with the proper polarization (rotating clockwise when looking in the direction of $\vec{B}$) which is exactly on resonance with σ_1 will be absorbed with the maximum cross section $3\lambda_\alpha^2/2\pi$ [7]. The absorption cross section scales with the transition probability, so for the other transitions from the d state the maximum cross section is always less and dependent on B. For example, the maximum cross section for resonant absorption on the π_1 transition is $3\lambda_\alpha^2 \sin^2\theta_+/2\pi$.

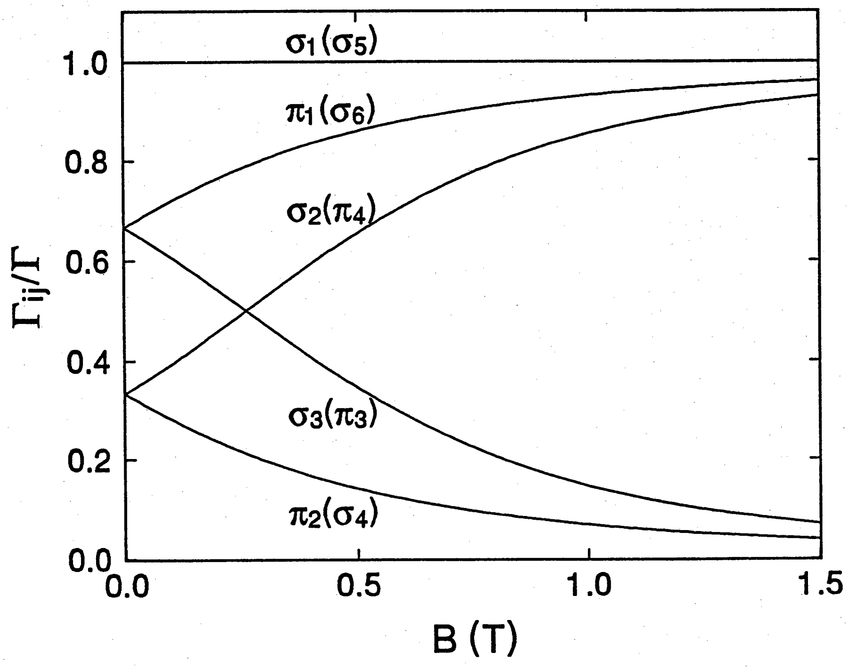

Figure 6.3: Relative transition probabilities Γ_{ij}/Γ of the five allowed transitions from the *d* (*b*) state as a function of magnetic field.

Summarizing, H↑ atoms in a magnetic trap with a non-zero field minimum give rise to at least five Zeeman shifted absorption lines. The local absorption of light of a certain frequency and polarization is strongly dependent on both the direction and the magnitude of $\vec{B}$, with a different dependence for each of the lines. The direction of $\vec{B}$ determines for each transition the component of the oscillating electric field vector participating in the excitation process; the magnitude $|\vec{B}|$ determines the local resonant absorption cross section and the local resonant frequency.

6.2.3 H↓ fine structure transitions

We are primarily interested in spectroscopy of trapped H↑ gas, but during the loading of the trap H↓ is also produced, which collects in the high field region (~ 4.5 T) and may cause extra absorption lines in the transmission spectrum of the sample. It is important that we can identify these H↓ lines as such.

From the high-field seeking doubly polarized *b* state one σ^-, two σ^+, and two

π transitions are allowed, which are labeled σ_4, σ_5, σ_6, π_3, and π_4. The transitions can be defined in terms of their excited states: $\sigma_4 \rightarrow 2^2P_{3/2}, m_j = 1/2$; $\sigma_5 \rightarrow 2^2P_{3/2}, m_j = -3/2$; $\sigma_6 \rightarrow 2^2P_{1/2}, m_j = 1/2$; $\pi_3 \rightarrow 2^2P_{3/2}, m_j = -1/2$; and $\pi_4 \rightarrow 2^2P_{1/2}, m_j = -1/2$. The transition frequencies are plotted as a function of B in Fig. 6.2 (dashed curves). The corresponding relative transition probabilities are shown in Fig. 6.3: $\Gamma_{\sigma 4} = \Gamma_{\pi 2}$, $\Gamma_{\sigma 5} = \Gamma_{\sigma 1}$, $\Gamma_{\sigma 6} = \Gamma_{\pi 1}$, $\Gamma_{\pi 3} = \Gamma_{\sigma 3}$, and $\Gamma_{\pi 4} = \Gamma_{\sigma 2}$.

6.2.4 H↑ hyperfine transitions

If we allow for the presence of c state atoms in the trapped gas the situation becomes more complicated. Applying the electric dipole selection rules again to Table 6.1 we find that 10 additional transitions to $2P$ states are allowed. The five of these associated with the $|0\uparrow\downarrow\rangle$ part of the c state are very similar to the five allowed transitions from the d state: Two σ^-, one σ^+, and two π transitions are allowed to the same $2P$ fine structure states. The corresponding transition frequencies only differ from those of the σ_1, σ_2, σ_3, π_1, and π_2 transitions (Fig. 6.2) by an amount equal to the $c - d$ transition frequency ($\sim 0.6\,\mathrm{GHz}$ for $B \geq 0.1\,\mathrm{T}$). The transition probabilities can be obtained by simply multiplying the fine structure transition probabilities (Fig. 6.3) by the hyperfine mixing parameter $\cos^2\theta$, which is close to unity in most cases ($\cos^2\theta \geq 0.95$ for $B \geq 0.1\,\mathrm{T}$).

The $|0\downarrow\uparrow\rangle$ part of the c state gives rise to two σ^+, one σ^-, and two π transitions. The σ^- transition excites the $2^2P_{3/2}, m_j = -3/2$ state, which is not accessible from the d state and forbidden if only fine structure is taken into account. The contributions of the latter five transitions are very small in most cases since their transition probabilities are suppressed by a factor $\sin^2\theta$ (≤ 0.05 for $B \geq 0.1\,\mathrm{T}$).

The Zeeman and Doppler broadening associated with the relatively high temperatures ($T \gtrsim 0.05\,\mathrm{K}$) of the experiments described in this thesis, prevented the resolution of the $1^2S_{1/2}$ hyperfine structure.

6.2.5 2P hyperfine structure

If the magnetic moment of the nucleus is taken into account, the interaction of hydrogen atoms in the $2P$ state with an externally applied magnetic field is described by the following effective Hamiltonian [8]:

$$\begin{aligned} H_{HF} &= E_1 + (2/3)\Delta\vec{\ell}\cdot\vec{s} + a_j\vec{\imath}\cdot\vec{\jmath} + (a_h/128)\vec{\imath}\cdot\vec{\ell} \\ &\quad + [\mu_B\vec{\ell} + g_e\mu_B\vec{s} + g_n\mu_n\vec{\imath}]\cdot\vec{B}, \end{aligned} \tag{6.6}$$

where $a_j = a_h/32j(j+1)$, μ_n the nuclear magneton, and g_n the nuclear g-factor. For $B = 0$, the Hamiltonian H_{HF} is, to a very good approximation, diagonal in the $|n,\ell,j,F,m_F\rangle$ basis, where $\vec{F}=\vec{\ell}+\vec{s}+\vec{\imath}$ is the total angular momentum. The only off-diagonal elements are due to the $\vec{\imath}\cdot\vec{\ell}$ term, which causes very weak coupling between between states with different j and can be safely neglected. Thus we have to a very good approximation the following four energy levels for $B=0$ (see Fig. 6.1):

$$\begin{aligned}E(2^2P_{3/2},F=2) &= E_1+\Delta/3+a_h/160\\ E(2^2P_{3/2},F=1) &= E_1+\Delta/3-a_h/96\\ E(2^2P_{1/2},F=1) &= E_1-2\Delta/3+a_h/96\\ E(2^2P_{1/2},F=0) &= E_1-\Delta/3-a_h/32.\end{aligned}\tag{6.7}$$

The hyperfine splitting of the $2^2P_{3/2}$ level is $a_h/60h \approx 24\,\mathrm{MHz}$ and of the $2^2P_{1/2}$ level $a_h/24h \approx 60\,\mathrm{MHz}$. If we compare this to the natural linewidth of the $2P$ states ($\Gamma/2\pi = 100\,\mathrm{MHz}$) and the bandwidth of our L_α source ($\sim 100\,\mathrm{MHz}$) it is clear that the $2P$ hyperfine structure cannot be resolved spectrally.

Due to the hyperfine interaction the $2P$ eigenstates are no longer the fine structure states discussed in Sect. 6.2.1. As a result the nature ($\sigma^\pm$, π) of the $1S \rightarrow 2P$ transitions changes and new transitions appear which are forbidden in fine structure. For L_α spectroscopy in relatively low fields ($B \lesssim 0.01\,\mathrm{T}$), when $2P$ hyperfine effects become noticeable, it is therefore necessary to determine the B-dependent eigenstates of H_{HF}, which in general requires diagonalizing a 12×12 matrix. Since H_{HF} is diagonal in m_F, the matrix representation of H_{HF} in the $|n,\ell,j,F,m_F\rangle$ basis can be separated in submatrices of a given m_F. The problem is then reduced to the diagonalization of two 3×3 matrices (for the $m_F=\pm1$ states) and one 4×4 matrix (for the $m_F=0$ states), whose B-dependent elements are tabulated in Ref. [8]. The two $|n=0,\ell=1,j=3/2,F=2,m_F=\pm2\rangle$ states are already eigenstates of H_{HF}. In principle this problem can be solved analytically, but it results in very complicated expressions which do not give much insight. Numerical diagonalization is more straightforward.

However, it is also possible to determine relatively simple closed expressions for the eigenstates by making use of the fact that, depending on the field, certain terms in H_{HF} can be treated as small perturbations. We distinguish two field regimes: $B \gg 0.004\,\mathrm{T}$ (regime I) in which approximation I holds, and $B \ll 0.8\,\mathrm{T}$ (regime II) in which approximation II holds. The approximations are discussed below. Since the two regimes have a large overlap, there is a smooth transition between the two approximations. Therefore, accurate closed expressions for the eigenstates can be obtained for all values of B.

For $\mu_B B \gg a_j$ ($B \gg 0.004\,\mathrm{T}$), the hyperfine terms

$$a_j\vec{\imath}\cdot\vec{\jmath}+(a_h/128)\vec{\imath}\cdot\vec{\ell},$$

which couple states with different m_i, contribute negligibly. In approximation I these terms are left out. In that case the eigenstates are the fine structure states already discussed in Sect. 6.2.1. If desired, the hyperfine admixture of the states with different m_i can be simply obtained by first order perturbation theory.

For $\mu_B B \ll \Delta$ ($x \ll 1$ or $B \ll 0.8\,\mathrm{T}$), coupling between states with different j may be neglected, which is equivalent to subtracting the terms

$$\mu_B(g_e - 1)\vec{s}\cdot\vec{B} + (a_h/128)\vec{\imath}\cdot\vec{\ell}$$

from H_{HF}. In approximation II these terms are left out. In the $|n, \ell, j, F, m_F\rangle$ matrix representation the problem is then reduced to straightforward diagonalization of 2×2 submatrices. The eigenstates in this approximation are four pure $|n, \ell, j, F, m_F\rangle$ states and eight states which are linear combinations of two $|n, \ell, j, F, m_F\rangle$ states, which only differ in the quantum number F. The 12 corresponding B-dependent eigenvalues very accurately describe the $2P$ hyperfine structure displayed in Fig. 6.1 (b) and (c). Again, the admixture of states with different j can be accounted for by first order perturbation theory.

A practical criterion is to use approximation I for $B \geq 0.015\,\mathrm{T}$ and approximation II for $B \leq 0.015\,\mathrm{T}$. For $B \approx 0.015\,\mathrm{T}$ the two approximations are equally accurate: for both approximations the admixtures due to the perturbation part of H_{HF} amount to a few percent for $B \approx 0.015\,\mathrm{T}$.

Since $2P$ hyperfine effects are completely negligible in the experiments described in this thesis ($B \geq 0.05\,\mathrm{T}$) the expressions for the $2P$ hyperfine eigenstates and energies are not given here.

6.3 Resonant light scattering in a dilute gas

In this section some aspects of the general theory of the extinction of a light beam in a gas of resonant scatterers are reviewed, to the extent necessary for the understanding of our spectra. The treatment is semiclassical, with a classical representation of the electromagnetic field but a quantum mechanical description of the atomic states. The description is slightly more involved than in the usual treatments (for example, Refs. [7, 9]), because we have to deal with multilevel atoms, and because the vector character of the light has to be taken into account explicitly.

6.3.1 Classical light propagation

From Maxwell's equations for a dielectric medium the following general wave equation can be derived straightforwardly:

$$\vec{\nabla}^2\vec{E} - \epsilon_0\mu_0\frac{\partial^2\vec{E}}{\partial t^2} = \mu_0\frac{\partial^2\vec{P}}{\partial t^2} - \frac{1}{\epsilon_0}\vec{\nabla}(\vec{\nabla}\cdot\vec{P}). \tag{6.8}$$

Here $\vec{E}$ is the electric field vector and $\vec{P}$ the induced polarization. We are interested in the extinction of a plane electromagnetic wave in a dilute polarizable medium, so we write $\vec{E}$ and $\vec{P}$ in the form

$$\begin{aligned} \vec{E}(\vec{r},t) &= \vec{E}_0(\vec{r},t)e^{i(kz-\omega t)}, \\ \vec{P}(\vec{r},t) &= \vec{P}_0(\vec{r},t)e^{i(kz-\omega t)}, \end{aligned} \tag{6.9}$$

where $k = \omega/c = \omega\sqrt{\epsilon_0\mu_0}$ is the wave number in vacuum of a plane wave with frequency ω propagating in the z direction. If we assume $\vec{E}_0(\vec{r},t)$ and $\vec{P}_0(\vec{r},t)$ are slowly varying functions of $\vec{r}$ and t:

$$|\frac{\partial\vec{E}_0}{\partial t}| \ll \omega|\vec{E}_0|,\ |\frac{\partial\vec{E}_0}{\partial t}| \ll c|\frac{\partial\vec{E}_0}{\partial z}|,\ |\frac{\partial\vec{P}_0}{\partial t}| \ll \omega|\vec{P}_0|, \tag{6.10}$$

and

$$|\vec{\nabla}^2\vec{E}_0| \ll 2k|\frac{\partial\vec{E}_0}{\partial z}|,\ |\vec{\nabla}(\vec{\nabla}\cdot\vec{P}_0)| \ll k|\vec{\nabla}\cdot\vec{P}_0| \ll k^2|\vec{P}_0|, \tag{6.11}$$

and we neglect all but the largest terms in Eq. (6.8) (slowly varying amplitude approximation), then we arrive at

$$\frac{\partial\vec{E}_0}{\partial z} = \frac{ik}{2\epsilon_0}[\vec{P}_0 - (\vec{P}_0\cdot\vec{e}_z)\vec{e}_z]. \tag{6.12}$$

This is our basic equation for the calculation of the propagation of a L_α beam through a sample of trapped H$\uparrow$. The induced polarization gives rise to both extinction and dispersion of the light. In general $\vec{E}_0$ is not parallel to $\vec{P}_0$. In Sect. 6.3.2 we will show that the induced polarization can be written as

$$\vec{P}_0 = \epsilon_0\overleftrightarrow{\chi}\vec{E}_0, \tag{6.13}$$

where $\overleftrightarrow{\chi}$ is the complex susceptibility tensor, which can be derived from microscopic quantum mechanical theory.

6.3.2 Complex susceptibility tensor

Consider a collection of motionless 2-level atoms subjected to the perturbing effect of a stationary electromagnetic wave $\vec{E}_0\exp[i(kz-\omega t)]$, whose frequency ω is close to the electric dipole transition frequency ω_0. The induced polarization is equal to the product of the density of the particles and the expectation value of the electric dipole moment. Assuming the light intensity is so low that the population of the excited state $|2\rangle$ is negligible with respect to the population of the ground state $|1\rangle$, one may derive straightforwardly [7, 9]

$$\vec{P}_0 = \frac{n(\vec{D}_{12} \cdot \vec{E}_0)\vec{D}_{21}}{\hbar(\omega_0 - \omega - i\Gamma/2)}, \tag{6.14}$$

where n is the density of the atoms, $\vec{D}_{12} \equiv \langle 1|e\vec{r}|2\rangle$ the electric dipole matrix element, and $\Gamma = k^3|\vec{D}_{12}|^2/3\pi\epsilon_0\hbar$ the natural linewidth of the transition. From Eq. (6.14) immediately follows the susceptibility tensor $\overleftrightarrow{\chi}_0$ for a gas at $T = 0$:

$$\overleftrightarrow{\chi}_0 = \frac{6\pi n}{k^3} \frac{\vec{D}_{12}\vec{D}^*_{12}}{|\vec{D}_{12}|^2} \left(\frac{\omega_0 - \omega}{\Gamma/2} - i\right)^{-1}. \tag{6.15}$$

Eq. (6.15) can be readily extended to more complex multilevel sytems:

$$\overleftrightarrow{\chi}_0 = \frac{6\pi}{k^3} \sum_{\ell,j} n_\ell \frac{\vec{D}_{\ell j}\vec{D}^*_{\ell j}}{\sum_f |\vec{D}_{fj}|^2} \left(\frac{\omega_{\ell j} - \omega}{\Gamma/2} - i\right)^{-1}, \tag{6.16}$$

where $\vec{D}_{\ell j}$ is the electric dipole matrix element between a ground state ℓ and an excited state j, $\omega_{\ell j}$ the corresponding transition frequency, and n_ℓ the density of atoms in the ℓ state. Eq. (6.16) only holds if the spacing between the ground state sublevels ℓ and the spacing between the excited state sublevels j is negligible with respect to $\omega_{\ell j}$, so that for all excited states $\Gamma_j \equiv k^3 \sum_f |\vec{D}_{fj}|^2/3\pi\epsilon_0\hbar = \Gamma$. This is clearly the case for the $1S \rightarrow 2P$ transitions in H. Further, for Eq. (6.16) to be valid it is necessary that the depletion of the ground state levels is negligible. We will discuss the latter assumption in more detail in Sect. 6.3.3.

For the $1S \rightarrow 2P$ transitions in trapped H$\uparrow$ the matrix elements $\vec{D}_{\ell j}$ generally depend on $\vec{B}$, whereas $\omega_{\ell j}$ and n_ℓ depend on $|\vec{B}|$. Note that the transition probabilities discussed in Sect. 6.2 are connected to the electric dipole matrix elements by the relation

$$\frac{\Gamma_{\ell j}}{\Gamma} = \frac{|\vec{D}_{\ell j}|^2}{\sum_f |\vec{D}_{fj}|^2}. \tag{6.17}$$

6.3.3 Power broadening

If the light intensity is so high that power broadening becomes appreciable, i.e., if the population of the excited state(s) can no longer be neglected, the description becomes much more complicated.

First, to estimate the influence of power broadening, which is in principle straightforward in the case of 2-level atoms and a cw light beam [7, 9], knowledge of the light intensity is required, which is a quantity with a large experimental uncertainty in our experiments. Second, for a multilevel system with non-negligible depletion of the ground states there is no longer a closed expression for the susceptibility: the full optical Bloch equations have to be solved (position dependent, in our case), involving all levels. Third, our light source is not cw but pulsed, with a pulse duration $\tau_p \approx 10\,\mathrm{ns} \approx 6\Gamma^{-1}$ (Γ^{-1} is the natural lifetime of the $2P$ state), which is too short to reach the steady state population of the excited states [7]. As a result the propagation of light at high intensities becomes sensitive to the detailed shape of the pulse.

Therefore, for a reliable, quantitative understanding of the spectra it is essential that our light intensity stays well below the saturation threshold. For a 2-level system this means the Rabi frequency $|\vec{D}_{12} \cdot \vec{E}_0|/\hbar$ should be much smaller than $\Gamma/2$. This condition can be expressed as

$$I \ll \frac{k^3 c\hbar\Gamma}{24\pi}, \tag{6.18}$$

where $I = \frac{1}{2}\epsilon_0 c|\vec{E}_0|^2$ is the light intensity. For the L_α transition this means the intensity should stay well below $I = 3.6\,\mathrm{W/cm^2}$. In our experiment we typically have $\sim 5 \times 10^7$ photons per 10 ns pulse and a $\sim 1\,\mathrm{mm}$ beam radius, corresponding to $I \approx 0.25\,\mathrm{W/cm^2}$.

6.3.4 Doppler broadening

Up to now we assumed the atoms to be at rest. If we allow them to move the resonant frequencies will be Doppler shifted. After averaging over the velocity distribution this gives rise to inhomogeneous line broadening. An atom with a velocity component v_z along the direction of the light propagation has shifted resonant frequencies

$$\omega'_{\ell j} = \omega_{\ell j}(1 - v_z/c). \tag{6.19}$$

Replacing $\omega_{\ell j}$ in Eq. (6.16) by $\omega'_{\ell j}$ and averaging over a Maxwell-Boltzmann velocity distribution,

$$\overleftrightarrow{\chi} = (2\pi k_B T/m)^{-1/2} \int_{-\infty}^{\infty} dv_z \; \overleftrightarrow{\chi}_0 \, (\omega'_{\ell j}) \exp(-m v_z^2/k_B T), \tag{6.20}$$

we find

$$\overleftrightarrow{\chi} = i\frac{6\pi^{3/2}}{k^3} \sum_{\ell,j} n_\ell \frac{\vec{D}_{\ell j}\, \vec{D}^*_{\ell j}}{\sum_f |\vec{D}_{fj}|^2} \frac{\Gamma}{2b} w(\zeta_{\ell j}), \tag{6.21}$$

where $b = k\sqrt{2k_B T/m}$, $w(\zeta) = e^{-\zeta^2}\mathrm{erfc}(-i\zeta)$, and $\zeta_{\ell j} = (\omega - \omega_{\ell j} + i\Gamma/2)/b$. The real part of the complex error function w is the Voigt profile describing a Doppler broadened line. In the literature the so-called plasma dispersion function $Z(\zeta) = i\sqrt{\pi}w(\zeta)$

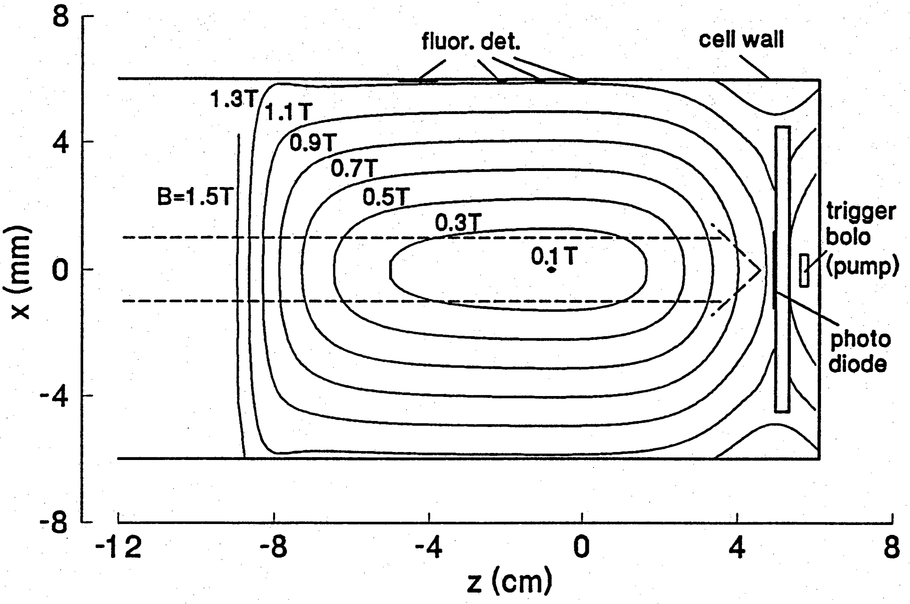

Figure 6.4: Schematic overview of the experimental situation. Indicated are the magnetic field contours, the positions of the detectors, and the light beam (dashed arrow).

is often used instead of $w(\zeta)$. For computational purposes a useful approximation of $w(\zeta)$ in terms of generalized Lorentzians is given in Ref. [10]. For $b \gg \Gamma/2$, i.e., for $T \gg 9\,\mathrm{mK}$ in our case, the Voigt lineshape function reduces to a Gaussian function with a FWHM Doppler linewidth $\Delta\omega_D = 2b\sqrt{\ln 2}$. In our case the FWHM Doppler linewidth is given by $\Delta\nu_D/\sqrt{T} = 1.76\,\mathrm{GHzK}^{-1/2}$. For $b \ll \Gamma/2$ ($T \ll 9\,\mathrm{mK}$), the Voigt lineshape approaches a Lorentz lineshape with a FWHM linewidth $\Delta\omega_L = \Gamma$, and the expression (6.21) for $\overleftrightarrow{\chi}$ may be replaced by the simpler expression (6.16).

Eq. (6.21) together with the equation for the propagation of the electric field amplitude,

$$\frac{\partial \vec{E}_0}{\partial z} = \frac{ik}{2}[\overleftrightarrow{\chi}\,\vec{E}_0 - (\overleftrightarrow{\chi}\,\vec{E}_0 \cdot \vec{e}_z)\vec{e}_z], \tag{6.22}$$

forms the basis for the calculation of the spectra.

6.4 Application to trapped H↑

In our experiments a L_α beam with a radius of $\sim 1\,\mathrm{mm}$ enters the experimental cell along the z-axis (see Fig. 6.4). The H↑ sample, located near the centre, has a spatial extent which depends on temperature: A typical temperature of $T = 0.1\,\mathrm{K}$ corresponds to a spread in magnetic fields $\Delta B \sim k_B T/\mu_B = 0.15\,\mathrm{T}$ and thus to a sample radius of ~ 1 mm (see Sect. 3.2.4), comparable to the beam radius. The light beam passes through the gas, is partially scattered, and hits a photodiode (sensitive area 2.3 mm × 2.3 mm). Part of the light scattered by the sample is absorbed by bolometric fluorescence detectors on the cylindrical side wall. In our experiments up till now the information on the trapped gas has been obtained mainly by measurement of the frequency dependence of the transmitted light intensity. Before going into the details of the calculation of the transmission spectra we will make some general remarks on the light propagation through the trapped gas, motivating our theoretical approach.

6.4.1 Phenomenology

The resonant absorption cross section for L_α can be as high as $3\lambda_\alpha^2/2\pi$, which at a typical density $n = 10^{12}\,\mathrm{cm}^{-3}$ corresponds to a resonant extinction length $\ell_{ext} = 2\pi/(3n\lambda_\alpha^2) = 0.14\,\mathrm{mm}$. In practice the resonant absorption cross section is smaller, mainly due to Doppler broadening and polarization effects, but still it is so large that already at moderate densities the H$\uparrow$ sample becomes optically thick at resonant frequencies. Under these conditions the sample actually casts a shadow on the photodiode. Since the dimensions of the photodiode are comparable to the beam diameter and comparable to or larger than the radial sample size, the intensity of the light incident on the photodiode can be strongly varying over its surface.

The combination of strong absorption and a magnetic field induce substantial changes of the polarization of the light while it passes through the sample. This necessitates a description of the light propagation in terms of the electric field vector. To illustrate this point, suppose linearly polarized light is incident on the sample at a frequency resonant with a σ^+ transition, but, due to Zeeman splitting, not in resonance with any σ^- transition. Then, if the magnetic field vector is parallel to the direction of the propagating light, only left-circularly polarized light will be absorbed, changing the polarization of the light from linear to right-circular. As in Ioffe traps the orientation of $\vec{B}$ is varies strongly with position, the evolution of the polarization is in general quite complicated in our samples. The H$\uparrow$ sample is not just a simple polarizer.

Optical thickness goes hand in hand with strong dispersive effects. To make an estimate of these effects we neglect the vector character of the light for the moment. For a dilute medium of two-level atoms at rest the refractive index η is then given by [7]:

$$\eta - 1 = \frac{\pi n}{k^3} \frac{\frac{\omega_0 - \omega}{\Gamma/2}}{1 + (\frac{\omega_0 - \omega}{\Gamma/2})^2}, \tag{6.23}$$

where ω_0 is the resonant frequency and Γ the natural linewidth. From Eq. (6.23) follows that the refractive index of trapped H↑ gas ($n \leq 10^{14}\,\mathrm{cm}^{-3}$) at the L_α wavelength is always very close to unity: $(\eta - 1)_{max} \approx 1 \times 10^{-3}$. For typical densities $n \leq 10^{12}\,\mathrm{cm}^{-3}$, $\eta - 1 \leq 10^{-5}$ so refractive effects are completely negligible. Dispersion, however, is still important. A light wave travelling a distance Δz through the sample acquires a phase shift $\Delta\phi = (\eta - 1)k\Delta z$ with respect to a wave in vacuum. If the frequency of the light is tuned near resonance, $\omega_0 - \omega = \Gamma/2$, a phase shift $\Delta\phi = 1$ is acquired over a distance $\Delta z = 8\pi/n\lambda_\alpha^2$, which is twice the extinction length ℓ_{ext} at this detuning. Such effects strongly enhance the polarization changes caused by absorption of the light. Moreover, for large detuning dispersive effects can still be appreciable while the absorption is small. For example, when tuned halfway between a σ^+ and a σ^- line both circular components of a linearly polarized light beam will be weakly, but equally, absorbed, thus keeping the light linearly polarized. The real parts of the susceptiblities associated with the two transitions, however, have opposite signs, causing an increasing phase shift between the two circular wave components and thus rotation of the total, linear, polarization. This so-called Faraday rotation is a purely dispersive effect.

These considerations indicate that in order to calculate spectra reliably, it is necessary to keep track of the intensity, the polarization, and the phase of the light propagating through the sample. Therefore we have to integrate Eq. (6.22) for each frequency and for all light trajectories ending on the photodiode surface. In view of the complicated dependence of $\overleftrightarrow{\chi}$ on position, this is quite a task. Fortunately it is possible to reduce the problem to a manageable size by making use of the symmetries of our experimental situation.

6.4.2 Calculation of transmission spectra

In order to write Eq. (6.22) in a practical and more transparent form, we introduce the vector basis ($\vec{e}_1$, $\vec{e}_2$, $\vec{e}_3$) for the polarization vector of the light, defined by

$$\begin{aligned} \vec{e}_3 &= \vec{k}/k, \\ \vec{e}_2 &= (\vec{e}_3 \times \vec{B})/B, \\ \vec{e}_1 &= \vec{e}_2 \times \vec{e}_3, \end{aligned} \tag{6.24}$$

where $\vec{k}$ is the wave vector of the unscattered light. The $\vec{e}_3$-axis, defined by the propagation direction of the light, is identical to the z-axis, while the $\vec{e}_1$-axis is defined in such a way that $\vec{B}$ always lies in the plane of $\vec{e}_1$ and $\vec{e}_3$. Since the angle of the magnetic field in the plane perpendicular to the z-axis is independent of z (see Chapter 2), Eqs. (6.24) unambiguously define a single vector basis for each light trajectory. (Actually, this is only approximately the case since the radial component of $\vec{B}$ rotates slightly as a function of z due to finite length effects of the racetracks (Fig. 2.6); for the present purposes this can be completely neglected.)

The electric field amplitude $\vec{E}_0$ may be expressed in either a linear or a circular polarization basis:

$$\vec{E}_0 = E_{01}\vec{e}_1 + E_{02}\vec{e}_2 = E_{0+}\vec{e}_+ + E_{0-}\vec{e}_-, \tag{6.25}$$

where $\vec{e}_\pm \equiv (\vec{e}_1 \pm i\vec{e}_2)/\sqrt{2}$. The unit vector $\vec{e}_+$ ($\vec{e}_-$) corresponds to left(right)-circularly polarized light. As we shall see, the circular polarization basis is the one most convenient for our purposes.

The matrix representation of the susceptibility tensor $\overleftrightarrow{\chi}$ takes a simple diagonal form $\left[\overleftrightarrow{\chi}\right]'$ in the $(\vec{e}_\pm{}', \vec{e}_3{}')$ basis, defined by $\vec{e}_3{}' = \vec{B}/B$, $\vec{e}_2{}' = \vec{e}_2$, $\vec{e}_1{}' = \vec{e}_2{}' \times \vec{e}_3{}'$, and $\vec{e}_\pm{}' = (\vec{e}_1{}' \pm i\vec{e}_2{}')/\sqrt{2}$, which is simply the $(\vec{e}_\pm, \vec{e}_3)$ basis, rotated in the plane of $\vec{k}$ and $\vec{B}$ in such a way that $\vec{e}_3{}' \parallel \vec{B}$:

$$\left[\overleftrightarrow{\chi}\right]' = \begin{pmatrix} \chi_+ & 0 & 0 \\ 0 & \chi_- & 0 \\ 0 & 0 & \chi_z \end{pmatrix}. \tag{6.26}$$

Here χ_+ is defined by

$$\chi_+ \equiv i\frac{6\pi^{3/2}}{k^3}\sum_{\ell,j} n_\ell \frac{|\vec{D}_{\ell j}|^2}{\sum_f |\vec{D}_{fj}|^2}\frac{\Gamma}{2b}\, w(\zeta_{\ell j}) = i\frac{6\pi^{3/2}}{k^3}\sum_{\ell,j} n_\ell \frac{\Gamma_{\ell j}}{2b}\, w(\zeta_{\ell j}), \tag{6.27}$$

where the ℓ, j summation is restricted to σ^+ transitions. χ_- and χ_z are defined analogously, with the ℓ, j summation restricted to, respectively, σ^- and π transitions. When only transitions from the d state are taken into account we find, using the results of the previous sections,

$$\begin{aligned} \chi_+ &= i(6\pi^{3/2}/k^3)\, n_d\, (\Gamma/2b)\, w(\zeta_{\sigma 1}), \\ \chi_- &= i(6\pi^{3/2}/k^3)\, n_d\, (\Gamma/2b)\, [\sin^2\theta_-\, w(\zeta_{\sigma 2}) + \cos^2\theta_-\, w(\zeta_{\sigma 3})], \\ \chi_z &= i(6\pi^{3/2}/k^3)\, n_d\, (\Gamma/2b)\, [\sin^2\theta_+\, w(\zeta_{\pi 1}) + \cos^2\theta_+\, w(\zeta_{\pi 2})]. \end{aligned} \tag{6.28}$$

The magnetic field dependence is contained in the d atom density n_d, the fine structure mixing angles $\theta_\pm$, and the frequency detuning parameters $\zeta_{\ell j}$.

The unitary matrix A for transformation from a $(\vec{e}_\pm, \vec{e}_3)$ representation to a $(\vec{e}_\pm{}', \vec{e}_3{}')$ representation is given by

$$A = \begin{pmatrix} (1+\cos\theta_B)/2 & (\cos\theta_B - 1)/2 & -\sin\theta_B/\sqrt{2} \\ (\cos\theta_B - 1)/2 & (1+\cos\theta_B)/2 & -\sin\theta_B/\sqrt{2} \\ \sin\theta_B/\sqrt{2} & \sin\theta_B/\sqrt{2} & \cos\theta_B \end{pmatrix}, \tag{6.29}$$

where θ_B is the angle between $\vec{B}$ and $\vec{k}$, $\cos\theta_B = B_z/B$. The matrix representation $\left[\overleftrightarrow{\chi}\right]$ of $\overleftrightarrow{\chi}$ in the $(\vec{e}_\pm, \vec{e}_3)$ basis is thus given by

$$\left[\overleftrightarrow{\chi}\right] = A^{-1}\left[\overleftrightarrow{\chi}\right]' A. \tag{6.30}$$

Combining Eqs. (6.22), (6.26), (6.29), and (6.30), the equation for the propagation of the electric field amplitude $\vec{E}_0$ can now be written in the form of the following set of coupled differential equations:

$$\begin{aligned}\partial E_{0+}/\partial z &= (ik/8)\{[\chi_+(1+\cos\theta_B)^2 + \chi_-(1-\cos\theta_B)^2 + 2\chi_z\sin^2\theta_B]\,E_{0+} \\ &\quad +(2\chi_z - \chi_+ - \chi_-)\sin^2\theta_B\,E_{0-}\} \\ \partial E_{0-}/\partial z &= (ik/8)\{(2\chi_z - \chi_+ - \chi_-)\sin^2\theta_B\,E_{0+} \\ &\quad +[\chi_+(1-\cos\theta_B)^2 + \chi_-(1+\cos\theta_B)^2 + 2\chi_z\sin^2\theta_B]\,E_{0-}\}.\end{aligned} \tag{6.31}$$

For $\theta_B = 0$ ($\vec{B} \parallel \vec{k}$) the equations are decoupled and χ_z drops out of the equations, or, in other words, the π lines do not contribute to the propagation of the light:

$$\frac{\partial E_{0\pm}}{\partial z} = \frac{ik}{2}\chi_\pm\,E_{0\pm}. \tag{6.32}$$

In our system this is the case on the symmetry axis of the trap. For $\theta_B = \pi/2$ ($\vec{B}\perp\vec{k}$) the equations are also reduced to a simple decoupled form when written in the linear polarization basis:

$$\begin{aligned}\partial E_{01}/\partial z &= (ik/2)\chi_z\,E_{01} \\ \partial E_{02}/\partial z &= (ik/4)(\chi_+ + \chi_-)\,E_{02}.\end{aligned} \tag{6.33}$$

For other angles there is no B-independent polarization basis in which Eqs. (6.31) decouple.

To a very good approximation our trapping field has quadrupolar symmetry (see Chapter 2):

$$\begin{aligned}B_\rho(\rho,\phi) &= \alpha\rho\sin 2\phi \\ B_\phi(\rho,\phi) &= \alpha\rho\cos 2\phi,\end{aligned} \tag{6.34}$$

where ρ is the radial distance from the z-axis, ϕ the azimuthal angle (see Fig. 2.4), B_ρ and B_ϕ are the corresponding field components, and $\alpha = 2.2\,\mathrm{T/cm}$ in the magnetic field configurations used. The magnitude of the field is independent of ϕ.

Consider a light beam with an axially symmetric intensity distribution but arbitrary polarization which enters the cell along the z-axis and is partially absorbed by the trapped gas. Obviously, the intensity distribution on the detector surface will have the same two-fold symmetry as the field. Suppose that for a fixed value of ρ and $\phi = 0$ the initial electric field amplitude is given by $\vec{E}_0 = E_{0+}\vec{e}_+ + E_{0-}\vec{e}_-$.

Furthermore, the E_{0+} component gives rise to a field amplitude $E_{++}\vec{e}_+ + E_{+-}\vec{e}_-$ on the photodiode surface and the E_{0-} component to a field amplitude $E_{-+}\vec{e}_+ + E_{--}\vec{e}_-$. Using the quadrupolar symmetry of the field and the definition (6.24) it is straightforward to derive that the intensity I_d on the detector surface for an arbitrary angle ϕ can be written as

$$\begin{aligned} I_d &= (\epsilon_0 c/2)\,[|E_{++}|^2 + |E_{+-}|^2 + |E_{-+}|^2 + |E_{--}|^2 \\ &\quad + \mathrm{Re}(E_{++}E^*_{-+} + E_{--}E^*_{+-})\cos 2\phi]. \end{aligned} \tag{6.35}$$

Thus, the intensity distribution on the detector surface can be completely determined by integrating Eq. (6.31) for a single value of ϕ. Since the photodiode has a square shape, centered on the z-axis, and hence four-fold symmetry, the ϕ-dependent term in Eq. (6.35) averages to zero in the measurement process. The observed signal is proportional to the sum of the average intensities associated with the separate circular polarization components, independent of their relative phase. This is a very useful property in view of the fact that the polarization and the precise intensity distribution of the L_α beam entering the cell are unknown and have to be inferred from the spectra.

Summarizing: Consider a sample of trapped H↑, characterized by a specific field configuration, particle number, and temperature. Assuming that the L_α beam entering the experimental cell has an axially symmetric intensity distribution, Eq. (6.31) has to be integrated for one value of the azimuthal angle ϕ and for the range of values of the radial distance ρ which lie within the sensitive area of the photodiode, separately for left and right-circularly polarized light. The information thus obtained enables straightforward calculation of transmission spectra for light beams with arbitrary polarization and arbitrary intensity distribution.

6.4.3 Bandwidth of the Lyman-α source

The transmission spectra which are calculated using the above recipe can only be obtained by scanning the frequency of a monochromatic L_α source. For comparison with experimental spectra the theoretical spectra are convoluted with a Lorentzian lineshape function with a 100 MHz FWHM linewidth, thus accounting for the finite bandwidth of our L_α source.

6.5 Transmission spectroscopy

In this section several examples are shown of experimental transmission spectra and a qualitative interpretation of the general features is discussed. Theoretical fits to

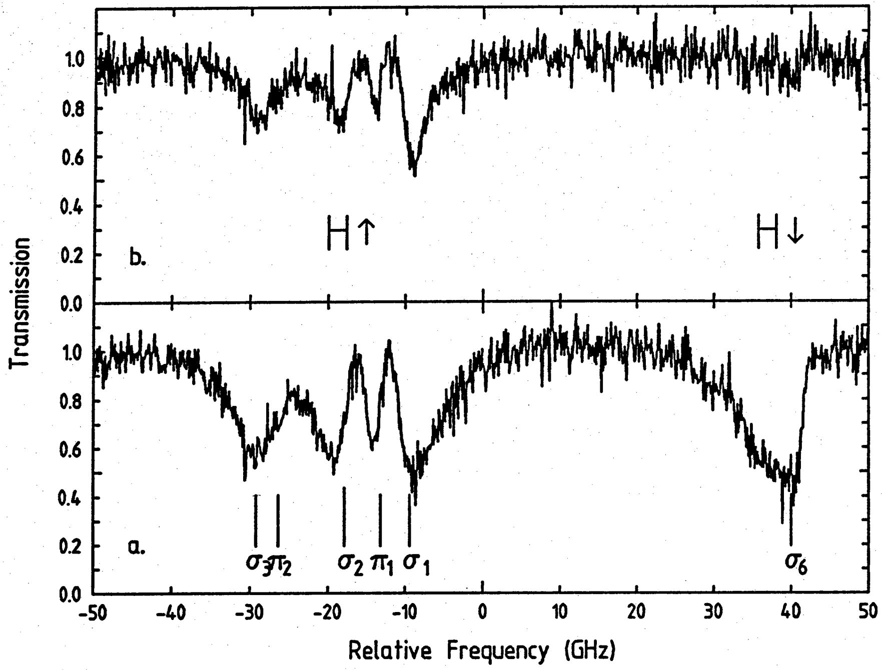

Figure 6.5: Transmission spectra recorded before (a) and after (b) removal of high-field seeking H↓ atoms.

some spectra are presented, which allow the determination of the temperature and the central density.

6.5.1 First optical evidence of trapping

In Fig. 6.5 two of the first recorded transmission spectra of trapped H↑ gas are shown. The spectra were recorded in a trapping field with a minimum $B_0 = 0.2\,\mathrm{T}$ with the H↑ gas in thermal equilibrium with the cell walls at $T \approx 0.2\,\mathrm{K}$. With the help of Fig. 6.2 the multiplet on the low frequency side may be identified with the H↑ transitions σ_1, σ_2, σ_3, π_1, and π_2. The σ_3 and π_2 lines overlap and cannot be distinguished separately. The asymmetric line shapes reflect the distribution of particles in the trapping field. The steep edge on the low frequency side of the σ_1 line, for instance, roughly corresponds with the field at the minimum, while the blue wing is due to absorption by atoms in higher fields, consistent with the positive sign of the Zeeman shift. The amount of inhomogeneous Zeeman broadening is directly related to the temperature of the gas: A temperature of $T = 0.2\,\mathrm{K}$ means the trapped particles are spread out over a magnetic field range of, roughly, $\Delta B \sim k_B T/\mu_B = 0.3\,\mathrm{T}$, which corresponds for the σ_1 transition to a frequency range $\Delta\nu = \mu_B \Delta B/h \sim k_B T/h = 4.2\,\mathrm{GHz}$. At this temperature the inhomogeneous Zeeman broadening is dominant: the natural linewidth is $\Gamma/2\pi = 0.1\,\mathrm{GHz}$ and the Doppler linewidth (FWHM) $\Delta\nu_D/\sqrt{T} = 1.76\,\mathrm{GHz\,K^{-1/2}}$ (see Sect. 6.3.4). The σ_2, σ_3, and π_2 transitions have negative Zeeman shifts and are consequently asymmetrically broadened to lower frequencies. The π_1 line displays no appreciable asymmetric broadening due to its small Zeeman shift.

In Fig. 6.5(a) an extra asymmetrically broadened line is present at high frequencies, whose steep edge coincides with the H↓ σ_6 transition in a field of $\sim 4.5\,\mathrm{T}$. This line is due to absorption by high-field seeking H↓ atoms, which are caught in the field maximum ($\sim 4.5\,\mathrm{T}$) of the dissociator coil "up-stream" in the light path of the L_α beam (see Fig. 4.2). The σ_6 line is inhomogeneously broadened to lower frequencies, in accordance with the positive sign of the Zeeman shift. The broadening of the σ_6 line is larger than that of, for instance, the σ_1 line because the H↓ atoms are in thermal equilibrium with a hotter part of the cell ($T \approx 0.4\,\mathrm{K}$). On the basis of Figs. 6.2 and 6.3 one would also expect a π_4 line in the middle of the H↑ multiplet; π transitions, however, cannot be excited in the high-field region, since $\vec{B}$ is strictly parallel to $\vec{k}$ at the heart of the dissociator coil. In Fig. 6.5(b) a spectrum is shown recorded immediately after triggering of the high-field bolometer, which very effectively removes the H↓ atoms by recombination on a local helium-free surface in the high-field region. The fact that the H↓ line has disappeared while the H↑ lines are still there, is clear evidence of trapping of H↑ in the field minimum.

In later measurements we were able to improve the signal-to-noise ratio of the transmission spectra significantly, allowing us to extract reliable quantitative information on the trapped samples using the exact theory described in Sect. 6.4.

6.5.2 Line shapes, absorption peaks, and density of states

Before going into a detailed comparison of the exact theory of Sect. 6.4 with the experimental spectra, we will dwell on a simplified description of the extinction of the light beam which provides a qualitative insight into the shape of the absorption lines, e.g. the difference between the H↑ lines and the H↓ line (Fig. 6.5). In addition it allows us to make approximate quantitative statements about the relation between the position of the absorption peaks and the temperature of the trapped gas.

Simplified picture. If we neglect the vector character of the light and dispersive effects, the extinction of a light beam of frequency ω and having an axially symmetric intensity distribution is described by

$$\frac{\partial I(\omega,\rho,z)}{\partial z} = -n(\rho,z)\,\sigma(\omega,\rho,z)\,I(\omega,\rho,z), \tag{6.36}$$

where I is the light intensity, $n(\rho,z) = n_0 \exp[-\mu_B B(\rho,z)/k_B T]$ is the gas density at position (ρ,z), and σ the absorption cross section. Restricting ourselves to a single optical transition with a linear Zeeman shift, the cross section may be written as $\sigma = \sigma_0(B)\,F_V(\omega-\omega_Z)$, where the resonant cross section σ_0 is only weakly field dependent, F_V is the Voigt line shape function, and $\omega_Z = \omega_0 + \alpha_Z B$ is the Zeeman shifted resonant frequency. The Voigt line has a width $\Delta\omega_V$, which depends on the natural linewidth Γ and the temperature T. For temperatures $T \gg 9\,\mathrm{mK}$ the Voigt linewidth $\Delta\omega_V$ is approximately equal to the Doppler linewidth (FWHM $\Delta\nu_D/\sqrt{T} = 1.76\,\mathrm{GHz\,K^{-1/2}}$).

Resonant absorption shells. In this simplified picture the absorption of light of a certain frequency ω only depends on the local field strength B. The relative absorption $I^{-1}(\partial I/\partial z)$ is largest on the magnetic field contour (equipotential surface) for which the extinction length $\ell_{ext} = [n(B)\sigma(\omega,B)]^{-1}$ is minimal as a function of B. If we only consider temperatures for which $k_B T \gg \hbar\Delta\omega_V$ ($k_B T \gg 8\ln 2(\hbar k)^2/m$, $T \gg 7\,\mathrm{mK}$), then the density is a much more slowly varying function of B than the cross section. To illustrate this, suppose light of a frequency ω is absorbed on the σ_1 transition, in which case $\alpha_Z = \mu_B/\hbar$. The Voigt absorption linewidth corresponds to a magnetic field range $\Delta B_V \approx \hbar\Delta\omega_V/\mu_B$. Using $\Delta\nu_V/\sqrt{T} = 1.76\,\mathrm{GHz\,K^{-1/2}}$ we have $\Delta B_V/\sqrt{T} \approx 0.13\,\mathrm{T\,K^{-1/2}}$. This means that for $T = 0.1\,\mathrm{K}$, for example, the light is resonant with σ_1 over a field range $\Delta B_V \approx 0.04\,\mathrm{T}$. The relative change in gas density over the field range ΔB_V is $|n^{-1}(\partial n/\partial B)\Delta B_V| = 0.084\,(T/\mathrm{K})^{-1/2}$, which is always small for the temperatures under consideration. Consequently, the value of B for which ℓ_{ext} is minimal is approximately equal to the value for which $\sigma(\omega,B)$ reaches a maximum, i.e., for $B = B_{res}(\omega)$, where $B_{res}(\omega)$ is defined by

$$\omega_Z(B_{res}(\omega)) \equiv \omega. \tag{6.37}$$

As a result, at densities which are so low that the sample is optically thin, most of the absorption of light of a frequency ω takes place in a thin shell, with a thickness corresponding to a field range $\Delta B_V \approx \alpha_Z^{-1}\Delta\omega_V$, which encloses the "resonant" magnetic field contour $B = B_{res}(\omega)$. (Actually, the above argument does not hold for frequencies ω with a large detuning with respect to the minimum, $\Delta\omega = \omega - \omega_Z(B_0) \gg \alpha_Z k_B T/\mu_B$; these frequencies, however, only contribute to the far wings of the absorption lines and are not important for this discussion.)

The picture of resonantly absorbing shells breaks down at high densities, when the outer layers of the gas cloud become optically thick even for non-resonant frequencies. In order to make somewhat more specific statements we introduce two convenient length scales: ℓ_V, the Voigt length, and ℓ_{re}, the resonant extinction length.

Voigt length and resonant extinction length. The Voigt length is the thickness of the resonant shell in the direction of the light propagation:

$$\ell_V \equiv (\partial B/\partial z)^{-1}\Delta B_V. \tag{6.38}$$

On the z-axis ($\rho = 0$) B depends approximately quadratically on z, $B(0,z) \approx B_0 + \beta(z - z_0)^2$, where typically $\beta = 0.023\,\mathrm{T/cm^2}$. One can easily derive that the axial Voigt length is then given by

$$\ell_V^{ax}(\omega) = \Delta B_V/2\beta(z - z_0) = \Delta B_V/2\sqrt{\beta[B_{res}(\omega) - B_0)}. \tag{6.39}$$

For a given temperature a typical axial Voigt length is obtained by substituting $z - z_0 = \ell_{eff}/2$ in Eq. (6.39), where ℓ_{eff} is the effective axial length of the sample (see Sect. 3.2.4). For the temperatures we are considering ($T \gg 7\,\mathrm{mK}$) we find a typical axial Voigt length

$$\ell_V^{ax,typ} = \hbar k\sqrt{\frac{8\ln 2}{m\mu_B\beta}} \approx 5.5\,\mathrm{mm}, \tag{6.40}$$

independent of the temperature.

In the $z = z_0$ plane B is approximately proportional to the radial distance ρ for $B - B_0 > B_0$: $B(\rho, z_0) \approx \alpha\rho$, where typically $\alpha = 2.2\,\mathrm{T/cm}$. The radial shell thickness is then approximately independent of the field:

$$\ell_V^{rad} \approx \Delta B_V/\alpha. \tag{6.41}$$

For example, for the σ_1 transition the radial shell thickness $\ell_V^{rad} \approx 0.2\,\mathrm{mm}$ at $T = 0.1\,\mathrm{K}$, 25× smaller than the axial thickness. In Fig. 6.6 the absorption shell around $B_{res} = 0.1\,\mathrm{T}$ is plotted for $T = 0.1\,\mathrm{K}$, in a field $B(\rho, z) = \sqrt{(B_0 + \beta z^2)^2 + \alpha^2\rho^2}$, with $B_0 = 0.1\,\mathrm{T}$, $\alpha = 2.2\,\mathrm{T/cm}$, and $\beta = 0.023\,\mathrm{T/cm^2}$.

The resonant extinction length is the extinction length at the center of the resonant absorption shell:

$$\ell_{re}(\omega) \equiv [n(B_{res}(\omega))\,\sigma(\omega, B_{res}(\omega))]^{-1}. \tag{6.42}$$

For example, for the σ_1 transition at a temperature $T = 0.1\,\mathrm{K}$ and a local density $n = 10^{11}\,\mathrm{cm^{-3}}$, the resonant extinction length $\ell_{re} \approx 5\,\mathrm{mm}$.

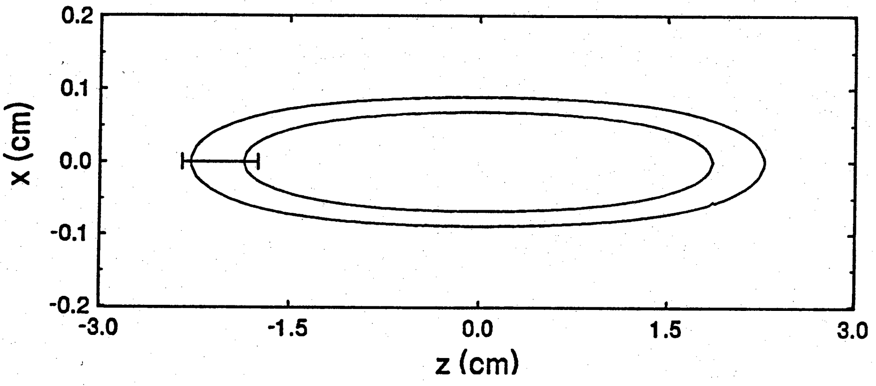

Figure 6.6: Resonant absorption shell around the contour $B_{res} = 0.2\,\mathrm{T}$ at $T = 0.1\,\mathrm{K}$. Note the difference in scales in the axial (z) and the radial (x) direction. The horizontal bar indicates the resonant extinction length for $B = B_{res}$, $T = 0.1\,\mathrm{K}$, and $n_0 = 2 \times 10^{11}\,\mathrm{cm}^{-3}$.

Clearly, if $\ell_{re}(\omega) \gg \ell_V$, then the sample is optically thin at the frequency ω and the maximum absorption occurs in the resonant absorption shell around the field contour $B = B_{res}(\omega)$. If $\ell_{re}(\omega) \ll \ell_V$, then the sample is optically thick and most of the light is absorbed before it reaches the resonant absorption shell. Since the shell thickness ℓ_V is much smaller in the radial direction than in the axial direction, the sample is in many cases optically thick axially, but optically thin radially (see Fig. 6.6).

Low densities. Let us first consider the case that $\ell_{re} \gg \ell_V$ for all frequencies. Maximum absorption in the spectrum then occurs at the resonant frequency $\omega = \omega_Z(B)$ which corresponds to the magnetic field contour of the absorption shell with the largest number of particles, i.e., corresponding to a value $B = B_p$ for which the function $\rho_M(B)\exp(-\mu_B B/k_B T)$ has a maximum. Here $\rho_M(B)$ is the magnetic density of states as defined in Chapter 3 (Sect. 3.2), which can be approximated quite well near the minimum by

$$\rho_M(B) = \frac{4\pi}{\alpha^2\sqrt{\beta}}[(B - B_0)^{3/2} + B_0(B - B_0)^{1/2}]. \qquad (6.43)$$

In this approximation of the trapping field the value of B_p only depends on B_0 and T and can be calculated easily. It is then also possible to express T in terms of B_0 and B_p:

$$T = \frac{\mu_B B_p}{k_B}\frac{B_p - B_0}{3B_p/2 - B_0}, \qquad (6.44)$$

which is very useful, as it allows us to make a quick estimate of the temperature of the trapped gas on the basis of the positions of the absorption peaks. This is illustrated

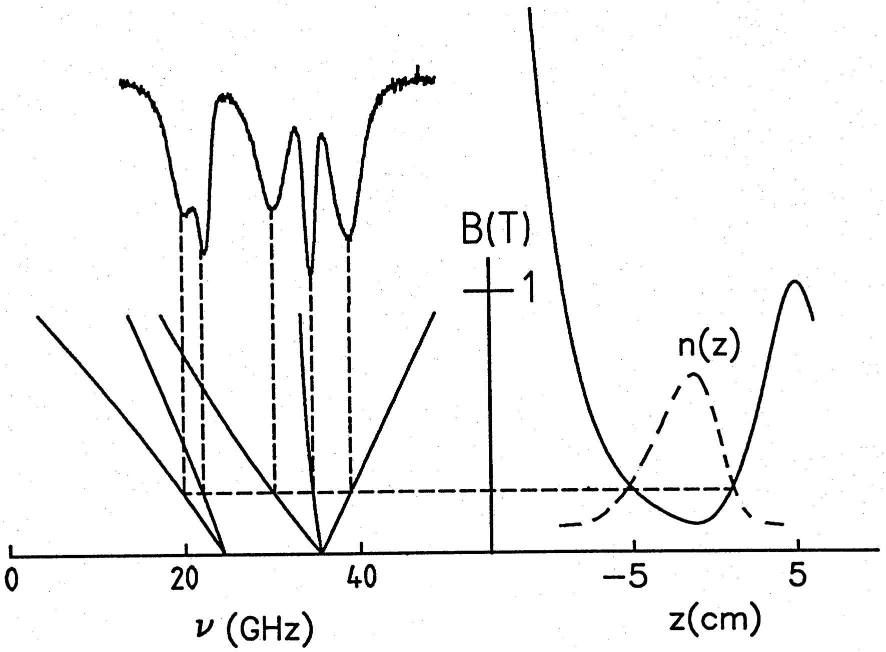

Figure 6.7: Transmission spectrum recorded with linearly polarized light (left) and axial magnetic field profile with density distribution (right). It is indicated via the Zeeman diagram how all five absorption peaks correspond to a single value of the magnetic field.

in Fig. 6.7. On the right hand side the axial magnetic field and the axial density distribution are plotted as a function of z. On the left hand side a transmission spectrum is shown, recorded with linearly polarized light, and the Zeeman diagram of the five H↑ fine structure transitions. The figure gives a clear intuitive picture of how the main features of the spectrum arise from the summation over the trapping region of density weighed, Zeeman shifted fine structure lines. The asymmetric line shapes reflect the signs and the magnitudes of the Zeeman shifts. The five absorption peaks all agree with $B_p = 0.23\,\mathrm{T}$, which suggests, using Eq. (6.44) and $B_0 = 0.1\,\mathrm{K}$, a gas temperature $T = 81\,\mathrm{mK}$. The density distribution plotted corresponds to $T = 81\,\mathrm{mK}$.

This approximate method of determining the temperature of the trapped gas can only be applied in a limited range of temperature and density. The picture of resonantly absorbing shells breaks down at high densities ($\ell_{re} \ll \ell_V$), when the outer layers of the gas cloud become optically thick even for non resonant frequencies, and for low temperatures $k_B T \lesssim \hbar\Gamma$, when the thickness of the absorption shells becomes comparable to the sample size.

One-dimensional picture. Using similar density of states arguments we can also understand the difference between the shapes of the H↑ lines and the H↓ line in Fig. 6.5. The H↓ atoms, caught in the field maximum, are magnetically trapped in the z-direction but are free to move radially, in which direction they are only confined by the inner surface of the surrounding light tube. Since B only depends on z, Eq. (6.36) can be written in the form

$$\frac{\partial I}{\partial B} = (\frac{\partial B}{\partial z})^{-1} n\,\sigma\,I, \tag{6.45}$$

so maximum absorption occurs in regions where $\partial B/\partial z = 0$, i.e., at positions where the one-dimensional magnetic density of states diverges. For the high-field region this means the absorption of light peaks at the resonant frequency corresponding to the field maximum at $B = 4.5\,\mathrm{T}$. Since there are no atoms residing in higher fields this is also the frequency where the line is cut off, as is demonstrated in Fig. 6.5. The sharp edge is a clear indication of one-dimensional absorption. The explanation of the shape of the spectra in terms of one-dimensional density of states arguments was also used by Helmerson *et al.* in their experiments with magnetically trapped Na atoms [11].

High densities. In Fig. 6.8 a transmission spectrum is shown which was recorded with left-circularly polarized light and at a relatively high temperature and density ($T \approx 0.2\,\mathrm{K}$ and $n_0 > 10^{13}\,\mathrm{cm}^{-3}$). Since the z-component of the magnetic field in our trap is pointing everywhere in the direction of the light beam, the excitation of σ^- transitions σ_2 and σ_3 is strongly suppressed. The magnetic field configuration used was the "short" geometry (Chapter 2, Fig. 2.7), which has a shallow secondary field minimum at $z = -7.4\,\mathrm{cm}$, as can be seen in the upper part of the figure, where the resonant frequencies of three transitions are plotted as a function of the position on the axis. The absolute field minimum has a value $B_0 = 0.1\,\mathrm{T}$, while the secondary minimum is at $B_1 = 1.4\,\mathrm{T}$. The magnetic barrier in between peaks at $B = 1.7\,\mathrm{T}$.

Because of the high density and temperature, or, in other words, the large number of trapped particles, the sample is almost completely opaque for an appreciable spectral range due to absorption on the σ_1 resonance. The σ_1 line is strongly broadened and it is no longer possible to define a single frequency of maximum absorption. A striking feature of the spectrum is the structure around $\nu = 40\,\mathrm{GHz}$ which is due to absorption on the σ_1 transition by H↑ atoms trapped in the secondary minimum. The structure displays two peaks which can again be explained by similar density of states arguments as used above. Notice that the local field *maximum* at $z \approx -5\,\mathrm{cm}$ gives rise to enhanced absorption as well. These "satellites" of the main σ_1 line only

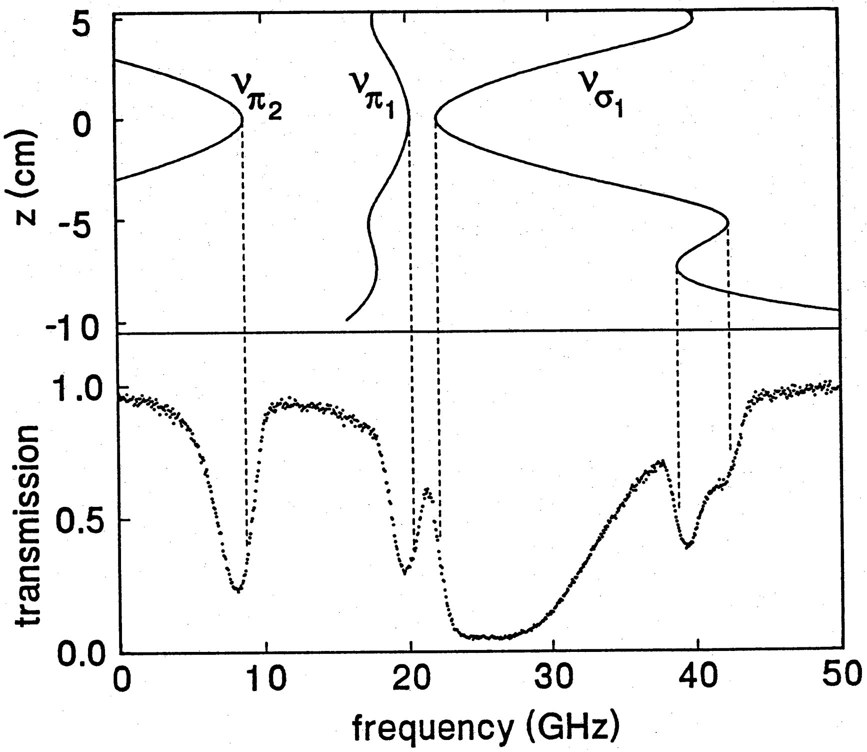

Figure 6.8: Lower part: Transmission spectrum recorded with left-circularly polarized light. Upper part: Resonant frequencies of the σ_1, π_1, and π_2 transitions as a function of z, on the axis.

appear at relatively high densities and/or temperatures since the density n_1 in the secondary minimum is strongly suppressed with respect to the central density n_0: $n_1 = n_0 \exp[-\mu_B(B_1 - B_0)/k_B T]$.

6.5.3 Diagnostics of the trapped gas

A reliable determination of the temperature and the density of the trapped gas requires careful fitting of the parameters that enter into the exact theory described in Sect. 6.4.2 to all the details of an entire transmission spectrum. In Fig. 6.9 two examples of fits are shown. The two spectra were taken on the same sample, shortly after each other, one with right- and one with left-circularly polarized light. The field configuration used was the "long" geometry (Fig. 6.4), which has a single minimum at $B_0 = 0.1\,\mathrm{T}$. The scan time for each spectrum was 30 s, which is approximately the

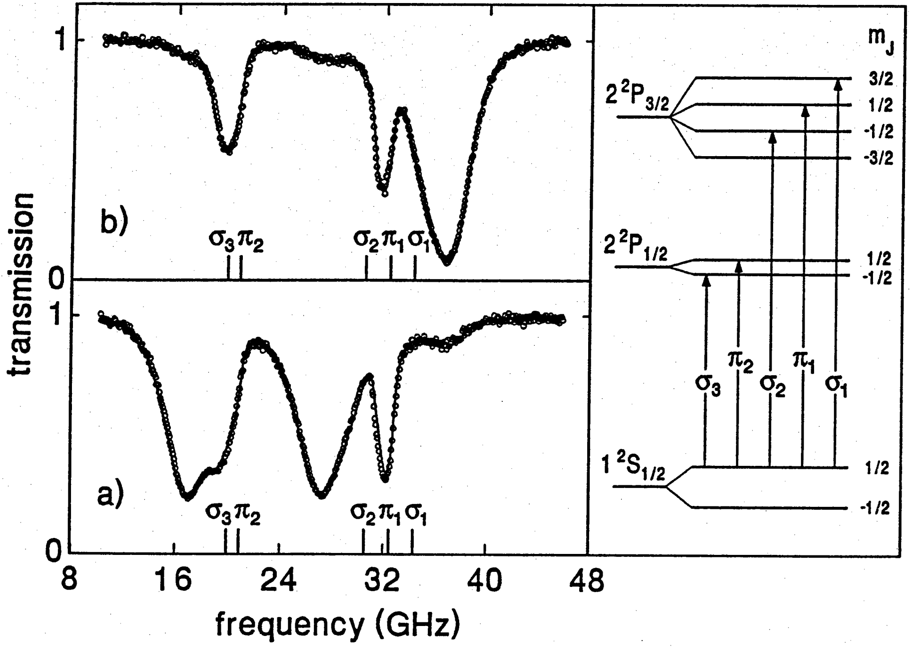

Figure 6.9: Transmission spectra, recorded with (a) right and (b) left-circularly polarized light, and energy level diagram defining the five allowed transitions. The solid lines are calculated spectra for $T = 51(12)\,\mathrm{mK}$ and (a) $n_0 = 4.4(1.0) \times 10^{12}\,\mathrm{cm}^{-3}$ and (b) $n_0 = 3.3(0.8) \times 10^{12}\,\mathrm{cm}^{-3}$. The vertical bars denote the resonant frequencies of the five allowed transitions for $B = B_0$.

maximum allowable time for gas densities $\sim 10^{12}\,\mathrm{cm}^{-3}$ for taking spectra with the aim of determining the temperature and the density of the trapped gas. Longer scan times lead to non-negligible particle loss during the scan, either through intrinsic loss mechanisms or through spurious optical pumping to H$\downarrow$ states. A scan time of 30 s, however, is sufficiently long to achieve a satisfactory signal-to-noise ratio, as is clear from Fig. 6.9.

In the fitting procedure there are five free fitting parameters: the central density n_0, the fraction of atoms in the c state, the temperature of the trapped gas T, the helicity of the light polarization, and the radial intensity distribution of the light beam. The presence of hyperfine structure in the spectra, due to c state atoms, becomes manifest only at $T \lesssim 10\,\mathrm{mK}$ and does not play any role of importance in the spectra described in this thesis. With the remaining four fitting parameters it is possible to obtain very good agreement between the experimental spectra and the theory of Sect. 6.4, as is shown in Fig. 6.9. We find for both spectra a temperature $T = 51(12)\,\mathrm{mK}$, while for the spectrum first taken (a) $n_0 = 4.4(1.0)\times10^{12}\,\mathrm{cm}^{-3}$, and for the second spectrum (b) $n_0 = 3.3(0.8) \times 10^{12}\,\mathrm{cm}^{-3}$. The calculated spectra are quite sensitive to the choice of the magnetic field $\vec{B}(\vec{r})$, especially to the value of the field minimum B_0. We use for the calculation of $\vec{B}(\vec{r})$ the expressions of chapter 2 and it turns out it is not possible to attain the same high quality fits (with other values of T and n_0) in a deviating field. The accuracy of the determination of T and n_0 depends on the conditions but is typically $\sim$ 25%, limited predominantly by imprecise knowledge of the beam shape. The reliability of the method would be greatly improved by an independent determination of the L_α beam shape.

The spectra shown in Fig. 6.9 exhibit several interesting features which will be discussed in Sect. 6.5.4.

6.5.4 Polarization and dispersion effects

Polarization effects. In our experimental arrangement the wave vector $\vec{k}$ of the light near the z-axis always points in the same direction as the z-component of the magnetic field vector, so left-circularly polarized light mainly excites σ^+ transitions while right-circularly polarized light mainly excites σ^- transitions. However, there is clearly a σ_1 contribution present in the spectrum of Fig. 6.9(a) and some traces of absorption on the σ^- transitions σ_2 and σ_3 in the spectrum of Fig. 6.9(b). This is not due to incomplete polarization of the light, but to the finite angle θ_B between $\vec{k}$ and $\vec{B}$ (off axis), as is immediately clear from Eq. (6.31): If $\theta_B \neq 0$ the component E_{0-} is also absorbed on σ^+ transitions and the component E_{0+} on σ^- transitions. Then, the projection of the oscillating electric field vector of a purely circularly polarized light beam on a plane $\perp \vec{B}$ is elliptical, and thus also contains a circular component with opposite helicity.

Absorption enhanced by optical activity. Circularly polarized light can be written as the sum of two perpendicular, phase shifted linearly polarized components of equal amplitude. Since π resonances only affect the linearly polarized component parallel to the transverse component of $\vec{B}$ with respect to the z-axis, $\vec{B}_\perp \equiv \vec{B}-(\vec{B}\cdot\vec{e}_z)\vec{e}_z$, one would expect that π-absorption of circularly polarized light cannot exceed 50%, and thus, using the arguments of Sect. 6.4, neither can π-absorption of arbitrarily polarized light in a quadrupolar field. In the spectra of Figs. 6.8 and 6.9, however, we observe that the maximum absorption on the π lines can be substantially higher than 50%. The extra absorption is too strong to be attributed to the far wings of σ lines. To explain the origin of this feature Eq. (6.31) is rewritten in the linear polarization basis, defined by the local orientation of the magnetic field (see Eqs. (6.24) and (6.25)):

$$\begin{aligned}\partial E_{01}/\partial z &= (ik/4)\{[(\chi_+ + \chi_-)\cos^2\theta_B + 2\chi_z \sin^2\theta_B]E_{01} \\ &\quad -i(\chi_+ - \chi_-)\cos\theta_B E_{02}\} \\ \partial E_{02}/\partial z &= (ik/4)\{(\chi_+ + \chi_-)E_{02} + i(\chi_+ - \chi_-)\cos\theta_B E_{01}\}.\end{aligned} \tag{6.46}$$

In this basis $\vec{e}_1$ is by definition parallel to $\vec{B}_\perp$, so only the component E_{01} is directly absorbed on π transitions. However, the equations are coupled so the component E_{02} is also affected - indirectly - by the π transition. Suppose, for instance, that π-absorption has reduced E_{01} to zero for some value of z. If the frequency is tuned between a σ^+ and a σ^- resonance in such a way that linearly polarized light is equally absorbed on both transitions, i.e., $\mathrm{Im}\chi_+ = \mathrm{Im}\chi_-$ and thus $\mathrm{Re}\chi_+ = -\mathrm{Re}\chi_-$, then the Eqs. (6.46) are coupled by a real coefficient $(k/4)(\chi_+ - \chi_-)\cos\theta_B$. Consequently, the amplitude E_{01} will grow in phase with the existing component E_{02}, which means the total polarization vector $\vec{E}_0 = E_{01}\vec{e}_1 + E_{02}\vec{e}_2$, initially linear, remains linear but starts rotating in the $(\vec{e}_1, \vec{e}_2)$-plane (= xy-plane). In this way the polarization, initially perpendicular to $\vec{B}_\perp$, will acquire a linear component parallel to the transverse component of $\vec{B}$ and will be absorbed subsequently on the π transition.

The continuous rotation of the linear polarization in the xy-plane is called Faraday rotation. There is only pure Faraday rotation if $\mathrm{Im}\chi_+ = \mathrm{Im}\chi_-$. At other frequencies the polarization will in general be elliptical, with the eccentricity and the orientation of the principal axes of the ellips continuously changing as a function of z.

Due to Faraday rotation both initial linear polarization components E_{01} *and* E_{02} will be absorbed on π transitions. Therefore, at high densities more than 50% of the light can be absorbed on a π line. The strengths of the π_1 line in Fig. 6.9(a) and of the π_2 line in Fig. 6.8 cannot be attributed to absorption in the wings of nearby σ lines and thus are clear evidence of strong optical activity of the trapped sample.

Absorption-induced line shift. Close inspection of the spectra shown in Fig. 6.9 reveals another subtle feature, namely, the frequency for maximum absorption of the π_1 line is different for left- and right-circularly polarized light. The π_1 line seems to be repelled by σ lines: For left-circularly polarized light the σ_1 line is strongest and the π_1 line is shifted to the red, while for right-circularly polarized light the σ_2 line is strongest and the π_1 line is shifted to the blue. The fact that in both cases the π_1 line is on the slope of a strong σ line suggests shifts in opposite directions. This phenomenon can be traced back to the imaginary part of the coupling coefficient $(k/4)(\chi_+ - \chi_-)\cos\theta_B$ in Eq. (6.46). Suppose at $z = 0$ we have left-circularly polarized light $\vec{E}_0 = E_{10}(0)(\vec{e}_1 + i\vec{e}_2)$ (linear components $E_{01}(0)$

and $E_{02}(0) = iE_{01}(0)$). For small z the coupling term in Eq. (6.46) will give rise to a change of E_{01} according to

$$(\frac{\partial E_{01}}{\partial z})_{coupling} \approx \frac{ik}{4}(\chi_+ - \chi_-)\cos\theta_B \, E_{01}(0), \tag{6.47}$$

so E_{01} will increase if $\mathrm{Im}(\chi_+ - \chi_-) < 0$ and E_{01} will decrease if $\mathrm{Im}(\chi_+ - \chi_-) > 0$: σ-absorption of the component E_{02} leads to the appearance of a linear component parallel to $\vec{e}_1$ which may be either in phase or in anti-phase with the already existing component E_{01}, depending on the sign of $\mathrm{Im}(\chi_+ - \chi_-)$. If σ^--absorption is dominant, i.e., if $\mathrm{Im}(\chi_+ - \chi_-) < 0$, the components are in phase, which means that part of the electric field component parallel to $\vec{e}_2$ is transformed into a linear component parallel to $\vec{e}_1$, which may be absorbed subsequently on the π transition. Hence π-absorption of left-circularly polarized light is enhanced if $\mathrm{Im}(\chi_+ - \chi_-) < 0$, which means the peak of the π_1 line will be shifted towards the σ_2 line, as is observed. Analogously, π-absorption of right-circularly polarized light is enhanced if $\mathrm{Im}(\chi_+ - \chi_-) < 0$, so in that case the π_1 line will be shifted towards the σ_1 line.

6.5.5 Deuterium

To date deuterium gas has defied attempts of trapping. Probably the main reason for this is the high binding energy of D on ℓ-^{4}He surfaces: $\epsilon_a/k_B \approx 2.6\,\mathrm{K}$ [12]. Actually we were able to show that if the experimental cell is heated up to $T_w \geq 0.4\,\mathrm{K}$, it is possible to produce D gas in our cryogenic dissociator and transport it subsequently to the trapping region. This is roughly consistent with the minimum temperature $T_w \approx 0.15\,\mathrm{K}$ required for loading the trap with H gas when the surfaces are covered with ℓ-^{4}He ($\epsilon_a/k_B = 1.00(5)\,\mathrm{K}$, see Chapter 3, Sect. 3.3). Unfortunately we were not able to trap D$\uparrow$, probably due to the high ^{4}He vapor density at $T_w = 0.4\,\mathrm{K}$.

One of the advantages of optical diagnostic techniques is the possibility to discriminate between H and D gas, in contrast with earlier, bolometric, methods [1, 2]: The transition frequencies of the L$_\alpha$ manifold in D are $\sim$ 770 GHz higher than the equivalent ones in H and therefore spectrally well separated. In Fig. 6.10 a D transmission spectrum is shown, recorded with the dissociator discharge continuously running and the cell heated up to $\sim 0.4\,\mathrm{K}$. It was necessary to keep the discharge running as the signal disappeared within a few seconds after the dissociator was turned off.

The trapping configuration used was the "short" geometry with $B_0 = 0.1\,\mathrm{T}$ (see Fig. 2.7). Using Fig. 6.2, the shape of the spectrum and the positions of the absorption peaks can be explained by assuming the cell was filled mainly with high-field seeking D$\downarrow$ atoms in thermal equilibrium with the cell walls. The descending

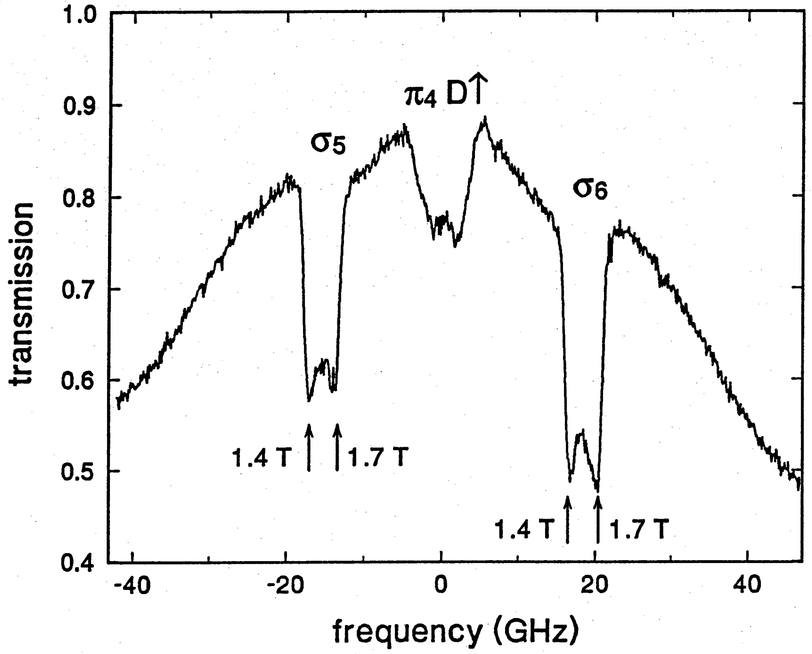

Figure 6.10: Deuterium transmission spectrum. Indicated are the absorption peaks due to D↓ and D↑ transitions. The frequency is given relative to $(E_{1D} - \Delta_D/6)/h$.

slope on the high frequency side ($\nu > 20$ GHz) is the red wing of the σ_6 line (compare Fig. 6.5), which peaks and is sharply cut off at $\nu \approx 60$ GHz, corresponding to the field maximum at $B = 4.5$ T. The rising slope on the low frequency side ($\nu < -20$ GHz) is, analogously, the blue wing of the σ_5 line, which peaks and is sharply cut off at $\nu \approx -57$ GHz. The two doubly peaked structures are satellites of the main σ_5 and σ_6 lines, with the peaks due to the local secondary minimum at $B = 1.4$ T and the nearby local maximum at $B = 1.7$ T (compare Fig. 6.8). The structure around $\nu = 0$ is due to absorption on both the π_4 transition and the D↑ transitions.

Although we did not succeed in trapping D↑, we have shown that it is possible in the present setup to produce D gas and transport it to the trapping region in sizeable quantities. This information may be useful for future attempts to trap D↑.

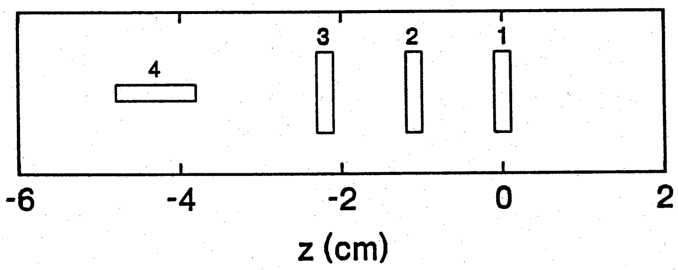

Figure 6.11: Orientations of the four bolometric fluorescence detectors on the cylindrical side wall.

6.6 Fluorescence spectroscopy

In addition to the photodiode we have four bolometric detectors at our disposal, which are mounted on the semi-cylindrical side wall of the detection unit, thus enabling angularly resolved fluorescence spectroscopy (see Fig.6.4). Each detector has a rectangular sensitive area, measuring 10 mm × 2 mm. The detectors are very thin, protruding negligibly into the sample volume, and they follow the curved inner surface of the cylindrical side wall. The orientations of the four detectors are schematically indicated in Fig. 6.11. The z-coordinates z_i of the centers are $z_1 = 0$, $z_2 = -10.8\,\mathrm{mm}$, $z_3 = -21.5\,\mathrm{mm}$, and $z_4 = -43.0\,\mathrm{mm}$. The lengths ℓ_i of the detectors in the z-direction are $\ell_1 = \ell_2 = \ell_3 = 2\,\mathrm{mm}$ and $\ell_4 = 10\,\mathrm{mm}$. The inner radius of the detection unit is $\rho_w = 6\,\mathrm{mm}$, so the azimuthal angles $\Delta\phi_i$ subtended by the detectors are $\Delta\phi_1 = \Delta\phi_2 = \Delta\phi_3 = 5/3$ and $\Delta\phi_4 = 1/3$. Construction details and the detection sensitivity of these devices are discussed in, respectively, Chapters 4 and 5.

In this thesis emphasis is put on the use of transmission spectroscopy as a diagnostic tool. Fluorescence spectroscopy yields in principle more information - the separate fluorescence detectors probe different parts of the trapped sample whereas in transmission spectroscopy a lot of the local details are smeared out - but the information is harder to analyze. Furthermore, the fluorescence meaurements in the experiments described in this thesis suffered from a rather poor signal-to-noise ratio compared to the transmission measurements. However, these noise problems are probably not of a fundamental nature (see Sect 5.5.2), and may be eliminated in future experiments. In this section we will discuss a simplified, preliminary analysis of some fluorescence spectra, based on the analysis of the corresponding transmission spectrum. This allows us to check the reliability and consistency of our diagnostic method and to estimate the detection sensitivity of the bolometric fluorescence detectors.

The calculation of the fluorescent radiation absorbed by a bolometric detector is more complicated than the calculation of the transmission of the sample. Using the equations of Sect. 6.4 we can keep track of the power absorbed from the L_α beam as a function of position. The subsequent spontaneous emission is not isotropic, but has an angular dependence which depends on the excited state and on both the local direction and magnitude of $\vec{B}$: For σ fluorescence, the probability per unit solid angle for emission of a photon with wave vector $\vec{k}$ is equal to $(3/16\pi)(1+\cos^2\theta_p)$, where θ_p is the angle between $\vec{k}$ and $\vec{B}$. The angular function for decay on a π transition is given by $(3/8\pi)\sin^2\theta_p$ [13]. The branching ratios determining the fraction of light released through σ-emission and the complementary fraction of π-emission depend on the excited state and $|\vec{B}|$ and can easily be calculated using Table 6.1 (see also Fig. 6.3). If multiple scattering effects are assumed to be negligible, the fluorescence reaching a particular detector from a small region in the sample is simply given by the spontaneous emission radiated within the solid angle subtended by that detector. Integration over the entire sample yields the total fluorescence incident on the detector. Due to the small solid angle subtended by the photodiode, less than 10^{-3} of the emitted fluorescence reaches the photo diode. The fluorescent intensity on the photodiode is therefore negligible with respect to the transmitted light intensity and introduces no error for the transmission measurements.

The justification of the single scattering assumption is in the fact that the thickness of the resonant absorption shells ℓ_V in the radial direction is much smaller than the resonant extinction length ℓ_{re}, under the relevant conditions (see Sect. 6.5.2). Consequently, the opacity for radially scattered light is fairly small, even under conditions of optical thickness of the sample core in the axial direction.

The above described procedure for calculating the fluorescence is straightforward but very time consuming. However, the calculation can be simplified considerably by the following approximations: First, we neglect the radial extent of the sample in the determination of the solid angle subtended by the detector, leaving only the dependence on z. This is of course a very good approximation at low temperatures. Second, we assume the spontaneous emission to be isotropic. For the σ_2, σ_3, π_1, and π_2 transitions this may be justified by the fact that the branching ratios for σ and π emission are comparable, in which case the anisotropy averages out, more or less. For the σ_1 transition this is not the case, since it forms a closed cycle and fluoresces therefore only through σ-emission. At temperatures $k_BT \gtrsim \mu_B B_0$ the anisotropy of the emission is also smeared out due to the fact that for each value of

z the orientation of $\vec{B}$ varies with the position in the xy-plane.

As a result of the two assumptions, we only have to keep track of the absorbed L$_\alpha$ power P_a as a function of z. The power P_i incident on detector i then simply follows from integrating the product of $P_a(z)$ and the detection solid angle over the length of the sample:

$$P_i = \int P_a(z)\,\frac{\Delta\phi_i}{4\pi}\left[\frac{z_i+\ell_i/2-z}{\sqrt{(z_i+\ell_i/2-z)^2+\rho_w^2}} - \frac{z_i-\ell_i/2-z}{\sqrt{(z_i-\ell_i/2-z)^2+\rho_w^2}}\right] dz. \qquad (6.48)$$

In Fig. 6.12 an example is shown of a transmission spectrum and the corresponding fluorescence spectra, recorded with detectors 1 and 4. The incident light beam was right-circularly polarized, as is clear from the near absence of the σ_1 line. First a fit to the transmission spectrum was obtained (see Fig. 6.12), using the theory of Sect. 6.4, which yielded $T = 46\,\mathrm{mK}$ and $n_0 = 6.9 \times 10^{11}\,\mathrm{cm}^{-3}$. The corresponding function $P_a(z)$ and Eq. (6.48) subsequently resulted in the fluorescence spectra indicated with solid lines in Fig. 6.12. The experimental fluorescence spectra were scaled to fit the theoretical spectra.

In view of the rather crude approximations used the result is very satisfactory. The main features of the fluorescence spectra are reproduced fairly well. Apparently our description gives a fully consistent description of both the transmission and the fluorescence spectra. We would like to stress that the frequency axis of the fluorescence spectra has not been scaled or shifted: the frequency dependence of the fluorescence signal is in good theoretical agreement with the transmission data. For both experimental fluorescence spectra approximately the same vertical scaling factor was used which implies that the bolometric detectors 1 and 4 have approximately equal detection sensitivities. The scaling factor obtained from this fit was used in Chapter 5 to compare the experimental bolometric detection sensitivity to the theoretically predicted value. Note that at most $\sim 0.5\%$ of the L$_\alpha$ flux entering the cell reaches the bolometers, indicating that, in spite of the rather poor signal-to-noise ratio, the absolute detection sensitivity of the bolometers is higher than that of the photodiode.

The fluorescence spectra are qualitatively different from the transmission spectra, displaying more sharply peaked structures. This arises from the fact that the bolometric detectors are more sensitive for the local absorption of the light, due to the strong z-dependence of the detection solid angle. The sensitivity for local absorption is also reflected by the fact that the absorption lines recorded by bolometer 4 are shifted to the red with respect to the corresponding lines recorded by bolometer 1: Bolometer 4 is sensitive to absorption in higher fields, which means that all fine structure lines, except the σ_1 line, are shifted to lower frequencies.

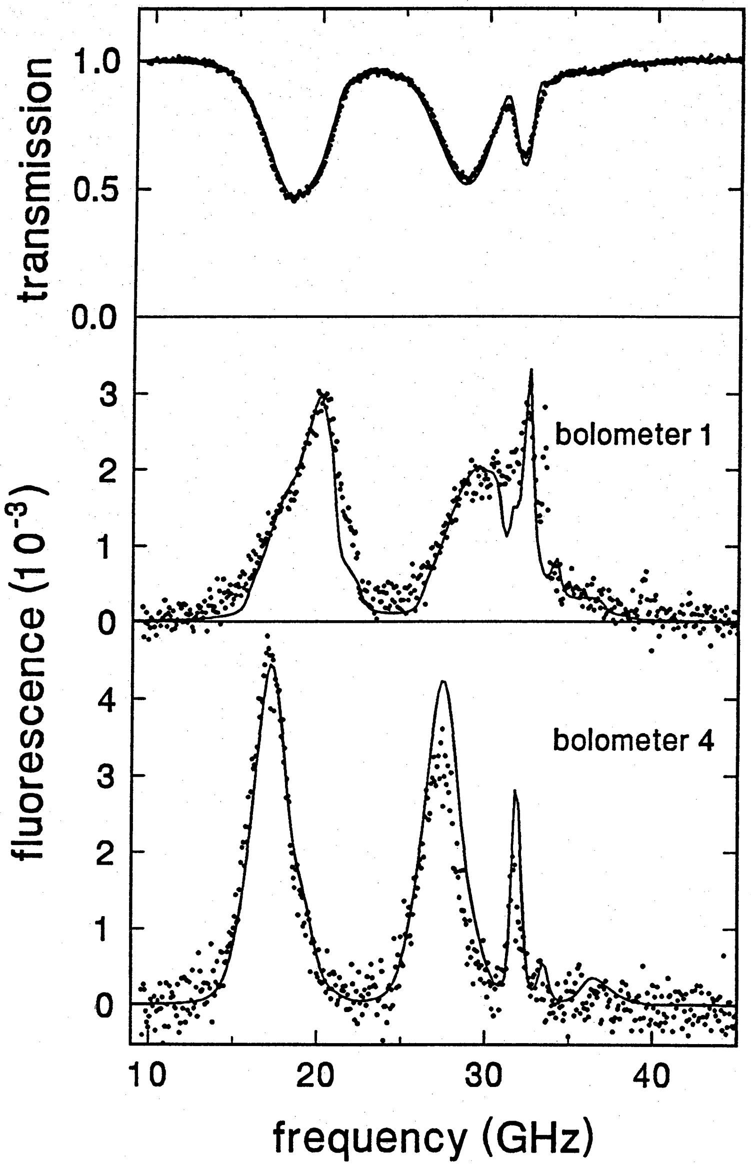

Figure 6.12: Transmission spectrum and corresponding fluorescence spectra of detectors 1 and 4, recorded with right-circularly polarized light. The fluorescence is normalized to the total L_α flux entering the cell. The solid lines are calculated spectra, based on a fit to the transmission spectrum: $T = 46\,\mathrm{mK}$ and $n_0 = 6.9 \times 10^{11}\,\mathrm{cm}^{-3}$.

References

[1] R. van Roijen, J. J. Berkhout, S. Jaakkola, and J. T. M. Walraven, Phys. Rev. Lett. **61**, 931 (1988).

[2] J. M. Doyle, J. C. Sandberg, N. Masuhara, I. A. Yu, D. Kleppner, and T. J. Greytak, J. Opt. Soc. Am. **6**, 2244 (1989).

[3] H. A. Bethe and E. E. Salpeter, *Quantum Mechanics of One- and Two-electron Atoms* (Plenum Publishing Corporation, New York, 1977).

[4] T. W. Hänsch, in *The Hydrogen Atom*, edited by G. F. Bassani, M. Inguscio, and T. W. Hänsch (Springer Verlag, 1988), p. 93.

[5] D. Kleppner, in *The Hydrogen Atom*, edited by G. F. Bassani, M. Inguscio, and T. W. Hänsch (Springer Verlag, 1988), p. 103.

[6] R. G. Beausoleil, Ph. D. Thesis, Stanford University (1986).

[7] R. Loudon, *The Quantum Theory of Light* (Clarendon Press, Oxford, 1988).

[8] S. J. Brodsky and R. G. Parsons, Phys. Rev. **163**, 134 (1967).

[9] K. Shimoda, *Introduction to Laser Physics* (Springer Verlag, 1984).

[10] J. Puerta and P. Martin, Appl. Opt. **20**, 3923 (1981).

[11] K. Helmerson, A. Martin, and D. E. Pritchard, J. Opt. Soc. Am. B **9**, 483 (1992).

[12] I. F. Silvera and J. T. M. Walraven, Phys. Rev. Lett. **45**, 1268 (1980).

[13] A. Corney, *Atomic and Laser Spectroscopy* (Clarendon Press, Oxford, 1977).

Chapter 7

Evaporative cooling

7.1 Introduction

As a first application of our optical diagnostic method, we have studied evaporative cooling [1], in particular the dynamics of the onset of the evaporation process. Evaporative cooling is an efficient method to reduce the temperature of trapped H$\uparrow$ gas and is considered a very promising technique for attaining Bose-Einstein condensation. Evaporative cooling was first proposed and demonstrated by Hess *et al.* at MIT [3, 4]. Subsequently, Masuhara *et al.* showed the feasibility of so-called forced evaporation. In later experiments [6, 7] this technique was improved and temperatures as low as $\sim 100\,\mu$K at densities $\sim 10^{13}\,\mathrm{cm}^{-3}$ were reached. Recently, Setija *et al.* have demonstrated an optical version of forced evaporative cooling [8]. Because evaporative cooling does not have the temperature and density limitations encountered in optical cooling, it is now also being considered for the application to trapped alkalis [2].

Evaporative cooling is based on the preferential removal of atoms with an energy higher than the average energy and on thermalization by elastic collisions. For a gas of atoms, trapped at temperature T in an external potential $U_p(\vec{r})$, the evaporation may be realized by removing the particles which reach a point $\vec{r}_p$, for which $U_p(\vec{r}_p) \equiv \epsilon_{tr} \gg k_B T$. The remaining gas will be driven by thermalizing interatomic collisions to a new equilibrium state at a lower temperature. Simultaneously, these collisions continually generate new atoms which reach $\vec{r}_p$, thus keeping the evaporation going. As the temperature of the trapped gas drops, the number of atoms that are able to reach $\vec{r}_p$ is exponentially suppressed, so eventually the cooling rate is balanced by a competing heating mechanism or becomes negligibly small. In order to keep the cooling rate at a constant level as the temperature drops, the evaporation threshold ϵ_{tr} may be lowered simultaneously, at a rate slow compared to the internal equilibration rate of the trapped gas. Using such forced evaporation techniques it is in principle possible to reach arbitrarily low temperatures. Evaporative cooling techniques have up till now only been applied to the system of trapped H↑ because it is the only system of trapped particles with a lifetime much longer than the internal collisional equilibration time.

To start the evaporation, we energize a small bolometer which is mounted in relatively high field behind the photodiode, as is shown in Fig. 6.4. By boiling off the helium film, the bolometer surface acts as a sorption pump, removing the most energetic atoms, which leads to (evaporative) cooling of the remaining H gas. The photo diode housing acts as a baffle, which protects the H sample against evaporating He atoms. During the evaporation both the temperature and the density of the trapped gas are measured *in situ* non-destructively by Lyman-α spectroscopy. In our approach the trap is first loaded and the trapped gas is allowed to equilibrate with the cell wall at a well-defined temperature. Subsequently, the evaporation is initiated by triggering the bolometer, enabling us to study the dynamics of the onset of the evaporation process independent of the filling of the trap. The objective of the experiments described was a quantitative study of thermalization and evaporation processes in the trapped gas, not the attainment of very low temperatures. Therefore the experiments were performed in a static field geometry, creating well-defined conditions for the spectroscopy of the gas and for the analysis of the evaporation process.

In the experiments at MIT, evaporation is realized differently by letting the most energetic H↑ atoms escape over a magnetic field barrier to a neighbouring zero-field region, where they recombine. The evaporation process is monitored by measuring the heat released in the recombination process. The temperature is either inferred from the evaporation rate, by making use of a model description of the trapped gas [5], or determined by a (destructive) measurement of the energy distribution of the trapped particles [6, 7]. The latter is accomplished by ramping down the magnetic field barrier at a rate faster than the internal equilibration rate of the gas, while measuring the number of escaping atoms as a function of the barrier height.

Before turning to our experimental results, we will discuss a model that has been developed to describe the evaporation process. This model is free of adjustable parameters. For an arbitrary trapping potential it yields a set of coupled differential equations describing the evolution of the temperature T and the number of trapped particles N during evaporation. For a specific trapping potential which accurately describes the field in our Ioffe trap, analytical expressions are found for the particle and energy loss rate during evaporation. These are used in Sect. 7.3 to describe our measurements.

7.2 Evaporation model

To calculate the evolution of the density and the temperature during evaporative cooling we developed a model that is believed to give an accurate description from the very moment the pumping bolometer is triggered. In principle the model can be applied to any system of trapped particles in an arbitrary potential $U_p(\vec{r})$, which interact through s-wave collisions. The essential ingredients are the following: (1) The evaporation may be considered as arising from a perfectly adsorptive wall coinciding with (2) a surface of constant potential energy, $U_p(\vec{r}) = \epsilon_{tr}$, surrounding the gas; (3) Any particle in the trapped gas with a total energy greater than ϵ_{tr} will actually reach the wall and be removed forever; (4) During the evaporation process the trapped gas is in a state of quasi-equilibrium.

We will first discuss these assumptions in detail for our specific experimental situation:

(1) *Sticky wall assumption.* We will show that any atom colliding with the cell wall has a much larger probability to reach the pumping bolometer than to scatter back into a trapped state. For this purpose we discuss the relevant time scales. As was shown in Chapter 3, Sect. 3.3, in thermal equilibrium the average time τ_c between two elastic interatomic collision events is given by $\tau_c^{-1} = \sqrt{2} n_0 \bar{v} \sigma_{el} V_{2e}(T)/V_{1e}(T)$, where n_0 is the central density, $\bar{v} = \sqrt{8 k_B T/\pi m}$ is the average thermal velocity, $\sigma_{el} = 8\pi a_T^2 = 13\,\text{Å}^2$ is the s-wave scattering cross section, and $V_{\ell e}$ is the ℓ^{th} order effective volume. For $T = 0.2\,\text{K}$ and $n_0 = 1 \times 10^{11}\,\text{cm}^{-3}$ $\tau_c \approx 4\,\text{s}$. An atom on a trajectory intersecting the wall will undergo many wall collisions before colliding with another atom. This arises since the radial oscillation period $\tau_r \approx 0.4\,\text{ms} \ll \tau_c$. Many of these wall collisions (3-6%) lead to surface adsorption followed by thermal desorption in a random direction. The residency time in a surface adsorbed state $\tau_a \approx 0.5\,\mu\text{s}$ for a wall temperature $T_w = 0.2\,\text{K}$ (see Sect. 3.3). The average time between two wall sticking events $\tau_w \approx \tau_r/2s$, where s is the sticking probability, $s/T \approx 0.33\,\text{K}^{-1}$ [9]. The average total energy of the H atoms after thermal desorption is $\epsilon_{tr} + \frac{3}{2} k_B T$, which is sufficient to reach the pump by Knudsen flow, impeded by the radial magnetic field gradient, within a time $\tau_p \approx 0.5\,\text{s}$, much shorter than τ_c. In the temperature and density range relevant for our experiments all relevant time scales are well separated, and we have $\tau_a \ll \tau_r \ll \tau_w \ll \tau_p \ll \tau_c$. Therefore the sticky wall assumption is justified.

(2) *Equipotential approximation.* We assume that we may replace the cell wall in our calculations by the $B_w = 1.33\,\text{T}$ equipotential surface. This is a very good approximation for our trap, as the cylindrical side wall nearly coincides with the $B_w = 1.33\,\text{T}$ contour and the side wall comprises the major part of the total wall

surface area (see Fig. 6.4). The calculation of the evaporation rate thus reduces to the calculation of the H$\uparrow$ flux crossing the B_w contour.

(3) *Threshold condition.* We assume that any atom emerging from a collision at a position $\vec{r}$ with a total energy $U_p(\vec{r}) + p^2/2m \geq \epsilon_{tr}$, will actually reach the B_w equipotential surface and be removed from the sample. This means that we neglect the influence of symmetries in the potential U_p, which may give rise to constants of motion other than the total energy, allowing trajectories with a total energy exceeding ϵ_{tr} that do not intersect the B_w equipotential surface. For example, in our Ioffe trap the field $B(\vec{r})$ has axial symmetry at $z = 0$. As a consequence, particles starting at $z = 0$ with only a small velocity in the z direction approximately conserve angular momentum with respect to the symmetry axis, giving rise to wall-grazing orbits with a total energy $> \epsilon_{tr}$. However, this is only true for trajectories which are restricted to a small region around the $z = 0$ plane; for larger starting values of $|z|$ or $|v_z|$ the small deviations from axial symmetry experienced by the particle are sufficient to scramble its axial angular momentum within, typically, a few radial oscillation periods τ_r. Simulations of trajectories indicate for our trap that besides the total energy other constants of motion affect the evaporation process only in a negligible part of the available phase space. Thus the evaporation rate may be simply assumed equal to the flux of atoms passing through the $U_p + p^2/2m = \epsilon_{tr}$ surface in phase space.

(4) *Quasi-equilibrium assumption.* In thermal equilibrium the phase space distribution function f of particles in a potential $U_p(\vec{r})$ is given by

$$f(\vec{r}, \vec{p}) = n_0(2\pi m k_B T)^{-3/2} \exp[-(U_p(\vec{r}) + p^2/2m)/k_B T]. \tag{7.1}$$

The density n_0 is chosen in such a way that f is normalized to the total particle number: $N = \int f(\vec{r}, \vec{p})\, d^3r\, d^3p$, where the integration is over the available phase space. As a result of assumptions (1), (2), and (3), the particle distribution immediately after triggering the pumping bolometer can be described by $f(\vec{r}, \vec{p})$, truncated in phase space at the $U_p + p^2/2m = \epsilon_{tr}$ surface. This is the "pumped" distribution, already discussed in detail in Chapter 3, Sect. 3.2. The assumption of quasi-equilibrium means that during the entire evaporation process the particle distribution may be described by the pumped distribution. On the one hand the pumped distribution is distorted due to the evaporation of particles, on the other hand thermalizing elastic collisions, which do not produce evaporating particles, tend to restore the pumped distribution. The justification for the quasi-equilibrium assumption lies in the fact that for the relevant conditions the total elastic collision rate $N\tau_c^{-1}/2$ for a pumped distribution is always much larger than the evaporation rate. Notice that quasi-equilibrium, as we define it, does not necessarily mean close to thermal equilibrium.

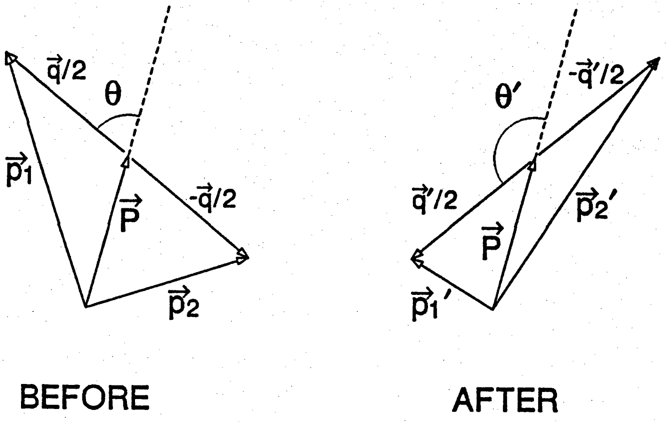

Figure 7.1: Atomic momenta before and after an elastic collision.

For example, the (pumped) distribution immediately after switching on the pump is far from equilibrium, as will be shown in Sect. 7.2.2.

In Sect. 7.2.1 relatively simple expressions will be derived for the particle and the energy loss rate during evaporative cooling in an arbitrary potential, using the above model. These general expressions will be applied in Sect. 7.2.2 to a specific potential shape, which accurately describes the field in a Ioffe trap. For this particular case closed analytical expressions are found. As a first application these expressions will be used in Sect. 7.2.3 to estimate the lowest temperatures that can be reached with evaporative cooling. In Sect. 7.3 they will be used to fit our experimental data.

7.2.1 General case

Consider an elastic collision event at a point $\vec{r}$ between two H atoms characterized by initial momenta $\vec{p}_1$ and $\vec{p}_2$, and final momenta $\vec{p}_1{}'$ and $\vec{p}_2{}'$ (see Fig. 7.1). We introduce center-of-mass and relative momentum coordinates $\vec{P} = (\vec{p}_1 + \vec{p}_2)/2$ and $\vec{q} = \vec{p}_2 - \vec{p}_1$. This is convenient because in an elastic collision $\vec{P}$ and $q = |\vec{q}|$ are conserved and only the angle θ between $\vec{q}$ and $\vec{P}$ and the azimuthal angle ϕ change. In a thermal distribution all initial angles (θ, ϕ) have equal probability. The final angles (θ', ϕ') are independent of the initial angles (θ, ϕ), since the H atoms only scatter through s-wave collisions. Thus all final angles (θ', ϕ') also have equal probability.

In order to calculate the evaporation rate we write the general equation for the total elastic collision event rate of a thermal distribution (see Chapter 3, Sect. 3.3):

$$\Gamma_c = \frac{\sigma_{el} n_0^2 (2\pi m k_B T)^{-3}}{2m} \int d^3r\, e^{-2U_p(\vec{r})/k_BT} \int d^3P\, e^{-P^2/mk_BT} \int d^3q\, q\, e^{-q^2/4mk_BT}. \tag{7.2}$$

In a pumped distribution all particles have a total energy

$$p^2/2m + U_p(\vec{r}) \le \epsilon_{tr}, \tag{7.3}$$

so during evaporation only collisions occur which are characterized by initial values P, q, and θ satisfying

$$P^2 + q^2/4 + Pq|\cos\theta| \le 2m[\epsilon_{tr} - U_p(\vec{r})]. \tag{7.4}$$

In these collisions an evaporating atom is produced if the final values $P' = P$, $q' = q$, and θ' fulfill

$$P^2 + q^2/4 + Pq|\cos\theta'| \ge 2m[\epsilon_{tr} - U_p(\vec{r})]. \tag{7.5}$$

The calculation of the evaporation rate entails performing the integral (7.2) over the part of phase space defined by the relations (7.4) and (7.5). To this purpose the evaporation condition is incorporated in the integrand by averaging for fixed P and q over all final angles (θ', ϕ') which satisfy Eq. (7.5). The resulting form is integrated over P, q, θ, and ϕ, with the integration boundaries defined by condition (7.4). We will now discuss the calculation in detail.

Let us consider the class of colliding particle pairs at position $\vec{r}$, characterized by fixed values of P and q. The fraction F of these colliding pairs which actually is part of the pumped distribution, i.e., which fulfills condition (7.4), can easily be calculated using the fact that all scattering angles have equal probability:

$$F = \frac{1}{4\pi}\int_0^{2\pi} d\phi \int d\theta\, \sin\theta, \tag{7.6}$$

where the θ integration is restricted to $|\cos\theta| \le [2m(\epsilon_{tr} - U_p) - P^2 - q^2/4]/Pq$. We find

$$F(\vec{r}, P, q) = \frac{2m[\epsilon_{tr} - U_p(\vec{r})] - P^2 - q^2/4}{Pq}. \tag{7.7}$$

Expression (7.7) holds for values of P, q, and $\vec{r}$ which satisfy

$$P^2 + q^2/4 \le 2m[\epsilon_{tr} - U_p(\vec{r})], \tag{7.8}$$

which is equivalent to $F \ge 0$ and a necessary condition for relation (7.4). For values P, q, and $\vec{r}$ which do not satisfy (7.8), $F < 0$, which is clearly unphysical. Further, $F \le 1$ for values of P, q, and $\vec{r}$ which satisfy

$$(P + q/2)^2 \ge 2m[\epsilon_{tr} - U_p(\vec{r})], \tag{7.9}$$

which is a necessary condition for relation (7.5). If Eq. (7.9) is not satisfied then $F > 1$, which is also unphysical. Thus all pairs which are characterized by the relations (7.8) and (7.9) have a finite probability F of being part of the pumped distribution. These same pairs also have a finite probability of producing an evaporating particle, i.e., of fulfilling condition (7.5). Since all final angles (θ', ϕ') are equally probable (s-wave scattering), the condition (7.5) is complementary to condition (7.4). Therefore the probability for producing an evaporating particle is equal to $1 - F$ for all P, q, and $\vec{r}$ obeying (7.8) and (7.9).

Taking into account that in the pumped distribution in each evaporating scattering event exactly one evaporating particle is produced, we can now write the following expression for the flux $\dot{N}_{ev}$ of evaporating atoms:

$$\dot{N}_{ev} = -\frac{\sigma_{el} n_0^2 (2\pi m k_B T)^{-3}}{2m} \int_{U_p \leq \epsilon_{tr}} d^3r \, \exp[-2U_p(\vec{r})/k_B T] \times$$

$$\int_0^Q dP \, 4\pi P^2 \int_{2(Q-P)}^{2Q} dq \, 4\pi q^3 \, F(\vec{r}, P, q) \, [1 - F(\vec{r}, P, q)] \, \exp[-(P^2 + q^2/4)/m k_B T], \tag{7.10}$$

where $Q(\vec{r}) \equiv \sqrt{2m[\epsilon_{tr} - U_p(\vec{r})]}$ is the maximum particle momentum at a position $\vec{r}$ in the pumped distribution, or, equivalently, the minimum momentum required to reach the pumping wall. The integration boundaries for $\vec{r}$, P, and q combined with the factor $F(1 - F)$ in the integrand express the conditions (7.4) and (7.5).

After some straightforward manipulation, in which we chose the new variable $y \equiv [U_p(\vec{r}) + (P^2 + q^2/4)/m - \epsilon_{tr}]/k_B T$, Eq. (7.10) can be written in the following much simpler form:

$$\dot{N}_{ev} = -\frac{4}{3\sqrt{\pi}} n_0^2 \, \sigma_{el} \, \bar{v} \, V_{3/2}, \tag{7.11}$$

where the volume V_ν is defined by

$$V_\nu \equiv \int_{U_p \leq \epsilon_{tr}} d^3r \, \exp[-U_p(\vec{r})/k_B T] \int_0^{y_m} dy \, (y_m - y) y^\nu \exp(-y), \tag{7.12}$$

with $y_m(\vec{r}) = [\epsilon_{tr} - U_p(\vec{r})]/k_B T$.

The energy flux carried by the evaporating particles can be calculated in a similar way. Again we consider pairs of colliding particles at position $\vec{r}$, characterized by fixed momenta P and q. By averaging over the final angles (θ', ϕ'), the average energy $\langle E_{ev} \rangle$ per particle carried by the evaporating particles can be calculated straightforwardly:

$$\langle E_{ev} \rangle = \frac{\int_0^{2\pi} d\phi' \int d\theta' \, \sin\theta' \, [U_p(\vec{r}) + (P^2 + q^2/4 + Pq\cos\theta')/2m]}{\int_0^{2\pi} d\phi' \int d\theta' \, \sin\theta'}, \tag{7.13}$$

where the θ' integrations are restricted to $|\cos\theta'| \geq [2m(\epsilon_{tr} - U_p) - P^2 - q^2/4]/Pq$ (condition (7.5)). We find

$$\langle E_{ev} \rangle = \epsilon_{tr} + [1 - F(\vec{r}, P, q)]\frac{Pq}{4m}, \tag{7.14}$$

where the fraction F is given by Eq. (7.7). Again, Eq. (7.14) only holds if $0 \leq F \leq 1$, i.e., for P, q, and $\vec{r}$ which satisfy (7.8) and (7.9). As a result, the energy loss rate $\dot{E}_{ev}$ due to evaporation is given by

$$\begin{aligned} \dot{E}_{ev} = -\frac{\sigma_{el} n_0^2 (2\pi m k_B T)^{-3}}{2m} \int_{U_p \leq \epsilon_{tr}} d^3r \, \exp[-2U_p(\vec{r})/k_B T] \times \\ \int_0^Q dP\, 4\pi P^2 \int_{2(Q-P)}^{2Q} dq\, 4\pi q^3\, F(\vec{r}, P, q)\, [1 - F(\vec{r}, P, q)] \times \\ \{\epsilon_{tr} + [1 - F(\vec{r}, P, q)]\frac{Pq}{4m}\} \exp[-(P^2 + q^2/4)/m k_B T]. \end{aligned} \tag{7.15}$$

After some manipulation, similar to the calculation of $\dot{N}_{ev}$, this can be written in the following much simpler form:

$$\dot{E}_{ev} = \dot{N}_{ev} \left\{ \epsilon_{tr} + \frac{2V_{5/2}}{5V_{3/2}} k_B T \right\}. \tag{7.16}$$

Under the given assumptions Eqs. (7.11) and (7.16) describe the evaporation process exactly. The problem has been reduced to the calculation of the functions $V_{3/2}(T)$ and $V_{5/2}(T)$, which can be calculated straightforwardly for an arbitrary potential. In Sect. 7.2.2 analytical expressions are derived for the volumes $V_{3/2}$ and $V_{5/2}$ for a potential which closely resembles the field in our Ioffe trap.

7.2.2 Ioffe trap

As was shown in Chapters 2 and 3, the modulus of the magnetic field in our Ioffe trap can be approximated quite accurately by

$$B(\rho, z) = \sqrt{\alpha^2 \rho^2 + [B_0 + \beta(z - z_0)^2]^2}, \tag{7.17}$$

where $B_0 = 0.1\,\mathrm{T}$, $z_0 = -7.5\,\mathrm{mm}$, $\alpha = 2.2\,\mathrm{T/cm}$, and $\beta = 0.023\,\mathrm{T/cm^2}$. In Chapter 3, Sect. 3.2, the following expression for the density of states of a pure d state gas in a field of the form (7.17) was derived:

$$\rho(\epsilon) = \frac{(2m\pi^2)^{3/2}}{2\mu_B^{5/2}\alpha^2\sqrt{\beta}} \epsilon^3 (1 + \frac{2\mu_B B_0}{\epsilon}). \tag{7.18}$$

Using Eq. (7.18), we have plotted in Fig. 7.2 the energy distribution function $N(\epsilon) = n_0 \rho(\epsilon) \exp(-\epsilon/k_B T)$ of an evaporating sample as a function of energy for

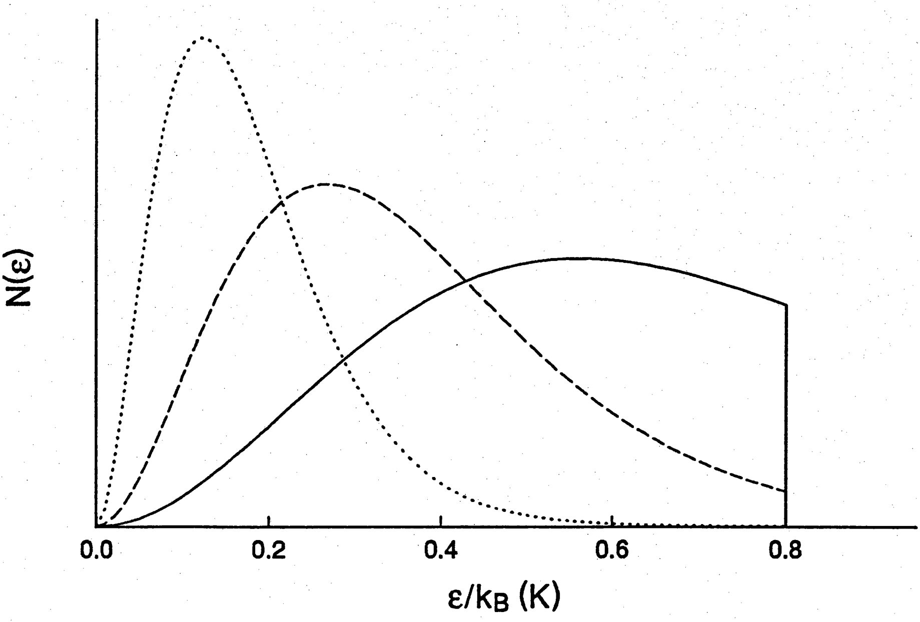

Figure 7.2: Energy distributions of an evaporating sample in a Ioffe trap. Solid curve: $T = 0.2\,\mathrm{K}$ ($\eta = 4$); dashed curve: $T = 0.1\,\mathrm{K}$ ($\eta = 8$); dotted curve: $T = 0.05\,\mathrm{K}$ ($\eta = 16$). The three distributions have been calculated for equal values of n_0.

three values of T. $N(\epsilon)d\epsilon$ is the number of trapped atoms in a small energy range $d\epsilon$ around energy ϵ. The distributions are cut off at $\epsilon = \epsilon_{tr}$; for lower values of ϵ they correspond to ordinary Boltzmann distributions. Note that the pumped distributions can be far from equilibrium, in which case T cannot be interpreted as a thermodynamical temperature, as was already mentioned in Chapter 3, Sect. 3.2. Likewise, the density n_0 as we define it (Eq. (7.1)), is strictly speaking not equal to the density at the minimum of the potential well. The latter identification only applies to true thermal distributions. For our purpose T and n_0 should be considered as convenient parameters, characterizing the pumped distribution. Nevertheless, for $k_BT \leq \epsilon_{tr}/8$ ($\eta > 8$) only a small error is made if T is interpreted as the thermodynamical temperature of the system and n_0 as the density at the minimum.

Fig. 7.2 nicely illustrates the evolution of the distribution during evaporative cooling in our Ioffe trap. Before switching on the pump, the gas is in thermal equilibrium with the cell wall at $T = 0.2\,\mathrm{K}$. The solid curve is the energy distribution immediately after triggering the pumping bolometer. Clearly, a substantial part of the sample has been removed instantly. Subsequently, the average energy of the particles is reduced as more particles evaporate due to redistribution of the energy through elastic interatomic collisions. For $k_BT < \epsilon_{tr}/10$ ($\eta > 10$) the pumped distribution becomes indistinguishable from a full thermal distribution and the evaporation has virtually come to a standstill.

To describe the evaporation process quantitatively we need expressions for the volumes $V_{3/2}$ and $V_{5/2}$. Since the integrand of Eq. (7.12) only depends on U_p, it is convenient to use the magnetic density of states ρ_M, which was introduced in Chapter 3, Sect. 3.2. In the case of a pure d state gas in a magnetostatic trap Eq. (7.12) can then be reduced to the following 2-dimensional integral:

$$V_\nu = \int_{B_0}^{B_w} dB\, \rho_M(B) \exp[-\mu_B(B - B_0)/k_BT] \int_0^{y_m} dy\, (y_m - y) y^\nu \exp(-y), \tag{7.19}$$

where in this case $y_m = \mu_B(B_w - B)/k_BT$. In Sect. 3.2 the following expression for the magnetic density of states of a field of the form (7.17) was derived:

$$\rho_M(B) = \frac{4\pi}{\alpha^2\sqrt{\beta}}[(B - B_0)^{3/2} + B_0(B - B_0)^{1/2}]. \tag{7.20}$$

Using Eq. (7.19), the volumes $V_{3/2}$ and $V_{5/2}$ can now be calculated straightforwardly:

$$\begin{aligned} V_{3/2} = (3\sqrt{\pi}/4)\, V_0\, \eta^{-5/2} \exp(-\eta)\{\eta - 5 + \tfrac{2}{3}\xi\eta(\eta - 4) + \exp(-\eta)\times \\ [\tfrac{\eta^4}{24}(1 + \tfrac{8}{3}\xi) + \tfrac{\eta^3}{3}(1 + 2\xi) + \tfrac{3}{2}\eta^2(1 + \tfrac{4}{3}\xi) + 4\eta(1 + \tfrac{2}{3}\xi) + 5]\}, \end{aligned} \tag{7.21}$$

and

$$\begin{aligned} V_{5/2} = (15\sqrt{\pi}/8)\, V_0\, \eta^{-5/2} \exp(-\eta)\{\eta - 6 + \tfrac{2}{3}\xi\eta(\eta - 5) + \exp(-\eta)\times \\ [\tfrac{\eta^5}{120}(1 + \tfrac{10}{3}\xi) + \tfrac{\eta^4}{12}(1 + \tfrac{8}{3}\xi) + \tfrac{\eta^3}{2}(1 + 2\xi) + 2\eta^2(1 + \tfrac{4}{3}\xi) + 5\eta(1 + \tfrac{2}{3}\xi) + 6]\}, \end{aligned} \tag{7.22}$$

where $V_0 = 3\pi^{3/2}\alpha^{-2}\beta^{-1/2}(B_w - B_0)^{5/2}$, $\eta = \mu_B(B_w - B_0)/k_BT$, and $\xi = B_0/(B_w - B_0)$. In the field geometry in which the evaporation measurements were performed $V_0 = 38\,\text{cm}^3$, $\xi = 0.081$, and $\eta T = 0.82\,\text{K}$.

From Chapter 3 we also know the effective volume $V_{1e} \equiv N/n_0$ of a pumped distribution in the potential (7.17):

$$V_{1e} = V_0\, \eta^{-5/2}(1 + \frac{2}{3}\xi\eta)\left\{1 - e^{-\eta}[1 + \eta + \frac{1}{2}\eta^2 + \frac{1}{6}\frac{\eta^3}{1 + \frac{2}{3}\xi\eta}]\right\}, \tag{7.23}$$

which makes the description complete. The combination of Eqs. (7.11), (7.16), (7.21), (7.22), and (7.23) fully describes the evaporation process of a pure d state gas in a magnetostatic trap of the form (7.17). These equations will be used in the Sect. 7.3 to describe the measurements.

For $\eta > 8$, i.e., in our geometry for $T < 0.1\,\text{K}$, the equations may be simplified by neglecting the $e^{-2\eta}$ terms. The particle and energy loss rate during evaporation can then be approximated accurately by

$$\frac{\dot{N}_{ev}}{N} = -n_0 \bar{v} \sigma_{el} \frac{\eta - 5 + \frac{2}{3}\xi\eta(\eta - 4)}{1 + \frac{2}{3}\xi\eta} \exp(-\eta), \tag{7.24}$$

and

$$\dot{E}_{ev} = \dot{N}_{ev} \left\{ \epsilon_{tr} + k_B T \frac{\eta - 6 + \frac{2}{3}\xi\eta(\eta - 5)}{\eta - 5 + \frac{2}{3}\xi\eta(\eta - 4)} \right\}. \tag{7.25}$$

For smaller values of η it is essential that all other terms are taken into account as well. For example, expression (7.24) yields a positive value for $\dot{N}_{ev}$ for $\eta > 5$, which is clearly unphysical. The potential experienced by the particles approaches a harmonic well in the limit $k_B T \ll \mu_B B_0$ ($\xi\eta \gg 1$). Eqs. (7.11) and (7.16) then reduce to:

$$\begin{array}{rcl} \dot{N}_{ev}/N &=& -n_0 \bar{v} \sigma_{el} (\eta - 4) \exp(-\eta) \\ \dot{E}_{ev} &=& \dot{N}_{ev} [\epsilon_{tr} + k_B T (\eta - 5)/(\eta - 4)]. \end{array} \tag{7.26}$$

Note that the condition $\xi\eta \gg 1$ does not necessarily imply that the potential well has a harmonic shape up to the evaporation threshold ϵ_{tr}. For the validity of Eqs. (7.26) it is sufficient that the potential is harmonic in the region of the trap where the majority of the particles reside. In the other extreme, i.e., if $\xi\eta \ll 1$ (for instance if $B_0 = 0$), the equations take the following simple form:

$$\begin{array}{rcl} \dot{N}_{ev}/N &=& -n_0 \bar{v} \sigma_{el} (\eta - 5) \exp(-\eta) \\ \dot{E}_{ev} &=& \dot{N}_{ev} [\epsilon_{tr} + k_B T (\eta - 6)/(\eta - 5)]. \end{array} \tag{7.27}$$

Apparently, for large values of η (> 8) the evaporative behaviour is not very sensitive to the exact shape of the trapping field. For fixed values of T and n_0 both the particle loss rate and the energy loss rate per evaporating particle are somewhat larger for a harmonic well. Notice that the average excess kinetic energy per evaporating particle is always less than $k_B T$.

7.2.3 Minimum temperature

In the absence of a competing heating process, evaporative cooling in principle leads to arbitrarily low temperatures. In practice, the lowest temperatures that can be reached are always limited by the intrinsic heating associated with collisional relaxation (Chapter 3, Sect. 3.5). Whereas evaporative cooling relies on the preferential removal of the most energetic atoms, relaxation heating is due to the preferential removal of atoms with an energy less than average: Collisional relaxation mainly takes place in the high-density region, i.e., near the center of the trap. The particle loss rate due to evaporation and the particle loss rate due to collisional relaxation both have the same density dependence, $\dot{N} \sim n^2$, since both are associated with two-body collisional mechanisms. Hence, the evaporative cooling rate and the relaxation heating rate also have the same density dependence. Consequently, for a given trapping geometry there is a lowest temperature T_{min}, independent of the density n_0, at which evaporative cooling and relaxation heating exactly cancel. Once this temperature has been reached, the sample will stay at T_{min}, if no other heating processes are involved [3].

We will now make an estimate of the equilibrium temperature T_{min} for the simple case of a sample of d state atoms in a harmonic potential, using the previously obtained results. The dipolar relaxation rate $\dot{N}_{dip}$ is given by (see Sect. 3.4):

$$\dot{N}_{dip} \approx -n_0^2 G_0 V_{2e}, \tag{7.28}$$

where $G_0 \approx 1 \times 10^{-15}\,\mathrm{cm}^3/\mathrm{s}$ is the dipolar rate constant at the field minimum and $V_{2e}(T) = V_{1e}(T/2)$ is the second order effective volume. The corresponding rate of energy loss $\dot{E}_{dip}$ from the sample is given by (see Sect. 3.5):

$$\dot{E}_{dip} \approx \dot{N}_{dip}(\gamma_{2e} + 3/2)k_B T, \tag{7.29}$$

where $\gamma_{2e}(T)k_B T = (1/2)\gamma_{1e}(T/2)k_B T$ is the second order average potential energy per particle. For a harmonic potential $\gamma_{2e} = 3/4$. The total energy per trapped particle is by definition equal to $(\gamma_{1e} + 3/2)k_B T$, so a steady state temperature is reached when

$$\dot{E}_{dip} + \dot{E}_{ev} = (\dot{N}_{dip} + \dot{N}_{ev})(\gamma_{1e} + 3/2)k_B T. \tag{7.30}$$

Using Eqs. (7.26) and the fact that $V_{1e}(T) \sim T^{3/2}$ and $\gamma_{1e} = 3/2$ for a harmonic potential, Eq. (7.30) can be rewritten in the form

$$\frac{8\sqrt{2}}{3}\frac{\bar{v}\sigma_{el}}{G_0}(\eta^2 - 6\eta - 7)\exp(-\eta) = 1. \tag{7.31}$$

From Eq. (7.31) follows that $T_{min} = 57\,\mathrm{mK}$ is the lowest temperature that can be reached in a harmonic potential with a well depth $\epsilon_{tr}/k_B = 0.8\,\mathrm{K}$, which corresponds to $\eta = 14.5$. A temperature $T_{min} = 90\,\mu\mathrm{K}$ may be reached for $\eta = 10$, i.e., by lowering the evaporation barrier to $\epsilon_{tr}/k_B = 0.9\,\mathrm{mK}$ (corresponding to $B_w - B_0 = 13.5\,\mathrm{Gauss}$). These numbers are approximately the same for other shapes of the potential [10]. In practice T_{min} is always approximately one tenth of the trapping depth.

As was already explained in Chapter 3, Sect. 3.5, collisional relaxation heating does not play any role of importance in the experiments described in this work. Collisions with relatively high-energy ^{4}He atoms, which are sprayed from a "hot" spot on the cell wall, was probably the dominant heating mechanism in the evaporation measurements. Since, unlike collisional relaxation, this is not a second order process, the background gas heating cannot be neutralized in a density independent way by evaporative cooling and the temperature will therefore never reach a steady state value. Initially, the relatively high densities in the trapped sample lead to very efficient evaporative cooling and the sample cools in spite of background gas heating. However, the cooling per trapped particle becomes less as the temperature and number of trapped particles drop. On the other hand, the heating per trapped particle due to background gas is approximately independent of the density and the temperature of the trapped gas. As a consequence, the evaporative cooling will eventually be overcome by background gas heating and the sample will heat up again. The temperature of the trapped gas will go through a minimum; the value of the minimum temperature depends on the initial values of both T and n_0.

7.3 Evaporation measurements

7.3.1 3-point transmission spectroscopy

We have measured the evolution of T and n_0 during evaporative cooling by means of transmission spectroscopy. As will be shown, the distribution of particles changes quite rapidly during the onset of the evaporation, typically on a time scale of a few seconds under our conditions, so it is not possible to monitor T and n_0 by full spectral scans of the $2P$ multiplet, which typically take $10 - 30\,\mathrm{s}$ (Chapter 6). Instead, we keep track of only a small, but characteristic, part of the spectrum, using a chain of three acousto-optic modulators (AOM, see Chapter 5, Sect. 5.3). Our AOM arrangement enables fast pulse-to-pulse switching of the VUV frequency between $\nu - 0.48\,\mathrm{GHz}$, $\nu + 0.48\,\mathrm{GHz}$, and $\nu + 0.90\,\mathrm{GHz}$, where ν is the 6^{th} harmonic of the cw laser frequency. In this way the evolution of a small part of the spectrum can be recorded at three fixed frequencies with a time resolution determined by the repetition rate of the L_α pulses (maximum rep. rate $\sim 50\,\mathrm{Hz}$).

In order to determine T and n_0 during the evaporation process with a minimum of particle loss due to optical pumping, the frequency ν was tuned to a fixed frequency in the blue wing of the σ_1 line (see Fig. 7.3). The reason for choosing this part of the spectrum is the fact that the σ_1 transition is the only transition which forms a closed optical cycle. In addition, the σ_1 line is the only line with a positive Zeeman shift, so contributions from other lines are strongly suppressed in its blue wing. As a result the transmission t_α of the sample in the blue wing of σ_1 is a well-behaved, monotonous function of ν, T, and n_0. In order to calculate $t_\alpha(\nu, T, n_0)$ we use the theory of Chapter 6. We assume that *before* switching on the pump the density

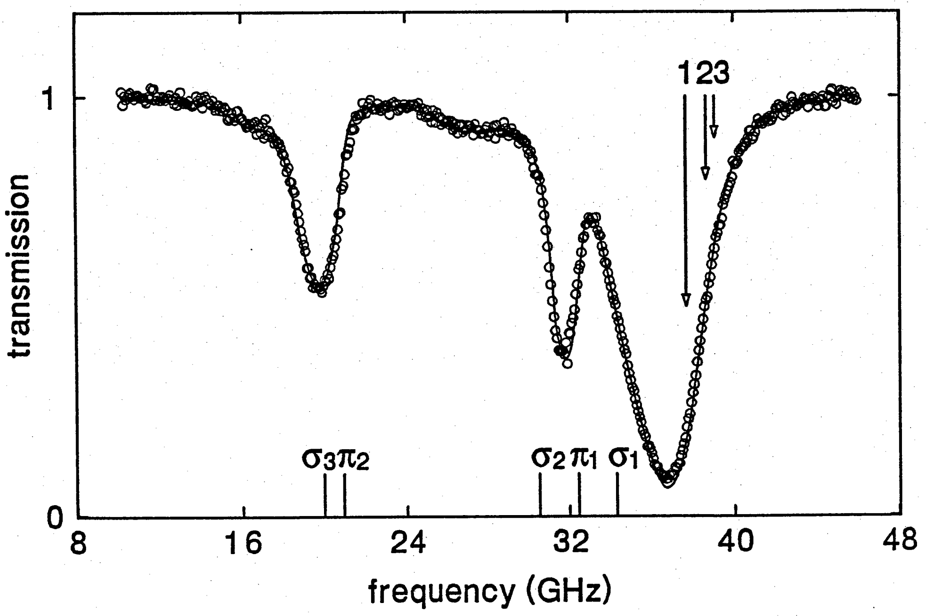

Figure 7.3: Transmission spectrum recorded with left-circularly polarized light. The arrows indicate the three AOM frequencies. The vertical bars denote the resonant frequencies of the five allowed transitions for $B = B_0$.

distribution is given by the ordinary Boltzmann distribution (7.32):

$$n(\vec{r}) = n_0 \exp[-U_p(\vec{r})/k_B T], \tag{7.32}$$

and *after* switching on the pump by the "pumped" density distribution (Sect. 3.2.1):

$$n_p(\vec{r}) = n(\vec{r}) \left[\operatorname{erf}(\sqrt{\frac{\epsilon_{tr} - U_p(\vec{r})}{k_B T}}) - \frac{2}{\sqrt{\pi}} \sqrt{\frac{\epsilon_{tr} - U_p(\vec{r})}{k_B T}} \exp(-\frac{\epsilon_{tr} - U_p(\vec{r})}{k_B T}) \right] . \tag{7.33}$$

Using these parametrizations of the density distributions there should be no discontinuity in T and n_0, according to our model, when switching on the pump. The exact calculation of the transmission gives rise to complicated functions $t_\alpha(\nu, T, n_0)$. However, using some simplifications a relatively simple expression may be derived which is a good first order approximation for t_α and which gives somewhat more insight in the method of 3-point transmission spectroscopy:

Making use of the fact that approximately $\vec{B} \parallel \vec{k}$ and that, to a good approximation, only the σ_1 resonance contributes, the vector character of the light and dispersive effects may be neglected. The extinction of the Lyman-α intensity I is then described by $I^{-1}(\partial I/\partial z) = n\,\sigma$ (Sect. 6.5), where σ is the local absorption cross section. The σ_1 resonant absorption cross section is independent of B and its resonant frequency is a linear function of B. In the relatively high fields corresponding to the far blue wing of σ_1, $B \sim z^2$. If we approximate the local absorption line shape by a δ-function (thus neglecting the Doppler broadening with respect to the Zeeman broadening) and we use the ordinary Boltzmann density distribution (7.32), the following simple form for the L_α transmission t_α in the blue wing of σ_1 may be derived:

$$\ln t_\alpha = -\sigma_0 n_0 \ell_0 \sqrt{\Delta\nu_w/\Delta\nu}\,\exp(-h\Delta\nu/k_B T). \tag{7.34}$$

Here $\sigma_0 = 3\lambda_\alpha^2/2\pi$ and $\Delta\nu = \mu_B(B - B_0)/h$ is the detuning from the σ_1 resonant frequency at the trap minimum. The length $\ell_0\sqrt{\Delta\nu_w/\Delta\nu}$ is an effective extinction length, with $\ell_0 \approx 0.5\,\mathrm{mm}$ and $\Delta\nu_w$ the detuning for $B = B_w$. Eq. (7.34) is a good first order approximation for the dependence of t_α on $\Delta\nu$, T, and n_0. Clearly, if the transmission t_α is known for two values of $\Delta\nu$, then T and n_0 are uniquely determined. In practice we measure t_α for three different values of $\Delta\nu$, which allows us to check the consistency of the method and to make an estimate of the error. In the actual analysis of our data we make use of a more precise parametrization, in which ℓ_0 is a slowly varying function of $\Delta\nu$, T, and n_0. Details related to, e.g., Doppler broadening, the finite radial extent of the sample, and the fact that after starting the evaporation the pumped distribution applies instead of a Boltzmann density distribution, are lumped into ℓ_0. Eq. (7.34) holds for left-circularly polarized light. For arbitrary polarization t_α should be transformed appropiately.

7.3.2 Dynamics of evaporative cooling

In Fig. 7.4 the transmission versus time is shown during evaporation, at the three frequencies indicated by arrows in Fig. 7.3. The data shown were taken on a single sample of trapped H$\uparrow$ with an integration time of 80 ms (4 pulses) per data point. The jump at $t = 38$ s coincides with the triggering of the evaporation bolometer and marks the "immediate" removal of a part of the sample. The inset reveals that this removal takes about 0.5 s, consistent with Knudsen flow to the pump, impeded by the presence of the magnetic potential. To determine T and n_0, the three data points at each time step are fitted to Eq. (7.34), after filtering the raw data (time constant 0.5 s). The result is shown in Fig. 7.5. For the calculation of the T and n_0 data points the proper density distributions are used, i.e., an ordinary Boltzmann density distribution (Eq. (7.32)) for $t < 38$ s and a pumped density distribution (Eq. (7.33)) for $t > 38$ s. Therefore, for $t < 38$ s, T is the thermodynamical temperature of the gas and n_0 the central density, whereas for $t > 38$ s T and n_0 should be interpreted

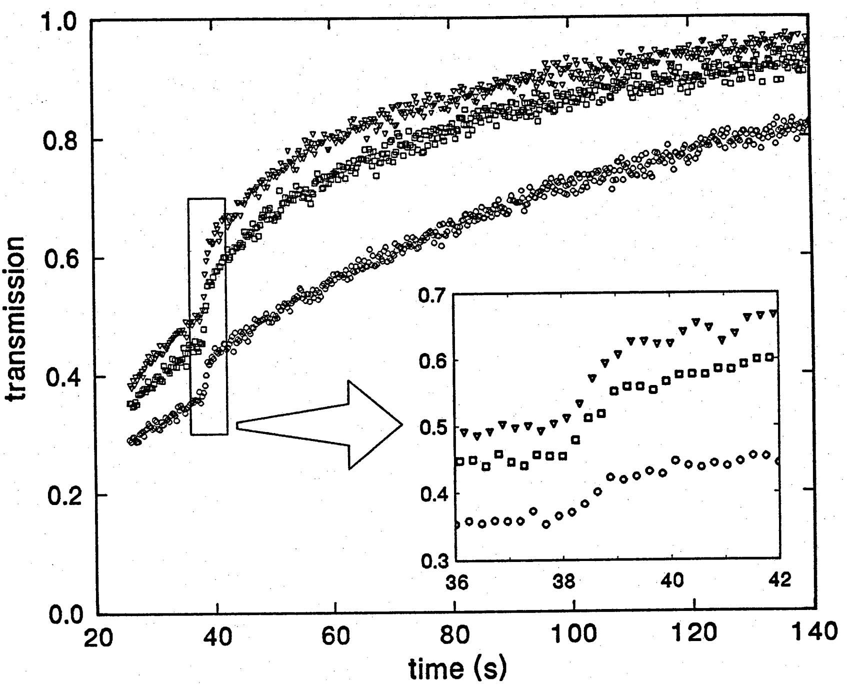

Figure 7.4: Transmission vs time for three fixed frequencies (circles: $\nu-0.48$ GHz; squares: $\nu+0.48$ GHz; triangles: $\nu+0.90$ GHz) in the blue wing of the σ_1 line. The jump at $t = 38$ s (inset) coincides with the triggering of the evaporation.

as the usual parameters characterizing the pumped distribution (see Sect. 3.2.1). Initially the gas is in thermal equilibrium with the cell wall at $T = T_w \approx 0.25$ K and the density decays quickly due to a surface-induced mechanism. At $t = 38$ s a substantial fraction ($\sim 30\%$) of the trapped gas is removed. After triggering the bolometer, T immediately drops to well below T_w. The resulting decrease of the effective volume V_{1e} leads to an increase of n_0, in spite of the fact that particles are being removed.

To describe the observed behaviour quantitatively, we assume that the evolution of T and n_0 is determined by the combination of evaporation and collisions with ^{4}He background gas. Using the heat balance equation derived in Sect. 3.5, we arrive at the following equation describing the temperature evolution:

$$\dot{T} = \frac{\dot{E}_{ev} - \dot{N}_{ev} k_B T(\gamma_{1e} + 3/2)}{N k_B(\gamma_{1e} + T(\partial\gamma_{1e}/\partial T) + 3/2)} + T_4 \tau_4^{-1}. \tag{7.35}$$

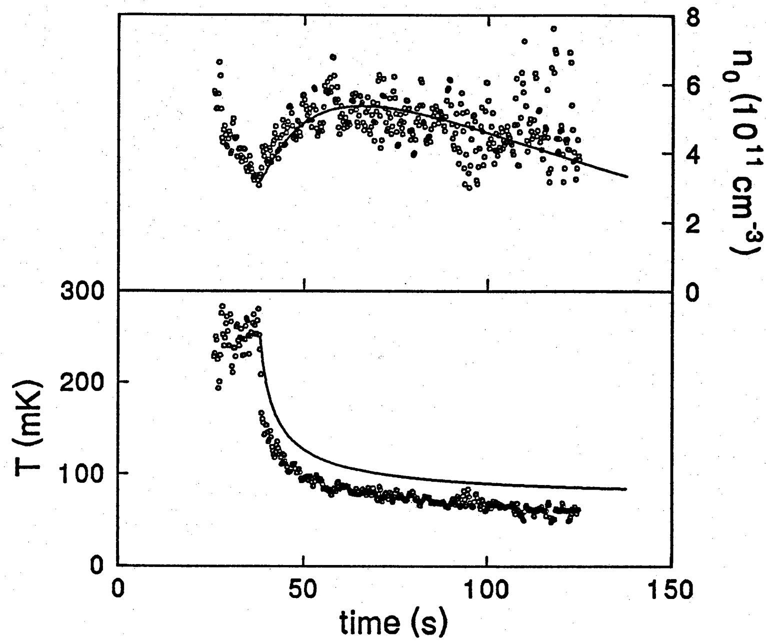

Figure 7.5: T and n_0 during evaporation calculated from the transmission data shown in Fig. 7.4. The solid lines are the results of the evaporation model (see text).

The particle loss is given by

$$\frac{\dot{N}}{N} = \frac{\dot{N}_{ev}}{N} - \tau_4^{-1}. \tag{7.36}$$

Here the phenomenological decay time τ_4 and temperature T_4 are introduced to account for the particle loss and heating due to ^{4}He background gas. In Sect. 3.5 some rough estimates were made of these quantities; for the description of the measurements, however, they will be used as free fitting parameters. For the calculation of $\dot{N}_{ev}$ and $\dot{E}_{ev}$ Eqs. (7.11), (7.16), (7.21), and (7.22) are used. Further, Eq. (7.23) is used for the effective volume $V_{1e} \equiv N/n_0$ and for the calculation of $\gamma_{1e} \equiv (T/V_{1e})(\partial V_{1e}/\partial T)$, the effective average potential energy per trapped particle in units $k_B T$.

In Fig. 7.5 the results of the model are compared with the experimental data. The solid curves have been obtained by integrating the coupled differential equations (7.35) and (7.36). These curves are completely determined by the starting conditions T_i and n_{0i}, and the choice of τ_4 and T_4. The best fit was obtained by choosing $\tau_4 =$ 90 s and $T_4 = 0$. The time scale $\tau_4 = 90$ s for particle loss due to ^{4}He background gas is roughly in agreement with the estimate of Sect. 3.4. Apparently the corresponding heating term is too small to be observed on the relatively short time scales of our measurements. The first few seconds after triggering the bolometer are completely determined by the evaporation dynamics. The initial sharp drop in T is due to the anomalously small value of the heat capacity $Nk_B[\gamma_{1e} + T(\partial\gamma_{1e}/\partial T) + 3/2]$ of the pumped distribution at the relatively high initial temperature (see, for instance, Chapter 3, Fig. 3.5 and Fig. 7.2).

The model gives a good description of the evaporation process, in view of the absence of adjustable parameters. It is not possible to improve the fit by using other values for the elastic scattering cross section ($\sigma_{el} = 13\,\text{Å}^2$) or for the well depth ($\epsilon_{tr}/k_B = 0.82\,\text{K}$). The remaining discrepancy may be partly due to a systematic experimental error and partly due to the sensitivity of the calculated heat capacity to the precise shape of the potential well. The heat capacity is calculated for a potential with a parabolic axial field profile (Eq. 7.17), while the experimental field (the "long" geometry) has a shape clearly deviating from this (Fig. 2.7). The effective volume V_{1e} in the experimental field is accurately described by Eq. (7.23), as was shown in Sect. 3.2, but the heat capacity may be much more sensitive to the exact shape, as it depends on $\partial^2 V_{1e}/\partial T^2$. For this reason it would be interesting to do similar measurements of the evaporation dynamics in a trapping geometry which resembles more closely the required parabolic shape (for instance, the "short" geometry, Fig. 2.7) and to establish whether the discrepancy disappears.

The evaporation measurements described in this chapter are only possible in a limited temperature range. Due to the fact that the initial temperature is equal to the wall temperature, $T_i = T_w$, T_i cannot be much higher than 0.3 K: at higher temperatures the ^{4}He background gas becomes a problem. On the other hand, for $T_i = T_w < 0.1\,\text{K}$ the liquid ^{4}He wall coverage starts acting as a true pumping surface so it is no longer possible to switch on the evaporation instantly. However, if a ^{3}He-^{4}He mixture is used for the wall coverage the trapped H↑ gas can be in thermal equilibrium with the cell walls down to $T_w \approx 0.08\,\text{K}$. Consequently, the initial temperature can in principle be varied over the range $0.08\,\text{K} < T_i < 0.3\,\text{K}$ by using different wall coverages. Unfortunately, a spurious radiative heat load on the cell prevented us from doing this within the framework of this thesis.

7.4 Conclusions

We have studied the dynamics of the evaporation process by *in situ* diagnostics of the trapped gas, using Lyman-α spectroscopy. These measurements constitute the first direct observation of thermalization processes in trapped H↑. An analytical model has been developed which describes evaporative cooling in a Ioffe trap. The model is in reasonable agreement with the experimental data.

In view of the importance of evaporative cooling techniques for systems of trapped particles, the subject deserves a continuation study. The experiments described above should be extended by varying the initial conditions T_i and n_{0i}, and the well depth $B_w - B_0$. The model that has been developed can be tested more rigorously by using a field configuration which resembles the model potential more closely. From the theoretical point of view, there are two points which should be addressed more closely: the assumption of quasi-equilibrium during evaporation and the role of constants of motion, other than the total energy.

References

[1] O. J. Luiten, H. G. C. Werij, I. D. Setija, M. W. Reynolds, T. W. Hijmans, and J. T. M. Walraven, Phys. Rev. Lett. **70**, 544 (1993).

[2] C. R. Monroe, E. A. Cornell, C. A. Sackett, C. J. Myatt, and C. E. Wieman, Phys. Rev. Lett. **70**, 414 (1993).

[3] H. F. Hess, Phys. Rev. B **34**, 3476 (1986).

[4] H. F. Hess, G. P. Kochanski, J. M. Doyle, N. Masuhara, D. Kleppner, and T. J. Greytak, Phys. Rev. Lett. **59**, 672 (1987).

[5] N. Masuhara, J. M. Doyle, J. C. Sandberg, D. Kleppner, T. J. Greytak, H. F. Hess, and G. P. Kochanski, Phys. Rev. Lett. **61**, 935 (1988).

[6] J. M. Doyle, J. C. Sandberg, N. Masuhara, I. A. Yu, D. Kleppner, and T. J. Greytak, J. Opt. Soc. Am. **6**, 2244 (1989).

[7] J. M. Doyle, J. C. Sandberg, I. A. Yu, C. L. Cesar, D. Kleppner, and T. J. Greytak, Phys. Rev. Lett. **67**, 603 (1991).

[8] I. D. Setija, H. G. C. Werij, O. J. Luiten, M. W. Reynolds, T. W. Hijmans, and J. T. M. Walraven, Phys. Rev. Lett. **70**, 2257 (1993).

[9] J. J. Berkhout, O. J. Luiten, I. D. Setija, T. W. Hijmans, T. Mizusaki, and J. T. M. Walraven, Phys. Rev. Lett. **63**, 1689 (1989).

[10] J. M. Doyle, Ph. D. Thesis, Massachusetts Institute of Technology (1991).

Samenvatting

In dit proefschrift worden de eerste optische experimenten beschreven met atomair waterstofgas bij zeer lage temperaturen, wandvrij opgesloten in een magneetveld. We laten zien hoe door vacuüm-ultraviolet spectroscopie van de $1S \rightarrow 2P$ Lyman-α overgang in atomaire waterstof, informatie kan worden verkregen over de temperatuur en de dichtheid van magnetisch ingevangen gasmonsters. Hierbij wordt gebruik gemaakt van een zeer nauwbandige lichtbron (bandbreedte ongeveer 100 MHz) bij een golflengte van 121.6 nm, resonant met de Lyman-α overgang. Een belangrijk voordeel ten opzichte van de traditionele bolometrische meetmethodes is het feit dat het gas nu *ter plaatse* bestudeerd kan worden, zonder het monster te vernietigen. Verder worden resonant-optische detectietechnieken gekenmerkt door een zeer hoge gevoeligheid, hetgeen van groot belang is bij lage temperaturen, wanneer het aantal ingevangen deeltjes zeer klein wordt. Tenslotte biedt een resonante lichtbron de mogelijkheid om het gas optisch te koelen.

Het grootste deel van het proefschrift is gewijd aan een gedetailleerde beschrijving van de theoretische en experimentele aspecten van Lyman-α spectroscopie van magnetisch ingevangen atomair waterstofgas. Als eerste toepassing van deze nieuwe diagnostische methode wordt de dynamica bestudeerd van een gasmonster dat geïsoleerd is van de wand door middel van de techniek van het zogenaamde afdampend koelen. Deze (niet-optische) koeltechniek is al eerder met succes toegepast op magnetisch ingevangen waterstofgas en wordt als een goede kanshebber gezien voor het realiseren van macroscopisch quantumgedrag in dit systeem.

Zowel voor de spectroscopie van het gas als voor de beschrijving van de dynamische eigenschappen is nauwkeurige kennis van het magneetveld onontbeerlijk. In Hoofdstuk 2 wordt een methode ontwikkeld om het veld in onze magnetische val te berekenen, gebaseerd op een benadering van het veld door middel van een reeksontwikkeling in cylindercoördinaten en gebruik makend van veldsymmetrieën. Deze methode stelt ons in staat gesloten uitdrukkingen af te leiden, die het veld zeer nauwkeurig beschrijven.

In Hoofdstuk 3 wordt een overzicht gegeven van de eigenschappen van magnetisch ingevangen monsters van atomair waterstofgas. Het laden van de magnetische val, het daaropvolgende thermalisatieproces en verscheidene verlies- en opwarmingsprocessen worden besproken. We voeren een benaderende uitdrukking in voor het veld in onze val, die ons in staat stelt gesloten uitdrukkingen voor de toestandsdichtheid af te leiden. Dit maakt het vervolgens mogelijk om op eenvoudige wijze belangrijke thermodynamische grootheden van het gas te berekenen als het effectieve volume, de soortelijke warmte en de gemiddelde interatomaire botsingsfrequentie.

In de Hoofdstukken 4 en 5 worden de experimentele technieken besproken. In Hoofdstuk 4 wordt het cryogene deel van de opstelling beschreven, met name de preparaatruimte in het hart van de mengkoelercryostaat. Bijzondere nieuwe kenmerken van de opstelling zijn de lichtgeleiding vanaf kamertemperatuur naar het hart van de cryostaat en de cryogene Lyman-α detectoren in de preparaatruimte. De laatste maken het mogelijk zowel de intensiteit te meten van het door het gas doorgelaten licht (transmissie) als de intensiteit van het verstrooide licht (fluorescentie), onder verschillend strooihoeken. In Hoofdstuk 5 wordt het optische deel van de opstelling beschreven. De nauwbandige Lyman-α straling (121.6 nm) wordt opgewekt in krypton gas als de derde harmonische van ultraviolet licht met een golflengte van 364.8 nm. De efficiëntie van deze methode wordt onderzocht en verscheidene speciale technieken worden besproken om de frequentie van het licht te stabiliseren en op de gewenste wijze te kunnen verstemmen. Verder wordt ingegaan op het gebruik van vacuüm-ultraviolet optiek en op de constructie en de gevoeligheid van de cryogene Lyman-α detectoren.

Hoofdstuk 6 is gewijd aan Lyman-α spectroscopie van de magnetisch ingevangen waterstofpreparaten. In het eerste deel van het hoofdstuk wordt een gedetailleerde theoretische behandeling gegeven van de voortplanting van Lyman-α licht door atomair waterstofgas in een uitwendig magneetveld. Een volledige beschrijving van dit proces, noodzakelijk voor een correcte kwantitatieve interpretatie van de experimentele spectra in termen van temperatuur en dichtheid, blijkt vrij gecompliceerd te zijn: De vormen van de spectra worden voornamelijk bepaald door de combinatie van de dichtheidsverdeling van het gas in de magnetische val en Zeeman-frequentieverschuivingen, maar het is essentieel om daarnaast Doppler-frequentieverschuivingen, de polarisatie van het licht en de optische dichtheid en optische aktiviteit van het monster in rekening te brengen. In het tweede deel van dit hoofdstuk komen de experimentele spectra aan de orde. De algemene karakteristieken van de spectra worden kwalitatief verklaard. Tevens laten we zien hoe door vergelijking met theoretisch berekende spectra de temperatuur en de dichtheid van het magnetisch ingevangen gas met ongeveer 25% nauwkeurigheid kunnen worden bepaald. Deze nauwkeurigheid wordt voornamelijk beperkt door de experimentele onzekerheid omtrent het profiel van de lichtbundel. Enige spectra vertonen onverwachte kenmerken, die het gevolg blijken te zijn van subtiele polarisatie- en dispersie-effecten. In dit proefschrift ligt de nadruk op transmissiespectroscopie, maar er worden tevens enkele fluorescentiespectra geanalyseerd. Verder wordt een deuteriumspectrum getoond, dat bewijst dat het mogelijk is in onze opstelling om koud atomair deuteriumgas te maken en vervolgens naar de preparaatruimte te vervoeren. We waren echter niet in staat het atomaire deuteriumgas daadwerkelijk wandvrij op te sluiten in de magnetische val.

In Hoofdstuk 7 wordt de dynamica van het proces van afdampend koelen onderzocht. We hebben een model ontwikkeld, zonder aanpasbare parameters, dat ons in staat stelt gesloten uitdrukkingen af te leiden voor de snelheid waarmee deeltjes ontsnappen en energie wordt onttrokken aan het gas gedurende afdampend koelen in onze magnetische val. We laten zien dat gedurende de aanvang van het afdampproces de energieverdeling van de atomen in de val essentieel afwijkt van de evenwichtsverdeling. Door middel van Lyman-α transmissie-spectroscopie hebben we de temperatuur en de dichtheid van het ingevangen gas gevolgd gedurende het afdampproces. Het nieuwe theoretische model wordt getoetst aan de hand van deze metingen.

Nawoord

Het spreekt vanzelf dat dit werk niet mogelijk was geweest zonder de hulp en steun van velen.

Promotor Jook Walraven schiep de mogelijkheid te werken aan dit uitzonderlijke project. Ik ben hem zeer erkentelijk voor het grote vertrouwen geschonken aan een voormalig theorie-student, die niet gehinderd werd door enige noemenswaardige ervaring op experimenteel gebied. Ik heb altijd met veel genoegen de discussie aangegaan met co-promotor Tom Hijmans. Toms voortvarende aanpak van de talloze problemen en zijn vele 'ideetjes' hebben enorm bijgedragen aan het slagen van het project. Ik had me geen beter gezelschap kunnen wensen dan Irwan Setija gedurende de nachtelijke sessies waarin wij ingewijd werden in de mengkoelmysterieën. Jaap Berkhout leerde ons regendansen en andere cryostaatgeheimen. Raymond van Roijen liet een zeer degelijk geconstrueerde magnetische val na. Het is vrijwel zeker dat dit boekje hier niet zou zijn geweest zonder de komst van postdoc Henri Werij, die onmiddellijk met grote deskundigheid de onwillige fotonen naar zijn hand zette. Onvervangbaar was ook postdoc Meritt Reynolds, de man die sneller programmeert dan zijn schaduw. Ik heb grote bewondering voor Otto Höpfner, die onder zeer moeilijke omstandigheden een perfecte experimenteercel bouwde. Joost Overtoom stond altijd klaar om onze onverzadigbare honger naar speciale onderdelen te stillen en daarna onze dorst te lessen. Helaas is Joost minder geschikt als rijinstructeur. Studenten Frederike Noordman, Ingrid Zevenbergen en Tycho Sonnemans hebben zeer waardevolle bijdragen geleverd aan de opbouw van het experiment én de sfeer in de groep. Ik wens Pepijn Pinkse veel succes met de voortzetting van het trap-experiment. I thank Simo Jaakkola for carefully reading the manuscript.

Met Wim Koops heb ik met veel plezier de kamer gedeeld. De groep 'Spectroscopie van de Verdichte Materie' als geheel is verantwoordelijk voor vele inspirerende en uit de hand gelopen koffiepauzes, lunches en vrijdagmiddagbesprekingen: Ad Lagendijk, Rudolf Sprik, Theo Nieuwenhuizen, Gerard Wegdam, Johannes de Boer, Mark van Rossum, Peter den Outer, Rik Kop, Ron Kroon, Mark Kroon, Maurice van Hoften, Bert Holsbeeke en vele anderen. Speciale vermelding verdienen de 'Magnificent 7', die gedurende 'a.i.o.-night' de Warmoesstraat écht onveilig maakten.

Graag wil ik Siem Bominaar bedanken voor een zeer consciëntieuze drukijking van de smeltlijnthermometer en Klaas Prins en Huib Luigjes voor het gewillig afstaan van een magneetvoeding.

Het experiment was alleen mogelijk door een geweldig uitgebreide en deskundige technische ondersteuning. Hiervoor wil ik bedanken Ton Jongeneelen, Edwin Baay, Flip de Leeuw, Piet Sannes, Theo van Lieshout, Jan Mulder, Jan Water, Jan Dekker, Rob Verbrugge, Johan van de Ridder, Dirk de Vries, Johan Soede, Fred van Anrooij, Ruud Scheltema, Ton Riemersma, Hugo Schlatter, Bert Zwart en Eddy Inoeng. Nico Jonker, Herman Pothoven en Gordon Reiziger zorgden ervoor dat we nooit droog kwamen te staan gedurende de lange meetruns. Zaken op bestuurlijk, administratief en huishoudelijk gebied werden steeds kundig verzorgd, onder anderen door Mariet Bos, Jenny Batson, Ineke Baay, Willem Mattens en Klaas van Paasschen.

Ing wil ik bedanken voor haar begrip en geduld en de plezierige jaren in Amsterdam. Tenslotte ben ik Eileen dankbaar voor het nauwkeurig doorlezen van het manuscript en familie en vrienden voor het geduldig aanhoren van de enthousiaste verhalen waarmee de langzame vorderingen werden ingekleed. Helaas heb ik sommigen moeten teleurstellen dat we nul Kelvin nog steeds niet bereikt hebben. Vianney had ze dit echter al van tevoren kunnen vertellen.